

Type of Report: Final Report

NASA Cooperative Agreement: # NNX07AP33A

Title: Flight Mechanics and Control Oriented Modeling of Next Generation On-Blade Control Concepts

Contributors:

Georgia Institute of Technology: J.V.R. Prasad, L.N. Sankar, Jeremy Bain, Ersel Olcer

Advanced Rotorcraft Technology: Chengjian He, Jinggen Zhao

Sikorsky Aircraft Corporation: Stephen Makinen

Washington University: David Peters

Date: September 28, 2010

TABLE OF CONTENTS

EXECUTIVE SUMMARY	2
NOMENCLATURE	5
BACKGROUND	7
TASK 1. CFD ANALYSES OF SELECTED OBC CONCEPTS.....	11
TASK 2. DEVELOPMENT OF REDUCED ORDER MODELS	44
TASK 3: INTEGRATION OF OBC REDUCED ORDER MODELS AND EVALUATIONS..	61
TASK 4: DEVELOPMENT OF EFFICIENT ALGORITHMS FOR EXTRACTION OF LINEAR TIME INVARIANT MODELS	64
TASK 5: LTI MODEL FIDELITY EVALUATIONS	74
CONCLUDING REMARKS.....	92
ACKNOWLEDGMENTS	93
REFERENCES	94

EXECUTIVE SUMMARY

This final report summarizes work performed under the NASA NRA cooperative agreement # NNX07AP33A titled “Flight Mechanics and Control Oriented Modeling of Next Generation On-Blade Control Concepts.” This executive summary presents the research objectives and the major highlights of the accomplishments. This research effort was divided into five specific tasks. The work done under each task is presented in this report.

Individual Blade Control (IBC) and On-Blade Control (OBC) concepts offer tremendous potential for expanding the design space for tailoring control input signals for desired individual blade responses to simultaneously address the flight control issues and the rotor control issues. The implications of higher-bandwidth arising from IBC and OBC concepts are currently only amenable to Computational Fluid Dynamics (CFD) plus Computational Structural Dynamics (CSD) analyses. Further, the state-of-the-art CFD plus CSD analyses tools are computationally expensive and are not suitable for controller synthesis, analysis and simulations needed in the design cycle. Hence, reduced-order models are needed that capture the essential physics of OBC control concepts for fast and real-time simulations. Further, linearized models in a linear time invariant (LTI) form that retain the important coupled rotor/body dynamics with various IBC and OBC concepts are needed for handling qualities assessment and integrated flight/rotor control development.

The 2-year research program was conducted by a team of researchers from the Georgia Institute of Technology, the Washington University, Advanced Rotorcraft Technology, Inc., and the Sikorsky Aircraft Corporation. The objectives of this study are to develop a methodology for physics based reduced order modeling of next generation OBC concepts suitable for fast and real time simulations and a computationally efficient framework and algorithms for extraction of time-invariant linearized models suitable for handling qualities assessment and integrated flight and rotor control design and analyses. The reduced order model development has exploited the experience gained by the Sikorsky Aircraft Corporation with analyses and wind tunnel test data of a variety of OBC concepts and the enhanced CFD and CSD tools from the DARPA Quieting Program. The methodology development for extraction of linearized models in time invariant form has benefitted from the past efforts in the literature for expressing time periodic states in the harmonic domain.

Specifically, the following work was done.

- The prediction accuracy of the developed reduced-order models has been evaluated through comparisons with high fidelity CFD predictions and available test data.
- A reduced order modeling framework using artificial neural networks has been developed for capturing aerodynamic and dynamic effects of rotor on-blade control.
- The developed reduced order models have been integrated into the modular architecture of FLIGHTLAB simulation model for fast and real time demonstrations.
- New algorithms have been developed by exploiting the harmonic domain representation of rotor states for extraction of LTI models of coupled body-rotor dynamics suitable for

various control design applications with IBC and OBC concepts and for handling qualities assessment.

- The prediction accuracy evaluation of the extracted LTI models has been accomplished through comparisons with the nonlinear model predictions in time and frequency domains.

The successful completion of the present 2-year program lays a firm foundation for the development of reduced order models of several OBC and IBC concepts. These models are suitable for fast and real time simulations, and when combined with the methodology for linear model extraction method developed in this study, can be used for computationally efficient extraction of coupled rotor and body LTI dynamic models. The LTI models may already be used for design of various integrated flight/rotor controllers using IBC and OBC concepts. This capability is expected to dramatically improve the prediction capabilities needed in the design process for expanding the civilian utility of rotorcraft to meet NASA Strategic Goals and supplement subsonic rotary wing technology and its development in the United States.

MS & Ph. D STUDENTS

The following students were fully or partially supported under this project.

- Roosevelt Samuel, MSAE, 2008
- Brian Clark, MSAE, May 2010
- Byung Young Min, Ph.D, May 2010
- F. Ersel Olcer, Ph.D. in progress

JOURNAL ARTICLES

The following journal articles were published under this effort:

- Bain, J., Sankar, L. N., Prasad, J. V. R., Bauchau, O., Peters, D. A., and He, C., “Computational Modeling of Variable Droop Leading Edge in Forward Flight,” *Journal of Aircraft*, Vol. 46, No. 2, pp. 617-626, March-April 2009.
- Min, B. Y., Sankar, L., Rajmohan, N., and JVR Prasad, ” Computational Investigation of the Effects of Gurney Flap on the Forward Flight Characteristics of Helicopter Rotors,” *Journal of Aircraft*, Vol. 46, No. 6, November – December 2009, pp. 1957 – 1964.

CONFERENCE PAPERS

The following conference articles were published under this effort:

- Min, B. Y., Sankar, L., Rajmohan, N. and JVR Prasad, “Computational Investigation of the Effects of Gurney Flap on the Forward Flight Characteristics of Helicopter Rotors,” AIAA 2008-6726.
- Bain, J., Sankar, L. N., Prasad, J. V. R., Bauchau, O., Peters, D. A., and He, C., “Computational Modeling of Variable Droop Leading Edge in Forward Flight ,” AIAA 2008-3872.

- Min, B. Y., Sankar, L. N., Prasad, J. V. R., and Schrage, D. "A Physics-Based Investigation of Gurney Flaps for Rotor Noise and Vibration Reduction," AHS 65th Annual forum, May 2009.
- Bain, J., Samuel, R., Sankar, L. N., and Prasad, JVR, "Neural Network Models for the On-Board and Individual Blade Control of Helicopter Rotors ," AIAA Paper 2009-3521, 27th AIAA Applied Aerodynamics Conference, San Antonio, Texas, June 22-25, 2009.
- Prasad, J.V.R., Olcer, F.E., Sankar, L.N. and He, C., "Linear Models for Integrated Flight and Rotor Control," 34th European Rotorcraft Forum, Liverpool, UK, September 16-19, 2008.
- He, C, Zhao, J., Sankar, L.N., Bain, J., and Prasad, J.V.R., "Development of a Reduced Order Modeling Framework for Flight Mechanics Oriented Modeling of On-Blade Control Concepts," 35th European Rotorcraft Forum, Hamburg, Germany, September 22-5, 2009.
- Prasad, J.V.R., Olcer, F.E., Sankar, L.N. and He, C., "Linear Time Invariant (LTI) Models for Integrated Flight and Rotor Control," 35th European Rotorcraft Forum, Hamburg, Germany, September 22-5, 2009.
- Olcer, F.E., Prasad, J.V.R., Sankar, L.N., Bain, J., Zhao, J., He, C, "Development and Evaluation of Reduced Order Models of On-Blade Control for Integrated Flight and Rotor Control", AHS 66th Annual forum, May 2010.

NOMENCLATURE

A	LTI model system matrix
A_{ij}	Sub-matrices of LTI state matrix
B	LTI model input matrix
B_i	Sub-matrices of LTI control matrix
b	Airfoil half chord length
b_δ	Trailing edge flap half chord length
C	LTI model output matrix
C_i	Sub-matrices of LTI output matrix
c	Chord
C_d, C_l, C_m	Drag, lift and moment coefficients
D	Drag
D	LTP model damping matrix
E	LTI model input-to-output matrix
F_x, F_y, F_z	Fixed system hub forces
G	LTP model input matrix
K	LTP model stiffness matrix
k_α	Reduced frequency of angle of attack
k_δ	Reduced frequency of trailing edge flap deflection
L	Lift
L	number of harmonic components of y
l_{GF}	Gurney flap length
M	Mach number
M_x, M_y, M_z	Fixed system hub moments
M	Number of harmonic components of control
N	Number of harmonic components of x
n_t	Number of response points used in model fidelity evaluation
n_o	Number of outputs used in model fidelity evaluation
P	LTP model output matrix associated with x
Q	LTP model output matrix associated with \dot{x}
R	Rotor radius
r	Radial location along a rotor blade
t	Time
U	Control vector
u	Change in U from trim
V_∞	Free stream velocity
X	Vector of displacement variables
x	Change in X from trim
\dot{x}, \dot{X}	First time derivatives of x and X
\ddot{x}, \ddot{X}	Second time derivatives of x and X
\bar{X}, \bar{U}	Periodic steady state values of X and U
Y	Output vector
y	Change in Y from trim
α	Angle of attack

$\dot{\alpha}$	Time rate of angle of attack
α_o	Mean angle of attack
α_c	Cosine harmonic of angle of attack
β	Trailing edge flap deflection
δ	Trailing edge flap deflection
δ_c	Cosine harmonic of trailing edge flap
$\dot{\delta}$	Time rate of trailing edge flap deflection
Δ	Deviation from the trim point
Γ	Generalized loading
ϕ	Phase lag
Ω	Rotor rotational speed
ω	Frequency
Ξ	Equation imbalance
ψ	Azimuth location
ψ_δ	Phase angle between angle of attack and trailing edge flap

Subscripts

$(\)_o$	Zero-th harmonic component/average component of ()
$(\)_{nc}$	n^{th} harmonic cosine component of ()
$(\)_{ns}$	n^{th} harmonic sine component of ()
$(\)_{aug}$	Augmented vector made up of average and harmonic components

Acronyms

BVI	Blade-Vortex Interaction
IBC	Individual blade control
LTP	Linear Time Periodic
LTI	Linear Time Invariant
MBC	Multi Blade Coordinates
NNET	Neural Network
OBC	On-blade control
ROM	Reduced Order Airloads Model
TEF	Trailing Edge Flap

BACKGROUND

Current flight controller designs for helicopters represent a difficult trade-off between controller bandwidth and its impact on rotor stability, rotor vibratory loads, etc. Traditional swashplate controls in terms of collective, longitudinal cyclic and lateral cyclic limit the number of controls available to the control designer in addressing flight and rotor control issues. For example, a four-bladed rotor using IBC has four independent controls available. However, the use of swashplate for control inputs restricts the number of independent controls to only three, thus limiting the control design space available to the control designer.

Individual Blade Control (IBC) and On-Blade Control (OBC) concepts offer tremendous potential for expanding the available control design space in tailoring control input signals for desired blade responses to address flight and rotor control issues in a unified framework. IBC and OBC concepts offer the potential to develop innovative controllers for mitigation of compressibility effects on advancing blades and reverse flow effects on retreating blades for improved rotor performance, control of an individual blade that may be off-track, mitigation of transient effects associated with rotor speed variations, mitigation of undesirable coupling between body and rotor in large size helicopters due to increased rotor blade flexibility, reduction of maneuver blade and rotor loads, reduction of vibratory hub loads, reduction of blade-vortex interaction noise, etc., while ensuring good flying qualities as specified in the Aeronautical Design Standard (ADS-33). While higher flight control bandwidth can be achieved through innovative integrated flight and rotor control designs, the implications of such higher bandwidth control arising out of IBC and OBC concepts on handling qualities and vehicle-pilot-biodynamic coupling, etc., need to be carefully assessed before they can be fully realized.

Higher harmonic control of swashplate [1-2], individual blade control [3-6] and on-blade control [7-9] applications both in wind tunnel and flight tests have been documented extensively in the literature. Expansion of the control space through IBC/OBC has enabled researchers to show possibilities of extensive improvements for reduced power [1,3,7], vibration [1,3,7], and noise [3,4,7]. Along with these primary improvements, even additional capabilities emerged such as gust alleviation [9], correction of the blade tracking problems due to dissimilarity between blades, higher redundancy for safety and reliability [10] of a modern helicopter. These studies focused on the rotor control applications alone without assessing their effect on handling qualities.

Higher harmonic control using on-blade control will require high fidelity aerodynamic analysis which includes changes in angle of attack and on-blade control deflections as well as deflection rates. This has been achieved in the literature by coupling Computational Fluid Dynamics (CFD) methods with comprehensive flight dynamic analyses codes, for example as in [11]. Unfortunately, the state-of-the art CFD plus Computational Structural Dynamics (CSD) analyses tools for assessing the implications of IBC and OBC concepts are computationally expensive and are not suitable for controller synthesis, analysis, simulations and handling qualities assessment needed in the design cycle.

Due to the periodic nature of helicopter rotors, the linearized models including rotor states extracted from nonlinear models of a rotorcraft will have periodic coefficients. Though stability

analysis of the extracted linear time periodic (LTP) models can be performed using the Floquet stability theory, it does not provide a convenient framework for controller synthesis and design as the available control design tools for LTP systems are few in number [12]. Further, the handling qualities specifications for small amplitude maneuvers as prescribed in the Aeronautical Design Standard (ADS 33) are based on a linear time invariant (LTI) model, and thus cannot be directly accounted for in the controller design process using LTP models. If linearized models in time invariant form are made available, it will open up the choice of available design and analyses tools to a rotorcraft control designer [12].

If one uses the current method of averaging over one rotor period for extracting a linear model with constant coefficients, the averaging process also removes all the dynamic coupling between the body states and the frequency components of the rotor states and controls. This presents a severe disadvantage of using such time averaged LTI models for integrated flight and rotor control design applications. For example, the impact of pilot control inputs on the rotor higher harmonic vibratory loads cannot be addressed using such models directly in the design process.

Methods available in the literature for transformation of LTP models to time-invariant form suffer from certain disadvantages. For instance, in the Lyapunov-Floquet transformation method [13], the system matrix of the LTP model is transformed into a time-invariant form using the time varying Lyapunov-Floquet transformation matrix. However, the control matrix of the transformed model will still be time-periodic. To overcome this difficulty, an auxiliary system is constructed with pseudo control variables which bear no resemblance to the control vector of the LTP model. Controller design is carried out on the auxiliary system and control laws for the time periodic system are constructed from feedback signals of the auxiliary system. However, this method suffers from the disadvantage of needing to compute the state transition matrices of the LTP model over one rotor period in order to construct the Lyapunov-Floquet transformation matrix. Analytical approximations of the coefficient matrices using the shifted Chebyshev polynomials of the first kind provide an efficient means in the state transition matrix computations. While the computational effort is significantly improved by the use of such closed form approximations, the accuracy of the results is significantly influenced by the number of terms used in the analytical approximations, and such an approach becomes numerically very sensitive. The transformation using discrete-time methods, such as time lifting and frequency lifting methods [14], also suffer from the same disadvantage of a need for state transition matrices.

The use of harmonic analyzers as part of the linearization step to extract a time invariant linear model for the specific application of flight control and higher harmonic control is explored in [12]. The extracted LTI model consists of the body states, time averaged rotor states, harmonic analyzer states, pilot controls and higher harmonic controls. Using such a model, Cheng, et al [12] show that it becomes feasible to consider the important coupling between the body states and the higher frequency rotor response in a combined flight and vibration controller design. Using numerical perturbations to individual harmonic components of periodic states of a system, LTI models are formulated with average and harmonic components of rotor response as augmented states in [15]. However, it is well known that the use of numerical perturbation techniques for extraction of linear models from a nonlinear model is sensitive to the size of state and control perturbations. Also, in cases where reduced order models are sought from the

linearization, the effect of state and control perturbations on the neglected states have to be properly taken into account, thus further increasing the computational complexity of the linearization process. More importantly, the number of harmonic components of rotor states required in the LTI model for retaining the important coupling between body states and rotor states is generally not known *a priori* in a specific application. As a result, one may be forced to consider different LTI model approximations in order to arrive at the appropriate model, thus further increasing the computational complexity of the linearization process.

From the above discussion, it is clear that there is a need that exists for the development of reduced-order models that capture the essential physics of the impact of IBC and OBC concepts on rotor aerodynamics for fast and real time simulations in order to fully realize the potential advantages offered by IBC and OBC concepts. Also, a need exists for the development of computationally efficient algorithms for extraction of linearized models in time-invariant form that still retain the important couplings between body states, rotor states and controls including components of high frequency rotor response. Such models will open up the design freedom available to the control designer in addressing simultaneously the flight control and rotor control issues.

RESEARCH GOALS AND TASKS

In order to address the above discussed needs, the project has the following research goals and Tasks:

Research Goals:

- Develop a methodology for the generation of physics based reduced order models of next generation OBC concepts suitable for fast and real time simulations
- Develop a computationally efficient framework and algorithms for extraction of time-invariant linearized models suitable for handling qualities assessment and integrated flight and rotor control design and analyses.

Tasks:

1. Generate a data base of the impact of various OBC concepts on rotor aerodynamics using high fidelity CFD models.
2. Using the generated data base and available test data, develop physics based reduced order models of next generation OBC concepts suitable for fast and real time simulations.
3. Evaluate the prediction accuracy of the reduced order models through comparisons with comprehensive CFD predictions and available test data.
4. Develop a computationally efficient framework and algorithms for extraction of time-invariant linearized models suitable for handling qualities assessment and integrated flight and rotor control design and analyses.
5. Evaluate the prediction accuracy of the time-invariant linearized models through comparisons with nonlinear model predictions in both time and frequency domains.

The outcome of the 2-year program is sufficient development of methodology and computationally efficient algorithms for generation of reduced order aerodynamic models of

OBC concepts from CFD analyses, integration of such models with comprehensive flight dynamic models, and extraction of coupled rotor and body LTI dynamic models. A detailed description of the work performed under each of the above tasks is included in the following sections along with concluding remarks.

TASK 1. CFD ANALYSES OF SELECTED OBC CONCEPTS

The primary objective of this task is to generate a data base of the impact of various OBC concepts on rotor aerodynamics using high fidelity CFD models. This database along with available test data is used to develop physics based reduced order models suitable for fast and real time simulations. Secondary objectives of this task include evaluation of the prediction accuracy of the reduced order models through comparisons with comprehensive CFD predictions and available test data. Figure 1 shows the overall approach.

Task 1 Process

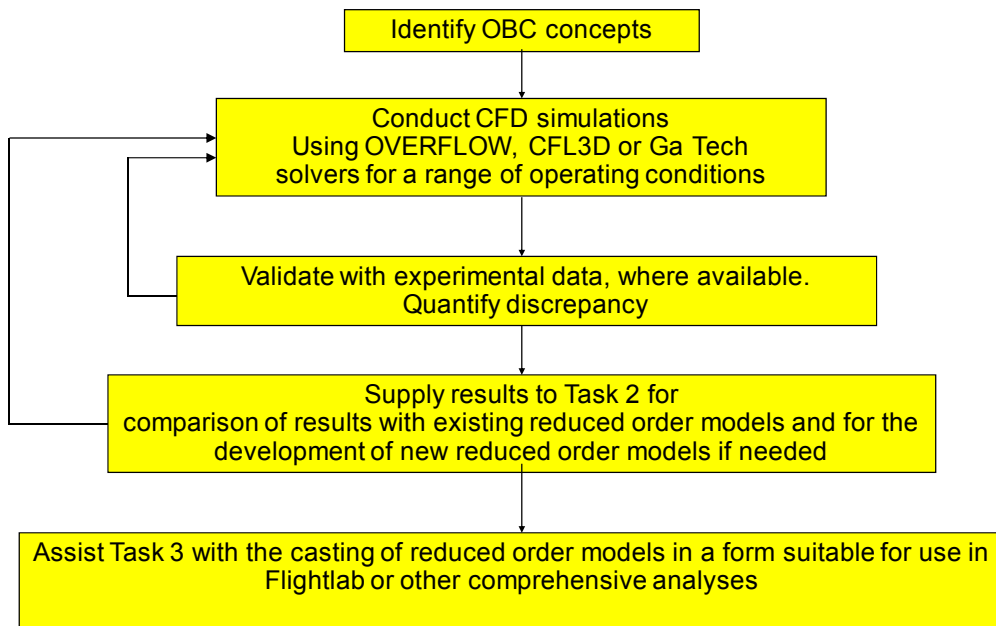


Figure 1. Overall approach for Task 1

OBC Concepts Studied

The following OBC concepts were explored in detail.

- Surface Blowing/Suction
- Variable Camber/Dynamic twist
- Leading Edge Slat and Trailing Edge Flap Devices

Of these concepts, the variable camber, dynamic twist, leading edge slot, and trailing edge flaps were examined in detail. Surface blowing and suction were not explored, although the reduced order model approach considered in Task 2 are equally applicable to surface blowing/suction concepts.

Active twist database was validated using test data for unsteady aerodynamics of oscillating airfoils. The oscillating trailing edge flap database was validated using Tijdeman's database. Leading edge slat studies were validated using experimental data collected by Chandrasekhara and Tung. 2-D calculations were done for Gurney flaps as well.

A limited number of 3-D studies were done. These data were used to assess how the OBC concepts considered in this study influence the rotary wing aeromechanics, both from a time-averaged steady state perspective (rotor thrust, power, L/De) and from vibratory load characteristics. The 3-D simulations were also useful in assessing whether the 2-D reduced order models should be corrected for 3-D effects such as radial flow, and flap/slot edge losses.

Task 1 Metrics

The following metrics were used as success criteria for Task 2.

- Comparisons will be made with experimental and analytical data.
- Normalized fit error between the experimental data and the analyses results to be less than 15%

2-D Results and Discussion

Most of the simulations in this task were done using the OVERFLOW structured overset grid analysis. Because the primary objective of this project is to establish a process for developing and implementing reduced order models of OBC concepts, other in-house solvers were also used where convenient. In all cases, validation of the solver for the intended OBC application was done. This section describes some of the validation studies.

Validation of Active Twist Aerodynamics

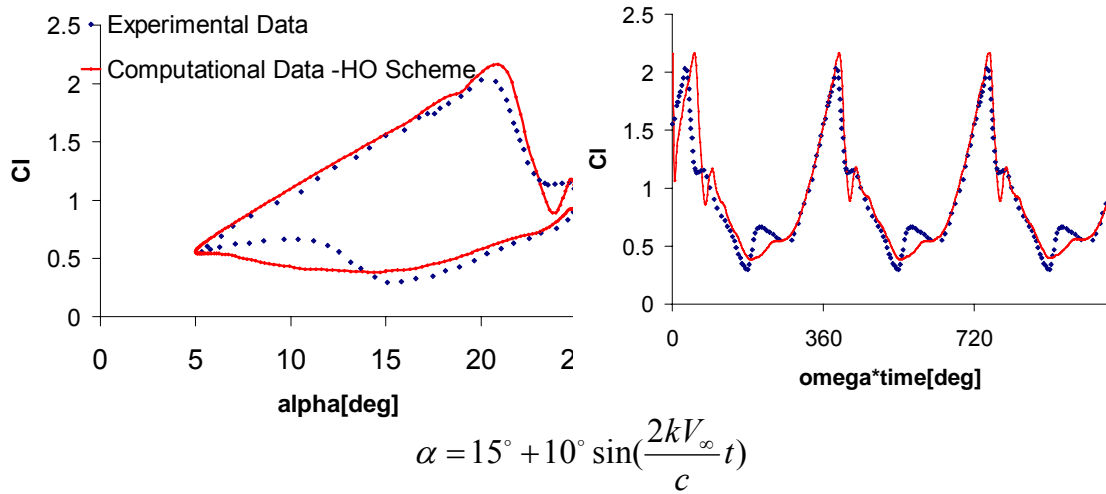
The present comparative study makes extensive use of results from an experiment conducted by Larry Carr, Ken McAlister, and Jim McCroskey at NASA Ames Research center. The flow conditions are as follows:

Reduced frequency $k=0.1$, Freestream Mach number = 0.3, Reynolds number = 3.55 Million

$$\alpha = 15^\circ + 10^\circ \sin\left(\frac{2kV_\infty}{c} t\right)$$

The OVERFLOW 2.0y solver, with a sixth order spatial accuracy scheme implemented by the present investigators, was used. Figure 2 shows typical results.

Hysteresis Curve for Lift (OVERFLOW, STVD6 scheme)



K= Reduced Frequency = 0.1 V_∞ = Freestream Speed of Sound
 C = Chord $M_\infty = 0.3$, Re = 3.55 Million.

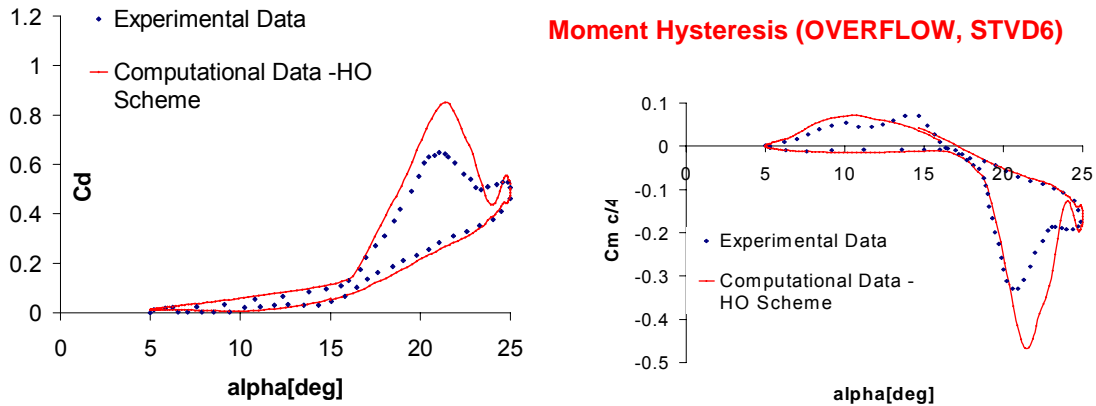


Figure 2. Variation of Lift and Drag with Angle of Attack for the NACA 0012 Airfoil

Oscillating Trailing Edge Flaps:

Trailing edge flaps are effective OBC devices because of their ability to modify the sectional lift and pitching moments. An extensive set of test data for NACA 64A006 airfoil have been obtained by Tidjeman at transonic Mach numbers. In the present study, validations were done at a freestream mach number of 0.875, which caused extensive transonic flow and unsteady flow variations associated with shock motions over the upper and lower surface, both. The trailing edge flap undergoes sinusoidal oscillations (1 degree) at a reduced frequency of 0.234, based on semi-chord. In-phase and out-of-phase components of measured data are available for comparison. Figure 3 below shows the present computations, along with experimental data.

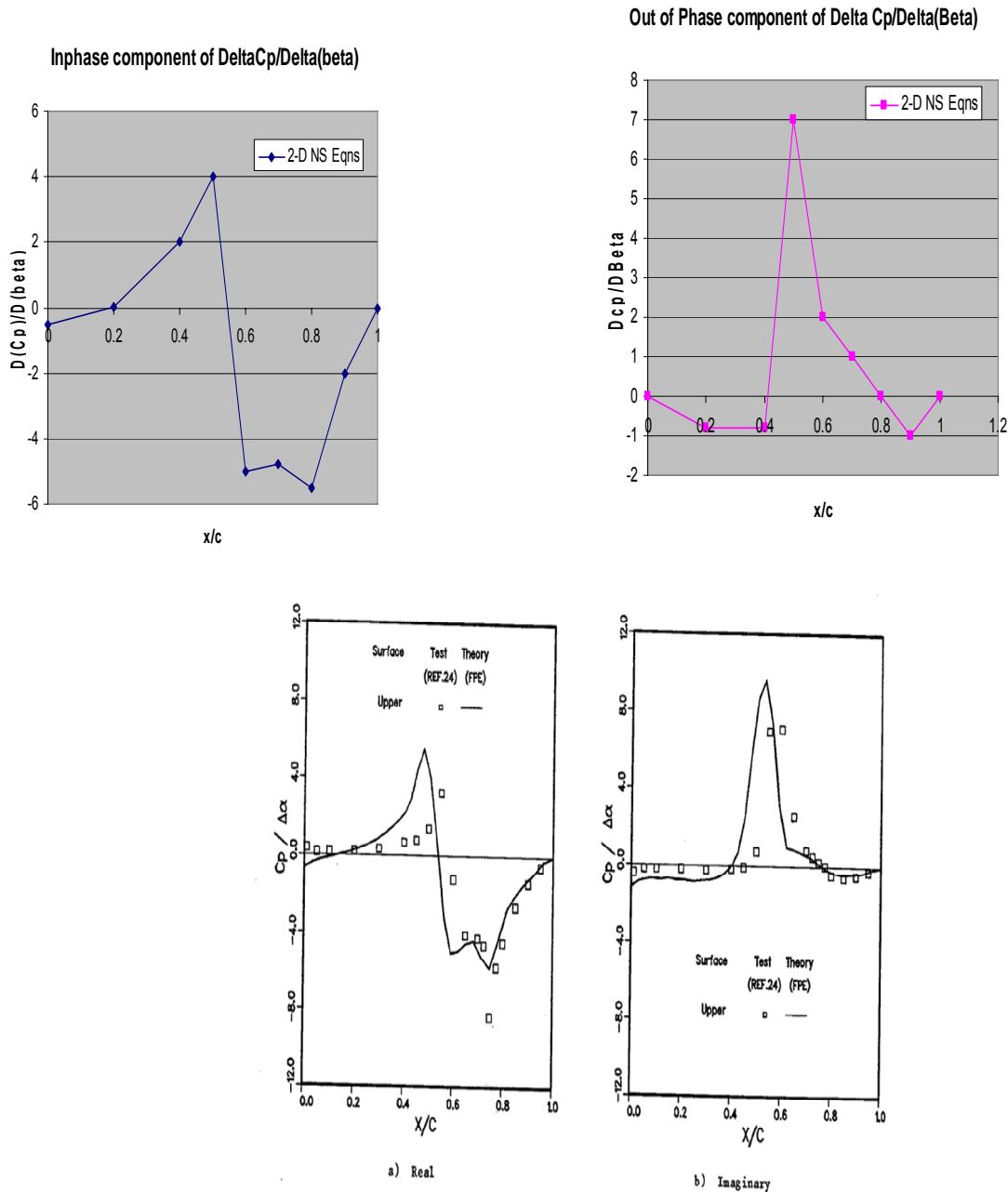


Figure 3. In Phase and Out-of-Phase Components of the Surface pressure Distribution for a NACA 64A006 airfoil Equipped with an oscillating Trailing Edge Flap (Free Stream Mach Number of 0.875, $k=0.234$).

Deformable Leading Edge (DDLE) Concept for Alleviating Dynamic Stall

It is well known that an active or passive leading edge droop can alter the dynamic stall characteristics of airfoils and rotors substantially. Calculations were done for a DDLE airfoil using the Ga Tech in-house solver, and are repeated using OVERFLOW. In this approach, the airfoil shape is gradually changed, and the leading edge radius is increased as the airfoil pitches up. Airfoils with large leading edge radii tend to have mild adverse pressure gradients, because

the peak local velocities are lower than that for a conventional airfoil. As the airfoil pitches down, and there is no danger of stall, the airfoil returns to its original shape.

The reduced frequency $k = \omega c / 2V_\infty$ is 0.05, where $c/2$ is the airfoil semi-chord, and V_∞ is the free-stream velocity. The Free-stream Mach number is 0.3. These parameters correspond to the experiment described in a paper by Chandrasekhara et al [16]. Preliminary numerical results for this concept have been presented by the present researchers [17]. The airfoil pitching motion is described by:

$$\alpha = 10^\circ + 10^\circ \cos(\omega t)$$

Figure 4 shows how the leading edge and alpha both vary with time. Figure 5 shows how the body-fitted grid may be dynamically deformed to accommodate these changes. Figure 6 shows the dynamic stall hysteresis loops for the DDLE airfoil and the baseline NACA 0012 airfoil. It is clear that the DDLE has a smooth rise and drop in the lift coefficient as the airfoil pitches up and down. The variations in pitching moment are very mild, indicating that the resulting pitch link loads will be small as well.

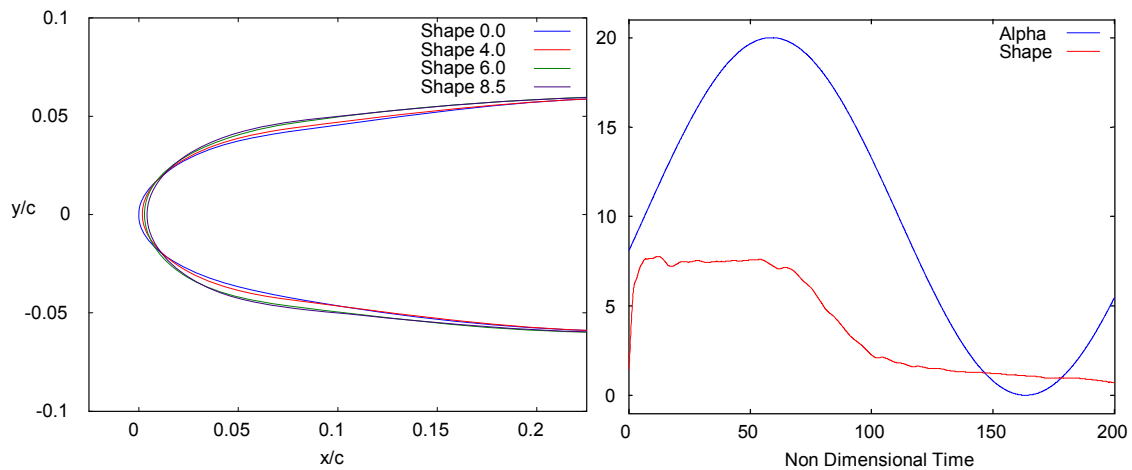
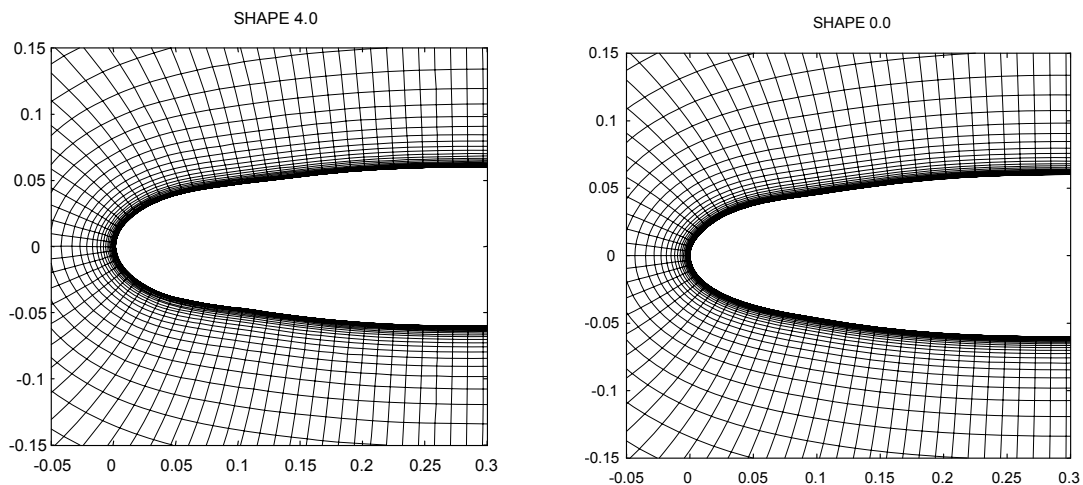


Figure 4. Variation of Angle of Attack and Leading Edge Shape with Time



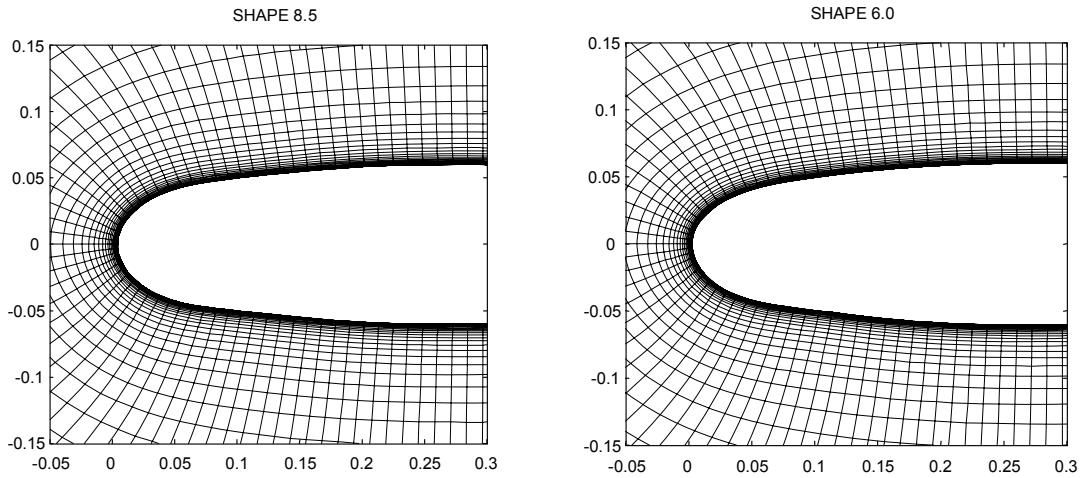


Figure 5. Body Fitted Grid near the Leading edge for Four Typical DDLE airfoil profiles

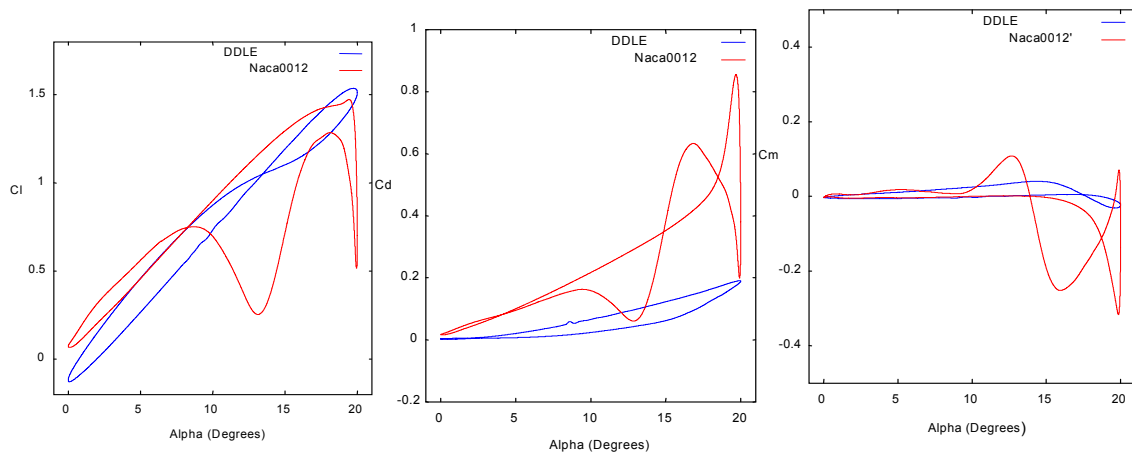


Figure 6. Comparison of computed Lift, Moment and Drag Hysteresis Loops between the NACA 0012 and the DDLE Airfoils

Drooped leading Edge Concept:

Calculations were also done for static drooped leading edge concepts to assess their influence on dynamic stall characteristics. A NACA 0012, an Ames-01 airfoil, and a VR-7 airfoil with a fixed 15 degree leading edge droop were studied. Figure 7 shows the configurations with and without droop. Figure 8 shows the surface pressure contours at selected instances in time for representative airfoils. It is clearly seen that the leading edge droop, even in a static manner, substantially alters the leading edge vortex formation, and mitigates the dynamic stall events.

C-type Grids for NACA0012 & VR-7



C-type Grids for NACA0012 & VR-7 with 15 deg Droop



Figure 7. Modeling of NACA 0012 and VR-7 Airfoils with a Drooped leading Edge

Comparison of Rigid & Drooped VR-7



Comparison of Rigid & Drooped Ames-01



Figure 8. Comparison of Pressure Field over a VR-7 and an Ames-01 airfoil with and without Droop at 24.7 degrees during Upstroke

Additional VDLE calculations were made using OVERFLOW. OVERFLOW, developed by NASA, uses overset structured grids for a wide variety of problems including rotorcraft simulations [18]. Version 2.0y with modifications made under the DARPA Helicopter Quieting Program, as reported by Duque et al [19] was used with elastic blade motion capability as

implemented per Nygaard. For 2-D calculations, two different grids were generated. The first was a C-grid of dimensions 547x105 was used with a y^+ of one. The second grid modeled the wind tunnel walls with a smaller C-grid of dimensions 257x50 and a stretched 119x62 Cartesian grid similar to previous OVERFLOW runs in this wind tunnel [20, 21]. In dynamic stall tests, 35,000 time steps per loop were used with 4 Newton sub-iterations. Calculations were made with up to 8 Newton sub-iterations but were found to produce near identical results. The solutions were run for 2-2.5 cycles using 4th order Central Differencing and the KES turbulence model [22, 23].

Two different grid deformation techniques were implemented within OVERFLOW. The first method requires several volume grids to be created before running OVERFLOW. OVERFLOW was modified to read in four grids representing no droop, maximum droop and two intermediate droop values. The grid at each time step was then calculated algebraically by interpolating between those grids for a particular droop angle. The second method used followed that of Morton [24]. This method was used by previous researches for similar variable leading edge deformations in OVERFLOW [25]. Once the deformed surface is calculated, the points in the normal direction are found by calculating the local normal to the grid surface. This maintains grid orthogonally at each time step. As the distance from the surface increases, a cubic spline is used to smoothly blend the deformed grid and the original grid. This maintains the outer boundary of the original grid. This results in some curving of the grid as shown in Figure 9. No differences were seen in the computed results to plotting accuracy. The second method has reduced memory requirements as only the four surface grids were kept in memory instead of all four volume grids and a small increase in computational time of 5%. In the three dimensional tests, the original grid was modified with the leading edge deformation at each time step before the elastic deformations are applied. The cubic blending function was modified for the 3D grids to be fully blended at 0.5 chord lengths from the blade surface.

To evaluate the grid deformation scheme in two dimensions, calculations were first done on a VR-12 airfoil with a both fixed and variable drooping leading edge from the experiment of Chandrasekhara [16]. This experiment used a VR-12 airfoil with up to a 25 degree leading edge droop from the quarter chord. C-grids were made for fixed droop angles of 0, 5, 10, 15, and 20 degrees by rotating the leading edge down as shown in Figure 9. The experiment has two mild steps near the hinge line as the airfoil transitions between the leading edge element, hinge, and main airfoil element that resulted in some additional separation. The grid had a smooth upper surface and does not have these transitions.

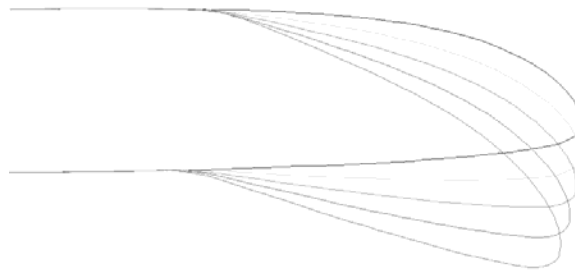


Figure 9. Surface of VR-12 Standard and Drooped Airfoils

Typically, dynamic stall computations use a single grid to model the entire flow field and apply freestream boundary conditions in the far field. This yields good results when the wind tunnel has a high height-to-width ratio so that the wind tunnel walls can be neglected. Previous computations neglected the wind tunnel wall effects and under predicted the lift curve slope and delayed stall [26]. Figure 10 shows the VR-12 in dynamic stall with and without the wind tunnel walls. The inclusion of wind tunnel walls results in significant improvement of the lift curve slope, maximum lift, and angle of stall of the baseline airfoil. Peak lift and drag were well predicted but peak pitching moment was under predicted. Figure 11 shows the lift results for 10 and 20 degree fixed droop cases. Both show good agreement with experimental data when wind tunnel walls are included. As the angle of droop is increased, the maximum lift, pitching moment, and drag are reduced.

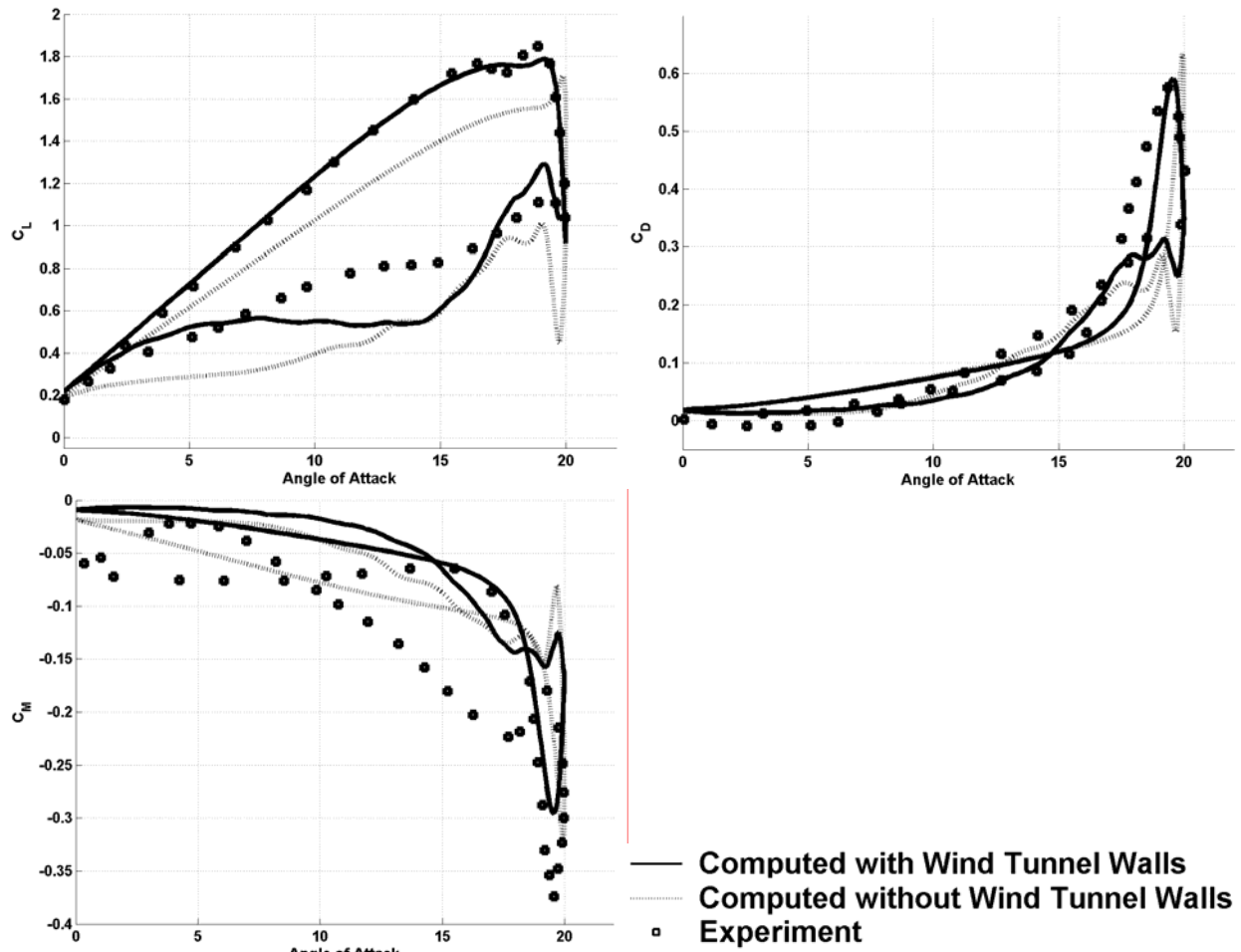


Figure 10. Comparison of Experimental and Computed Results for VR-12
 $M=0.3, k=0.1, \alpha=10^\circ + 10^\circ \sin(\omega t)$

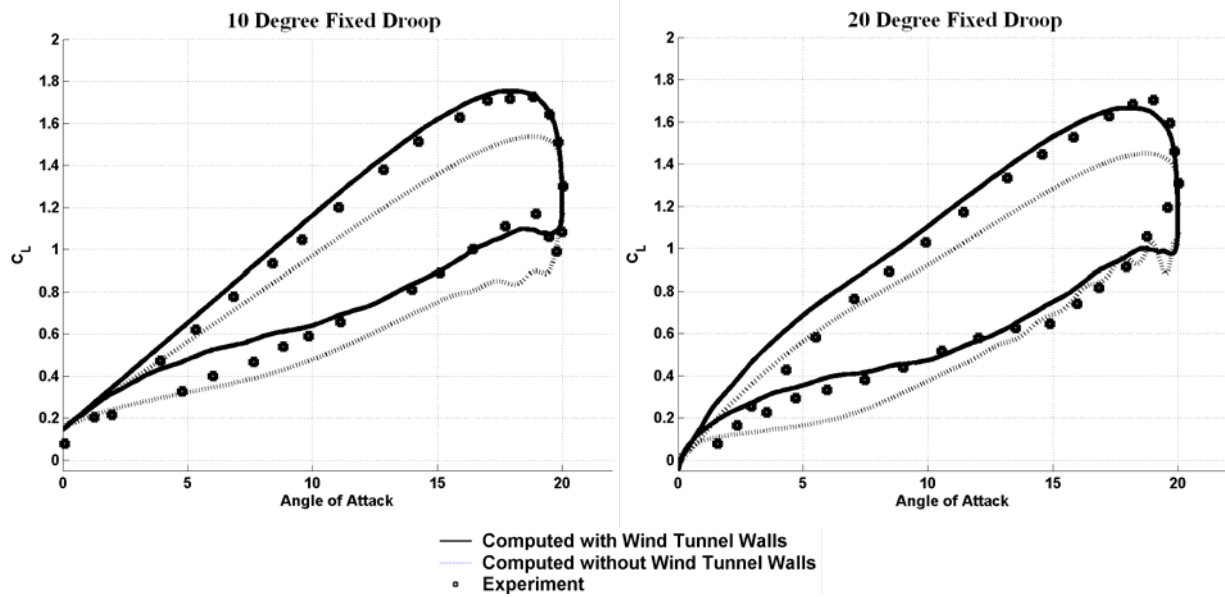
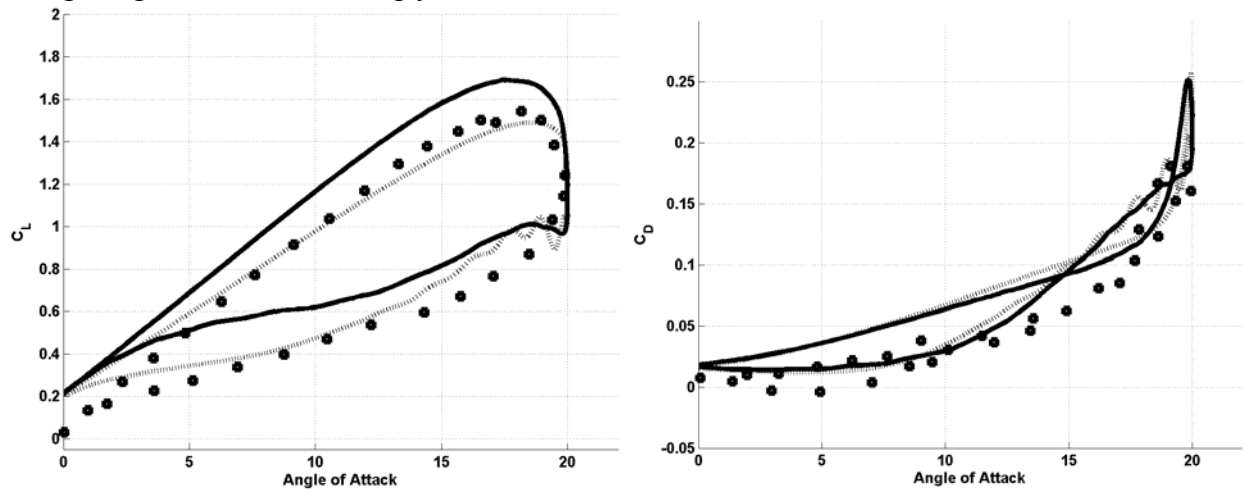


Figure 11. Comparison of Experimental and Computed Results for Fixed Droop VR-12
 $M=0.3, k=0.1, \alpha=10^\circ + 10^\circ \sin(\omega t)$

Next the VDLE airfoil was tested. The droop schedule is such that the first quarter chord of the airfoil is always at zero degrees angle of attack. The results with and without the wind tunnel walls are shown in Figure 12. The inclusion of wind tunnel walls improves the prediction of the lift curve slope but there is a steady offset of lift equal to the lift of the baseline airfoil at zero degrees. At zero degrees angle of attack, the VDLE airfoil has the same shape as the baseline VR-12. The computed results for the VDLE airfoil show similar lift values at low angle of attack to the baseline VR-12 but the experimental results have a near zero value. The pitching moment at high angle of attack is strongly underestimated.



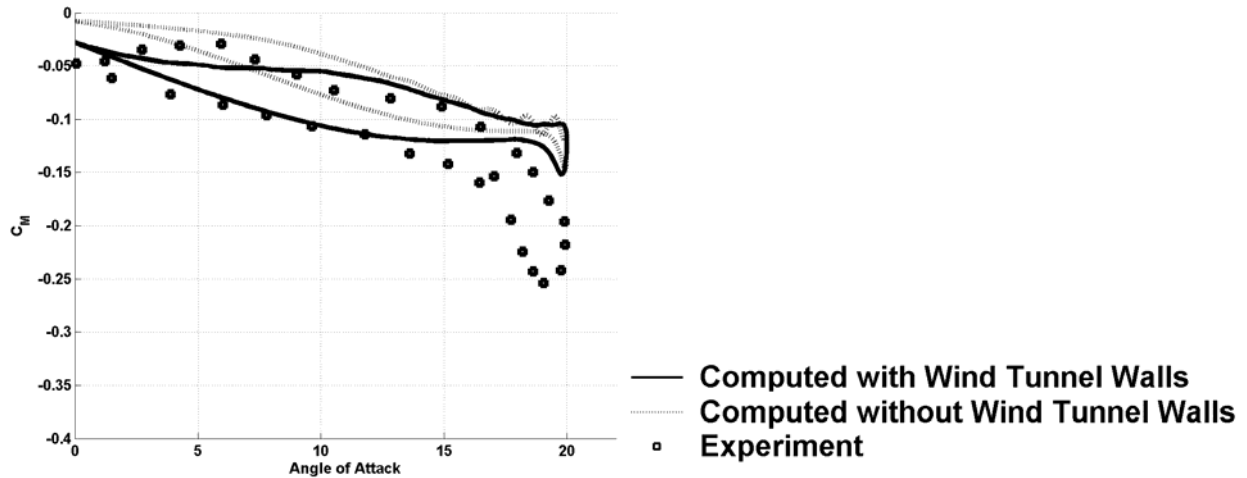


Figure 12. Comparison of Experimental and Computed Results for the VDLE Airfoil
 $M=0.3, k=0.1, \alpha=10^\circ + 10^\circ \sin(\omega t)$

Mach contours are compared at 18.5 degrees on the upstroke in Figure 13. As in the experiment, there is a small pocket of supersonic flow on the baseline airfoil but the shock is not strong enough to cause separation. The maximum Mach number for the VDLE airfoil is significantly reduced from 1.063 to 0.642. The leading edge of the VDLE airfoil is at low incidence and has a much weaker C_{pmin} of -3.16 compared with -8.38 of the baseline airfoil. The C_p distribution at 19.5 degrees is shown in Figure 14. The dynamic stall vortex evident in the baseline image has been suppressed by the VDLE airfoil. The effect of the VDLE airfoil on peak lift, drag, and moment are summarized in Table 1. The VDLE has significantly decreased the peak drag and pitching moment with minor reduction in peak lift.

Table 1. Effect of VDLE VR-12 Airfoil on Critical Quantities

	Experiment	Computed
Peak C_L Reduction	8%	5%
Peak C_D Reduction	63%	57%
Peak C_M Reduction	31%	49%

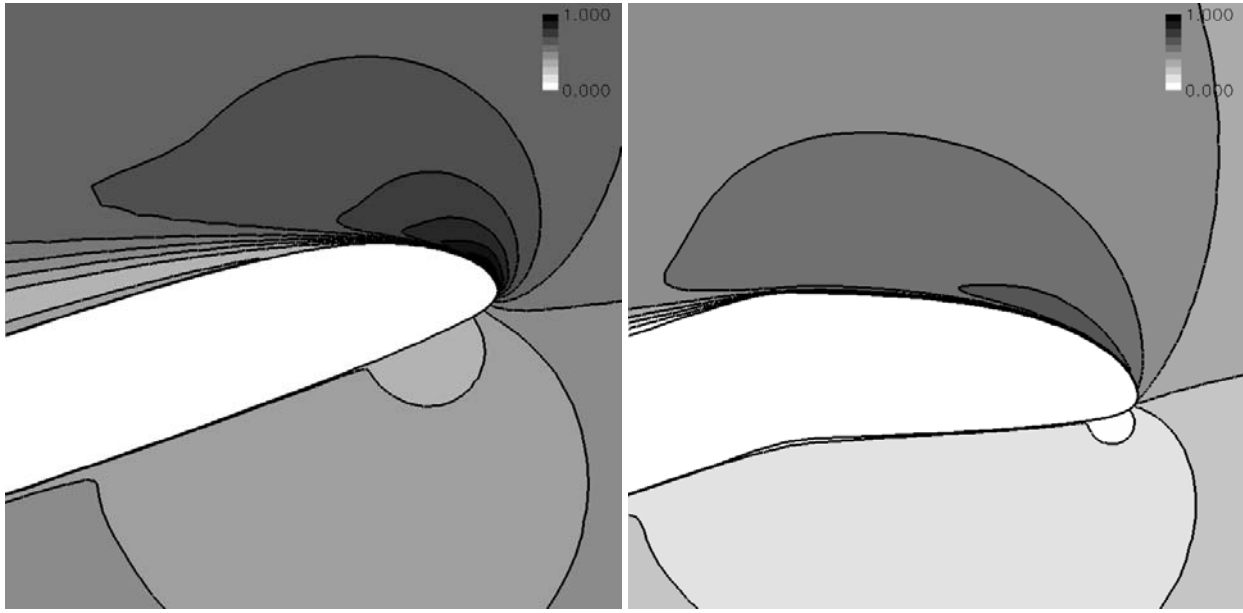


Figure 13. Mach Contours of VR-12 (left) and VDLE (right) at 18.5 Degrees on Upstroke.

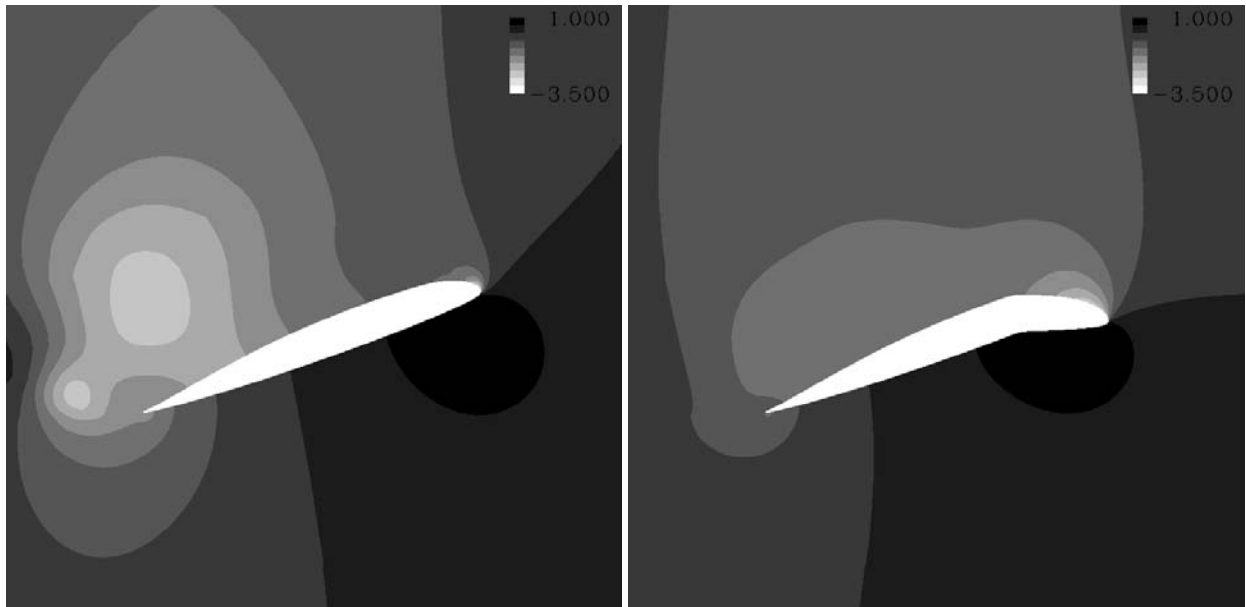


Figure 14. C_p Distribution of VR-12 (left) and VDLE (right) at 19.5 Degrees on Upstroke.

Next, the SC1095 airfoil was simulated. This airfoil along with the similar SC1094, are the airfoils on the UH-60A Blackhawk. There is a large database of computed and experimental results of this rotor for validation and comparison. The VR-12 is a more modern airfoil than the SC1095 with higher maximum lift and drag divergence Mach number. Results for the SC1095 in dynamic stall computations are shown in Figures 15 through 17. The VDLE droop schedule was

designed to maximize the $L^{3/2}/D$ on the upstroke using the results of the previous fixed droop runs as shown in Figure 18. The schedule maintains the baseline SC1095 airfoil from 0 to 5 degrees and then transitions to 15 degrees droop while keeping the angle of attack of the leading edge at 5 degrees. The effect of the VDLE airfoil on peak lift, drag, and moment are summarized in Table 2. The results are similar to the VR-12 tests except that the SC1095 shows an even greater computed drag reduction of 72% versus 57% for the VR-12. Figure 19 shows that the VDLE airfoil has successfully suppressed the leading edge separation that characterizes dynamic stall. The flow characteristics are very similar to the VR-12 tests. The lower incidence of the leading edge of the VDLE airfoil maintains attached flow even at very high angle of attack. Some separation does occur near the trailing edge of the main airfoil element but this region is significantly smaller than the baseline airfoils.

Table 2. Effect of VDLE SC1095 Airfoil on Critical Quantities

Peak C_L Reduction	15%
Peak C_D Reduction	72%
Peak C_M Reduction	58%

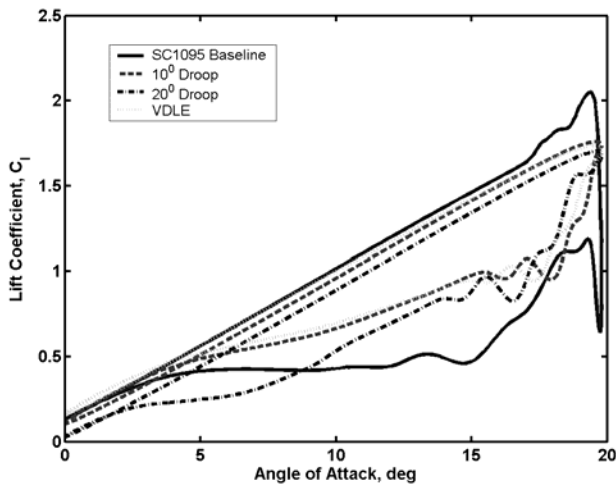


Figure 15. SC1095 Lift with Drooped Airfoils
 $M=0.3, k=0.1, \alpha=10^\circ + 10^\circ \sin(\omega t)$

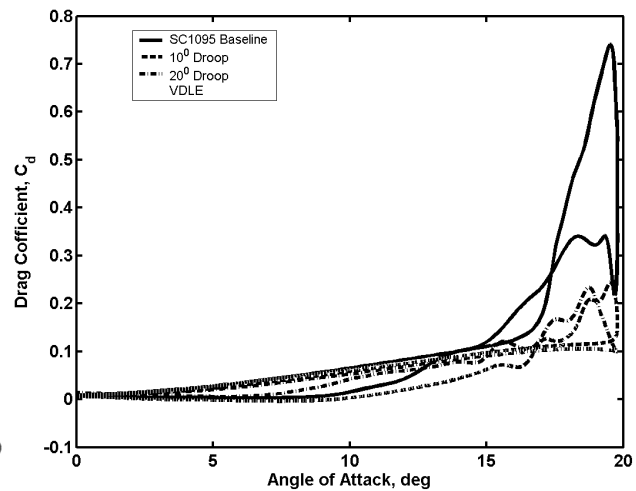


Figure 16. SC1095 Drag with Drooped Airfoils
 $M=0.3, k=0.1, \alpha=10^\circ + 10^\circ \sin(\omega t)$

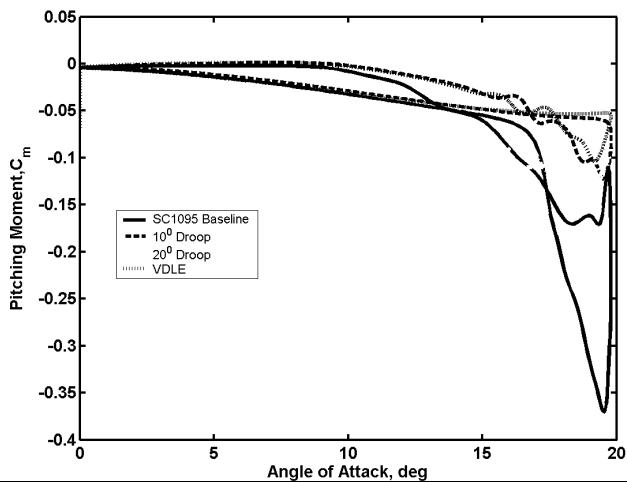


Figure 17. SC1095 Moment with Drooped Airfoils
 $M=0.3, k=0.1, \alpha=10^\circ + 10^\circ \sin(\omega t)$

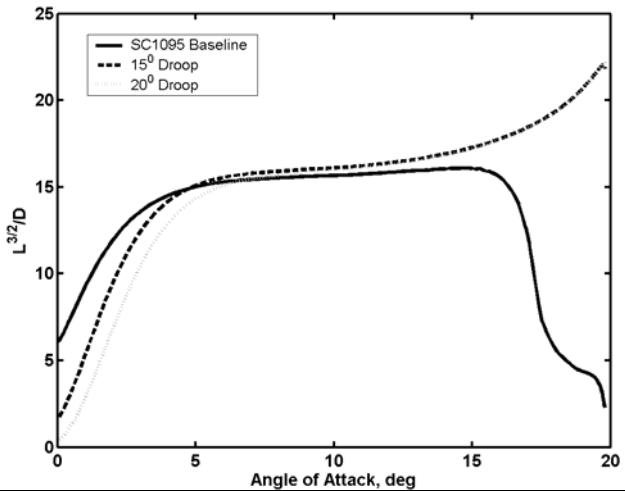


Figure 18. SC1095 Effect of Droop on $L^{3/2}/D$

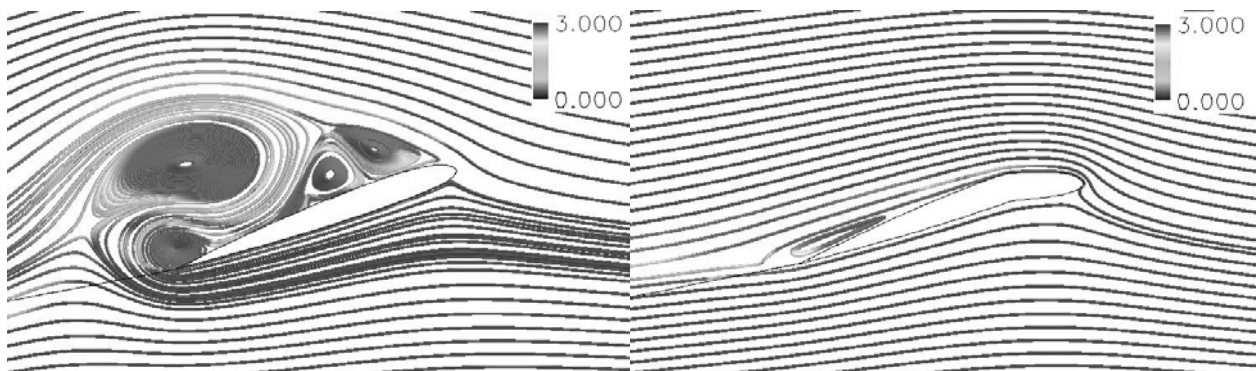


Figure 19. Instantaneous Streamlines around baseline SC1095 (left) and VDLE (Right) at 19 degrees on Upstroke Colored by Vorticity

Gurney Flaps:

Gurney flap is a 1 to 5 % of chord length device installed on the trailing edge. The flap deflects flow around the trailing edge, enhancing the circulation, with little incremental drag. Because a Gurney flap is small, light in weight, and may be deployed normal to the blade chord line with negligible moments at the hinges and linkages, a small low-power actuator such as a piezoelectric device may be used for deploying and retracting a Gurney flap.

Troolin et. al have investigated the effect of Gurney flap [27]. The configuration tested is a NACA 0015 airfoil equipped with several heights of Gurney flap at the trailing edge. An angle of attack sweep was performed and the lift coefficients were reported. The flap height of 2% of the chord length was chosen for the present validation study. The Mach number and Reynolds number were 0.05 and 2.1×10^5 , respectively.

Figure 20 shows a representative Gurney flap configuration and the associated body-fitted grid. Figure 21 shows the computed and measured lift vs. alpha characteristics computed using the Georgia Tech in-house flow solver, GENCAS.

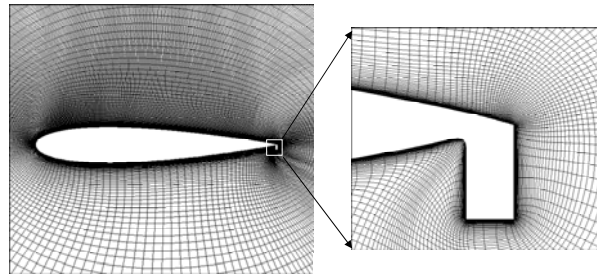


Figure 20. Grid system for NACA 0015 with 0.02c Gurney Flap (524×134 Grid)

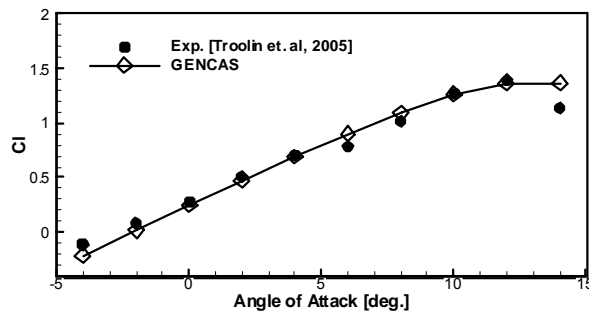


Figure 21. Comparison of lift coefficient: NACA 0015 with Gurney Flap

Dynamically deployed Gurney Flaps:

Prior to its application to the three dimensional rotor blades, the dynamically deployed Gurney flap was tested in a 2-D airfoil to determine the air load response. A NACA 23012 airfoil, representative of the airfoil used in the HART-II blade, was selected. Gurney flaps were deployed on the lower and upper surfaces of the airfoil at 90% chord. The length of the flap was varied with the following function:

$$l_{GF} = l_{GF-\max} \sin(2kM_{\infty}t)$$

Where, M_{∞} is the reference Mach number, and k is the reduced frequency. A positive value for l_{GF} represents a lower side deployment, while a negative value indicates an upper side deployment. The reference Mach number and reduced frequency were selected so that the analysis simulates the baseline descent mode of the HART-II rotor. The corresponding reference Mach number was 0.64 (hover tip Mach number of the blade). The reduced frequency was 0.121 for four-per- rev deployment and 0.242 for eight-per-rev deployment. The maximum Gurney flap length was limited to 1% of the airfoil chord length to reduce the sectional drag penalty and reduce nose-down sectional pitching moments.

Grid Independence Study for the Modeling of Deployable Gurney Flap:

Since the deployable Gurney flap is simulated using dynamic wall boundary condition, the grid resolution along the Gurney flap is of concern in establishing the model's accuracy. Two sets of grids in the vicinity of the Gurney flap were tested. Figure 22 shows the grid around

Gurney flap. The fine grid system has more than twice the grid points along the flap as the baseline grid, and more grid points were placed upstream and downstream of the flap.

Figure 23 compares predicted delta-airloads from the two grid sets. Here, the term “delta-airload” refers to the incremental load (lift, drag, or pitching moment) generated by the Gurney flap deployed airfoil relative to the baseline airfoil. The predictions from both grids compare well with each other. Spikes were observed in the drag coefficient, and it was greater with the coarse baseline grid. This is caused by the step change in the number of grid points over the flap as the flap is introduced into the flow and retracted. The spikes are reduced with a finer grid since the cell size is smaller, the step changes are small and the wall boundary condition is turned on in more smooth and gradual manner. However, the low frequency content of the drag values on the two grid systems is quite similar. The lift variation was smooth in both grid systems, and the pitching moment variation shows a small fluctuation due to the drag oriented moment. Based on this study, a grid similar to the baseline grid was used in all subsequent 2-D and 3-D computations.

Unsteady Airloads Response to the Dynamically Deployed Gurney Flap:

Dynamic deployment of Gurney flap causes unsteady variations in the sectional loads. This includes phase lag and delta magnitude of airloads relative to the steady state air loads. Identifying the temporal (or phase) lag between the Gurney flap deployment and the air load response is important in establishing a Gurney flap schedule.

Figures 24 and 25 show the airloads with deployed Gurney flap at reduced frequencies of 0.121 and 0.242. In the delta- C_l plot for $k=0.121$, it is clearly seen that the zero, maximum and minimum lift occur with a 38.5 degree (0.1069 cycle) phase lag from the flap schedule. In comparison, the phase lag was about 55 degree (0.153 cycle) for the $k=0.242$ case. However, drag variation follows the flap schedule without noticeable phase lag because the flap deployed normal to the flow leads to a nearly instantaneous loss in momentum, unlike the lift generation that requires flow settling time to build circulation. The phase-lag for the pitching moment was somewhat between the lift and drag phase lags due to both of their contribution to the moment. A noticeable decrease in the magnitude of the lift is also observed with the higher frequency flap deployment, similar to classical unsteady aerodynamics where an increase in frequency leads to a reduced lift and moment response.

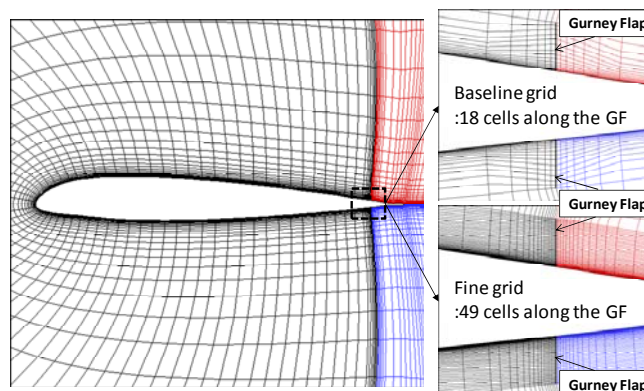


Figure 22. Gurney flap grid resolution

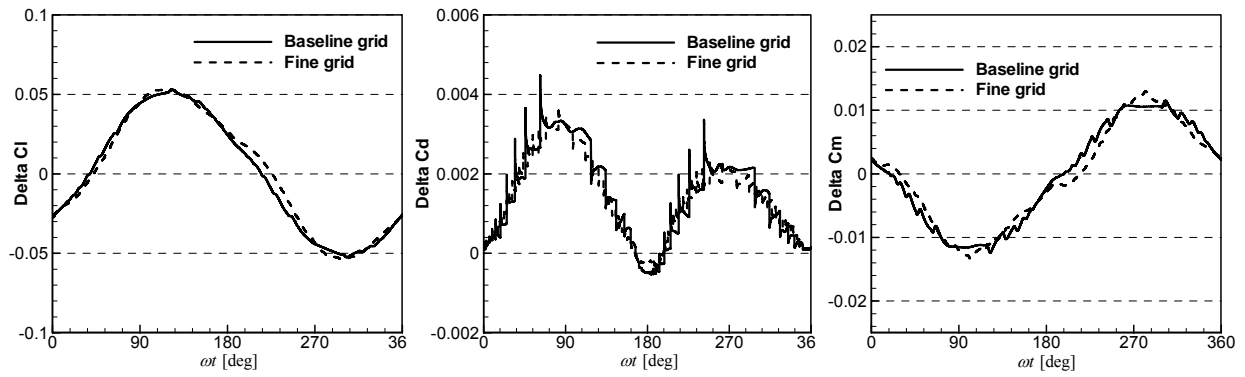


Figure 23. Delta-airloads comparison of two grid systems

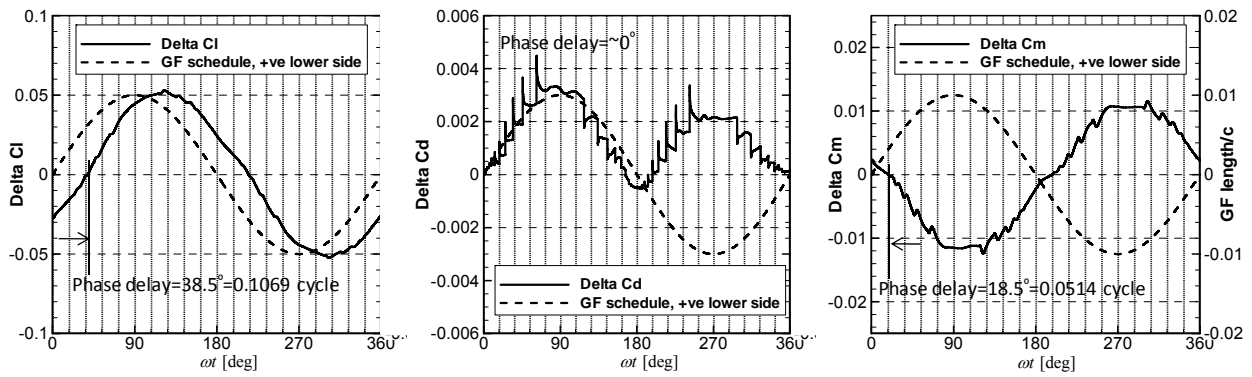


Figure 24. Delta-airloads: $k=0.121$ (4 per Rev.)

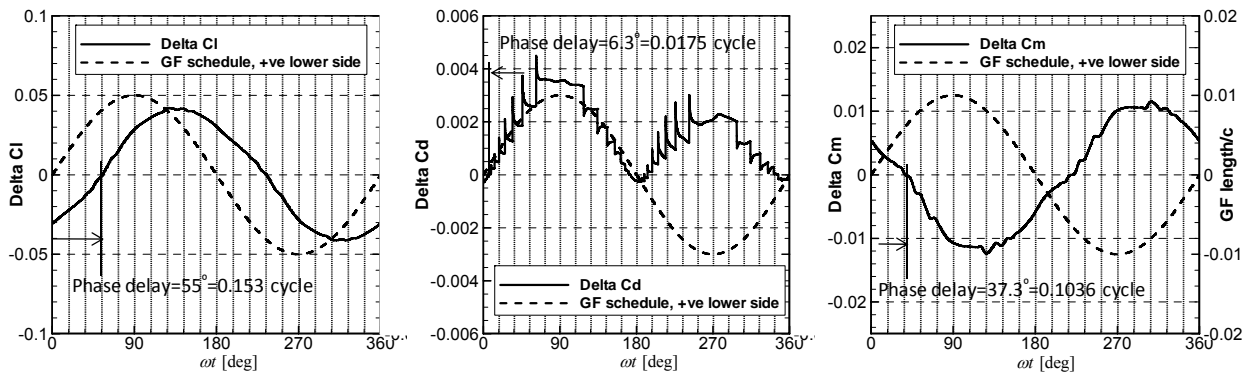


Figure 25. Delta-airloads: $k=0.242$ (8 per Rev.)

3-D Studies of deployable Gurney Flaps

3-D studies were also carried out to understand how the effectiveness of OBC concepts is influenced by radial flow, time-dependent freestream velocity, and losses at the edge of devices. Because helicopter rotors are flexible, the interplay between the structural deformations and aerodynamics is important. In these studies, this was accounted for using a loosely coupled CFD/CSD approach where the CFD analysis (OVERFLOW or Georgia tech in-house solver GENCAS) is coupled to DYMORE, a multi-body dynamics solver developed at Georgia Tech.

The four-bladed HART-II rotor model is used as a representative rotor [28]. The flight condition corresponds to a forward flight descent mode with advance ratio of 0.15 and a hover tip Mach number of 0.64. A harmonic deployment of Gurney flaps is used, aimed at minimizing the four-per-rev harmonic vertical vibratory load while mitigating adverse effects such as high sectional pitching moments and hub moments.

Four-Per-Rev Deployment of Gurney Flaps:

A multi-block grid system shown in Figure 26 is used, with Gurney flap installed at 90% chord-wise location. Prior to deploying the Gurney flap, the baseline descent condition was simulated using GENCAS-DYMORE coupled analysis and the trimmed state was established. Starting with the trimmed baseline rotor flow field as the initial condition, Gurney flap was deployed and the coupled analysis was continued to reach trimmed state. The phase angle of the Gurney flap schedule was specified based on the 2-D studies discussed earlier, so that the delta-lift due to Gurney flap aims to cancel out the 4P vibratory load of the baseline rotor (Figure 27). A phase lag was based on the 2-D analyses discussed earlier was included in the specification of the flap deployment. The radial placement of the flap was adjusted to minimize the target vibratory loads. The final Gurney flap schedule was obtained after several adjustments and is shown in Figure 28.

The GENCAS-DYMORE loosely-coupled analysis was continued in time from the trimmed baseline rotor with the scheduled Gurney flap deployment. The rotor was re-trimmed after every few rotor revolutions, and the blade elastic motion updated. Figure 29 shows the trim history of the rotor with Gurney flap. It is seen that the trim process drives the rotor hub loads (thrust and moments) to the same values as the baseline rotor.

Although the Gurney flap schedule was rigorously determined by including the response time lag, the resultant hub load at the beginning of Gurney flap deployment will somewhat differ from the desired load distribution due to 3-D and unsteady inflow effects. This is seen in Figure 30, which compares the 4P vertical load for the baseline rotor and the Gurney flap-equipped rotor before a re-trim. The desired 4P load cancellation was not achieved. This is attributable to the non-uniform delta-load production from the Gurney flap at each azimuth angle in forward flight due to varying dynamic pressure. It may be noted that the force coefficients are non-dimensionalized based on the blade tip speed, not the local flow velocity. Figure 31 shows delta-load distribution immediately after Gurney flap is deployed (Iteration #11) following a re-trim. On the advancing side, the high dynamic pressure produces a large delta-load. On the retreating side, the Gurney flap is not as effective due to the lower dynamic pressure. As a result, moment unbalance occurs as shown in the trim history plot (Figure 29). The re-trimming process re-

distributes the load so that the adjusted pitch control compensates for the delta-load differences in the advancing/retreating and fore/aft sides of the disk due to Gurney flap. Once the rotor is re-trimmed, the delta-loads following the re-trimming are shown in Figure 31b.

The summation of delta-load of four blades, located with 90 degree azimuth angle phase shift is shown in Figure 32. Before the re-trim, Gurney flap produced a skewed and phase shifted delta-load instead of the expected clean sinusoidal shape. After the re-trim, the desired delta-loads with proper phase angle and a near sinusoidal shape was obtained. Figure 33 shows the vertical hub loads at the hub and the filtered 4P hub load. It is evident that the vertical hub load is more evenly distributed and 4P vertical hub load is greatly reduced from the original state.

Additional studies have been done to adjust the width and radial position of the Gurney flap. In Figure 33b, an alternate flap schedule, with the flap spanning the 70% to 74% radius is shown. With this radial placement, a small increment in the delta-loads was seen compared to the original flap placement (between 70% and 73% radius). The sensitivity of the vertical hub loads to the span of the flap and the radial placement indicates that the four-per-rev vertical load may be reduced with an optimized flap placement and flap length.

Gurney flap are known to generate high nose-down local pitching moments. In the current study, the local pitching moments and their effect on the blade torsional deflection were examined. Figure 34 shows the local pitching moment distribution. As a result of the small size of the flap coupled with 3-D relief effects, the effect of Gurney flaps on elastic torsional deflection (in the vicinity of $r/R=0.7\sim 0.73$) was negligible as shown in Figure 35.

Figure 36 compares vibratory side forces and hub moments. The incremental changes in H-force, Y-force and pitching moments at the hub, attributable to the Gurney flaps, were negligible. Although the vibratory rolling moment increased relative to the baseline rotor, the Gurney flaps had one order of magnitude less impact on hub rolling moment coefficients than on vibratory vertical hub load coefficient.

Individual Blade Control of 4P & 8P Vibratory loads:

A further benefit of deployable Gurney flap as a control concept is that the segmented flap can be controlled individually (IBC). This section examines the potential for Gurney flaps for reducing higher harmonic components of vibratory loads.

In an attempt to reducing the eight-per-rev components of the vertical hub loads, the previous 4P deployment at separated flap segments was modified with the addition of an eight-per-rev schedule of the flap. The radial placement of the flaps, and the flap schedule was adjusted. The final schedule is shown in Figure 37. Since the resultant change in the thrust and hub moments was negligible with this additional 8P deployment, re-trimming process was not necessary.

The 8P vertical hub loads shown in Figure 38 demonstrate a significant reduction in vibratory loads compared to the previous cases. Table 3. summarizes rotor performance and vibration level of the four-per-rev and 4+8 per rev concepts. The 4P vertical hub load of the 4P Gurney flap deployed rotor was reduced to the 17% of the baseline rotor, and the 8P vertical load of the simultaneous 4P and 8P Gurney flap deployed rotor was reduced to the 4% of the baseline rotor.

These improvements were achieved while the trim state was maintained with negligible performance penalty (L/D_e).

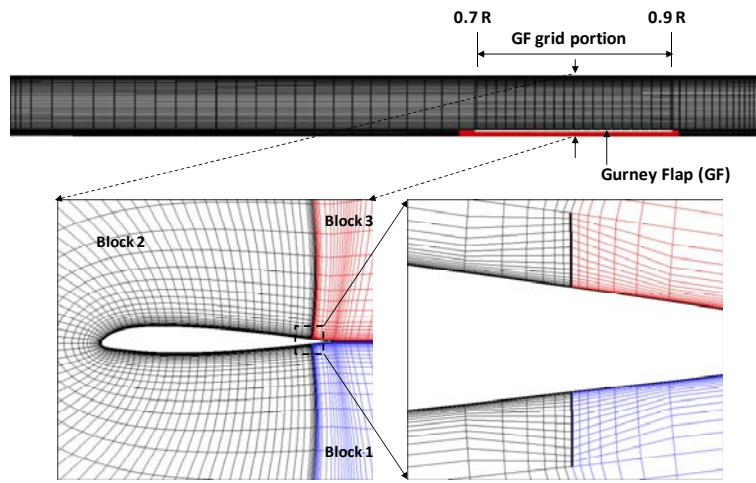


Figure 26. Grid system for Gurney flap simulation

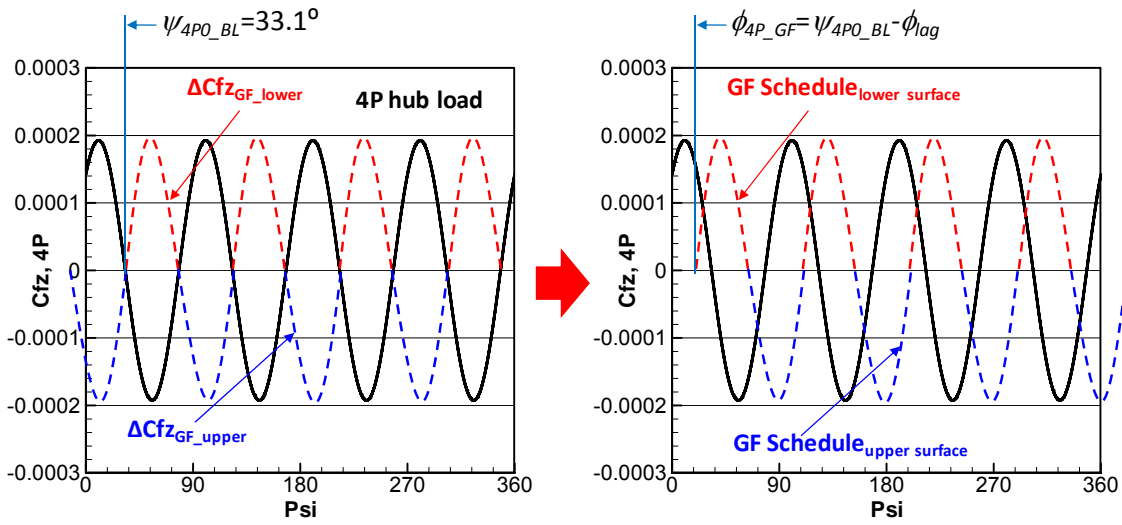


Figure 27. 4P Vertical hub load of the baseline rotor and initial Gurney flap schedule

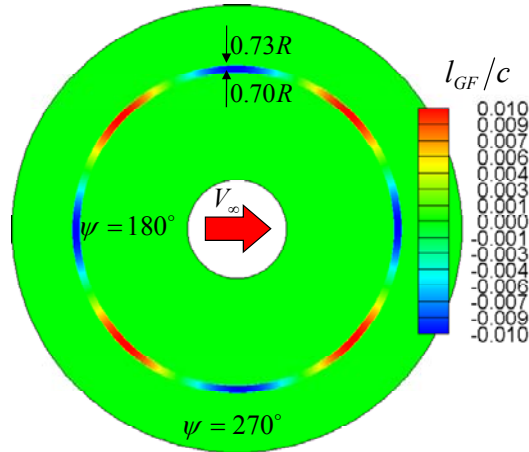


Figure 28. 4P Gurney flap schedule (+: lower surface, -: upper surface)

$$(l_{GF} = A \sin(n(\psi - \phi_{4P_GF}))), \text{ where } n=4, A=0.01c, \text{ and } \phi_{4P_GF} = 23.5^\circ$$

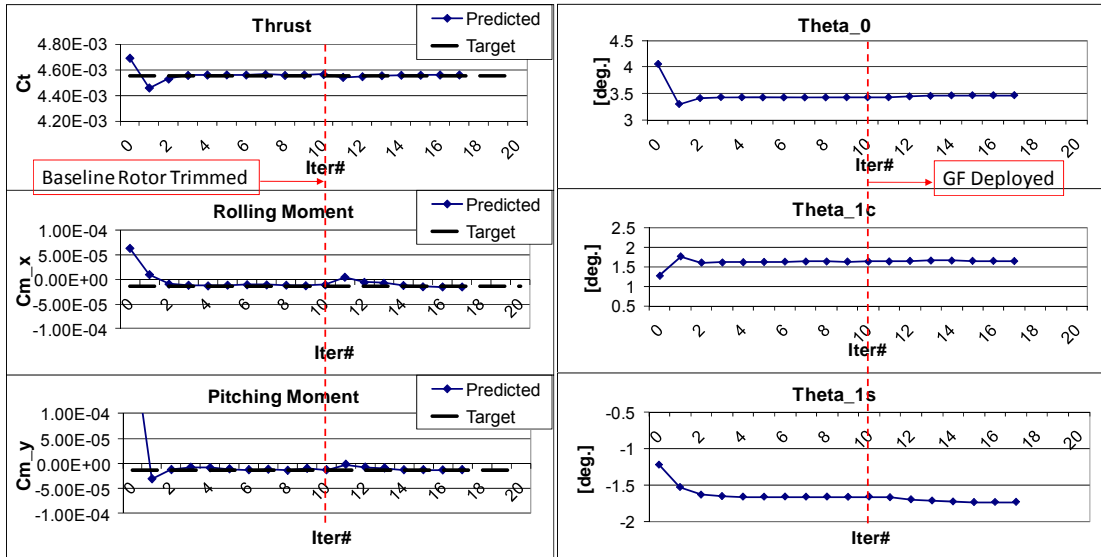


Figure 29. Trim history of the Gurney flap deployed rotor

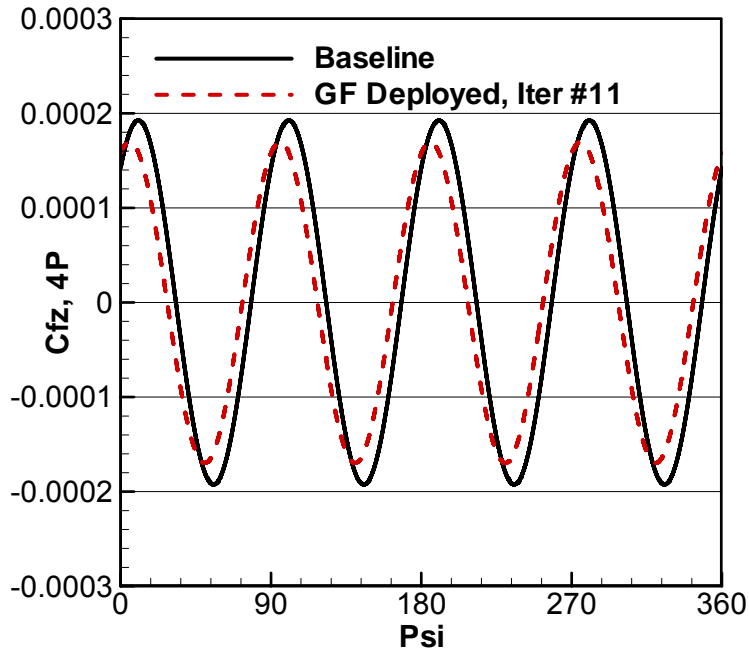
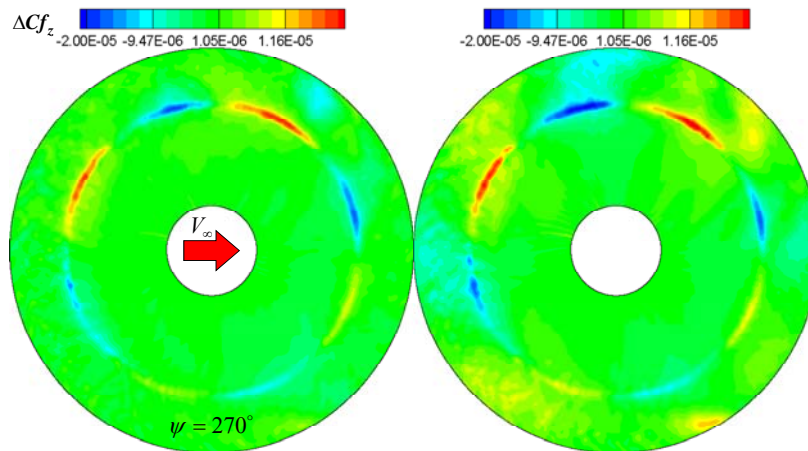


Figure 30. 4P vertical hub load comparison, (baseline vs. GF rotor before re-trimming)



a) Before re-trimming (Iter. #11) b) After re-trimming (Iter. #17)
 Figure 31. Delta vertical force due to Gurney flap ($\Delta C_{f_z} = C_{f_z} - C_{f_z_baseline}$)

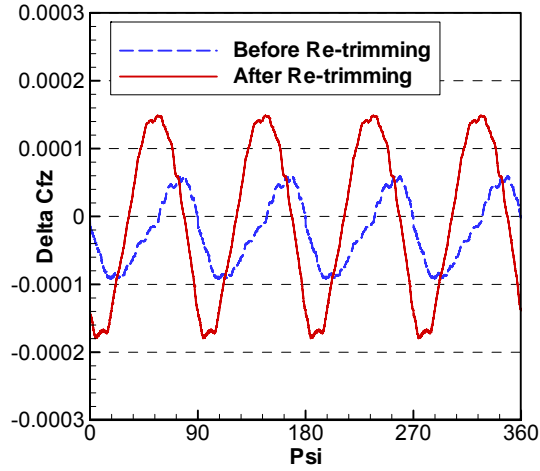
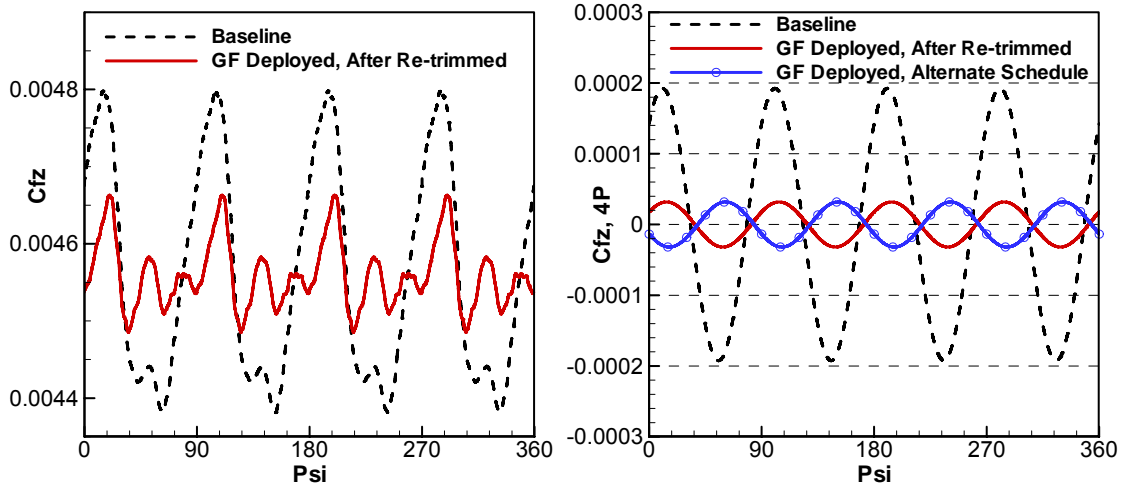


Figure 32. Delta hub load due to Gurney flap before/after re-trimming



a) Total vertical hub load

b) 4P Vertical hub load

Figure 33. Vertical hub load comparison, baseline vs. GF rotor after re-trimmed

(Alternate GF schedule: $\phi_{AP_GF} = 25^\circ, r/R_{GF} = 0.7 \sim 0.74$)

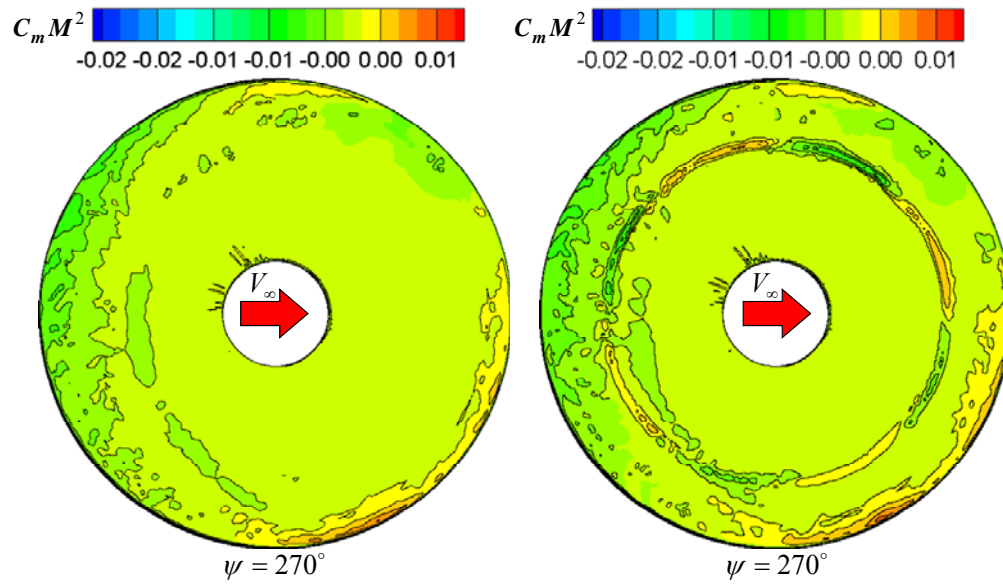


Figure 34. Local pitching moment distribution

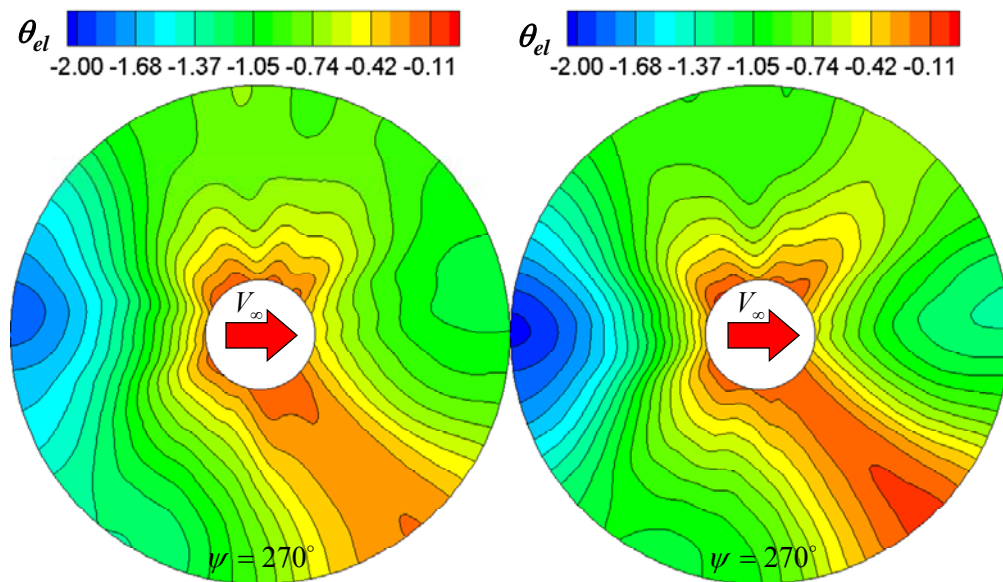


Figure 35. Blade torsional deflection comparison (Elastic deformation only, angle in degree)

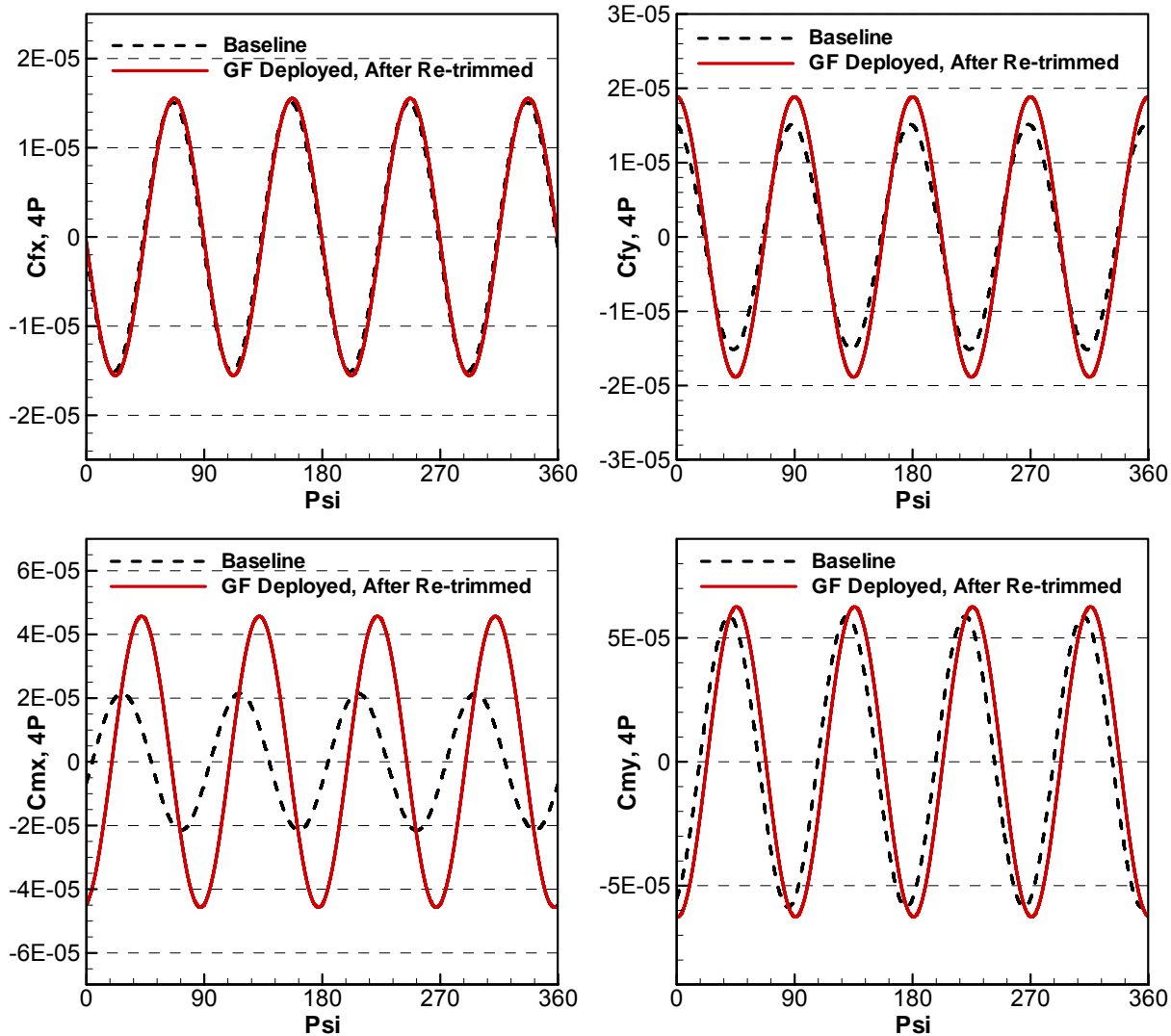


Figure 36. 4P hub load comparisons

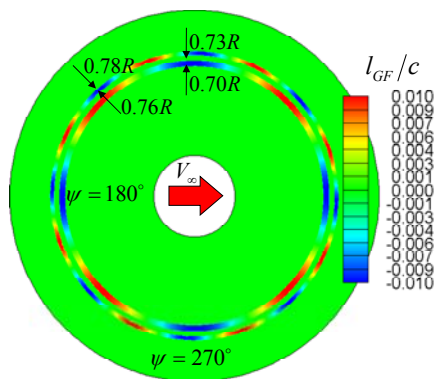


Figure 37. 4P and 8P Gurney flap schedule (+: lower surface, -: upper surface)

$$(l_{GF_4P} = A \sin(n_{4P}(\psi - \phi_{4P_GF})), l_{GF_8P} = A \sin(n_{8P}(\psi - \phi_{8P_GF})))$$

Where, $n_{4P} = 4$, $n_{8P} = 8$, $A=0.01c$, $\phi_{4P_GF} = 23.5^\circ$ and $\phi_{8P_GF} = 8^\circ$

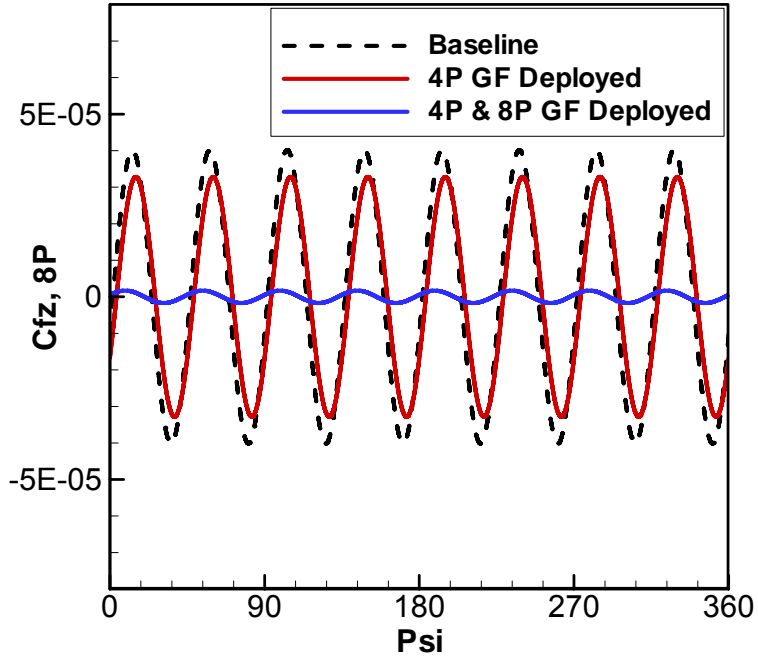


Figure 38. 8P vertical hub load comparison

Table 3. Rotor performance and vibratory load ($L/D_g = L/(D + \frac{N_G R}{V_G})$)

	<i>GF Deployed</i> (4P Harmonic)	<i>GF Deployed</i> (4P & 8P Harmonic)
$C_T/C_{T, BL}$	1	1
$\Delta C_{Mx} = C_{Mx} - C_{Mx, BL}$	-4.21×10^{-6}	3.54×10^{-6}
$\Delta C_{My} = C_{My} - C_{My, BL}$	1.29×10^{-7}	4.84×10^{-6}
$(L/D_g)/(L/D_g)_{BL}$	0.99	0.98
$(F_{z, 4P})/(F_{z, 4P})_{BL}$	0.17	0.18
$(F_{z, 8P})/(F_{z, 8P})_{BL}$	0.82	0.04

3-D Studies of VDLE based UH-60A Rotors

To assess the effects of drooping leading edge devices in 3-D applications, the UH-60A Blackhawk rotor was used. Analysis of helicopter rotors in forward flight is a complex multidisciplinary problem. Rotor blades are flexible beams that undergo significant elastic deflection. To solve the elastic deflections and trim the rotor to the required thrust, rolling, and pitching moment, several Comprehensive Structural Dynamics (CSD) codes have been developed. The features and development history of these codes are summarized in [29]. They require the sectional structural properties of the rotor blade and details of the hub system. These properties determine the elastic characteristics of the rotor and interact with the aerodynamic forces. Accurate modeling of the aerodynamics of rotors is extremely challenging due to requirement to model unsteady transonic flow with shocks, dynamic stall, reversed flows, and wakes. CSD codes rely on simplified aerodynamics from table lookups, stall models, and wake models. The aerodynamic calculations can be improved using a CFD code to supplement the internal aerodynamic calculation through CFD-CSD coupling but at approximately two or three orders of magnitude increase in computational cost. Extensive work has been done on the UH-60A rotor using CFD-CSD coupling with a variety of solvers through the UH-60A Airloads Program [30]. Potsdam et al [31] used loose coupling with OVERFLOW and CAMRAD II for a variety of level flight conditions. OVERFLOW has also been used with other structural solvers including RCAS [32] and DYMORE [33].

DYMORE is a finite element solver which uses a multi-body dynamics approach for the modeling of the rotor as a nonlinear elastic multi-body system. A four bladed UH-60A rotor model is used that includes the blades, lag dampers, and push rods. A dynamic wake is used for the initial aerodynamics. An auto pilot algorithm is used to trim the rotor to the prescribed thrust and moment targets. This model has been used in previous studies using OVERFLOW [31] and GT-HYBRID [34]. No changes were made to the DYMORE model to account for the VDLE mechanical device.

A loose coupling trim method initially developed by Tung et al [35] was used. DYMORE is first run using lifting line aerodynamics for several revolutions to obtain the trim solution and blade motions. The elastic blade motions are then transferred to OVERFLOW. The three forces and three moments in the hub frame are then calculated by OVERFLOW. This avoids any differences in the local frame due to changes in chord length and orientation that occurs when the leading edge is deformed. Airloads and elastic deformations were calculated at eighty-one rotor stations. The first exchange of airloads from OVERFLOW to DYMORE took place after a periodic solution was obtained from two full rotor revolutions. Subsequent iterations passed airloads after two or three quarter-revolutions. Since airloads are exchanged at every degree of azimuth, care is required to ensure that the OVERFLOW loads have reach periodicity to avoid discontinuities. DYMORE uses the OVERFLOW loads and applies a small trim correction using table lookup aerodynamics. Typically 6-10 iterations are required to converge to the desired thrust, rolling, and pitching moment. DYMORE ran for approximately four hours per iteration. OVERFLOW was run on an eight node 2.4 GHZ AMD Athlon Processor cluster on 3-16 processors. Approximately 8 hours per revolution are required when using 16 processors.

Flight C9017 was used. This is a moderate speed (advance ratio $\mu = 0.237$) high thrust case that has two dynamic stall cycles. The two stalls occur at approximately $\psi = 270^\circ$ and $\psi = 330^\circ$.

The first stall is due to the high control angles necessary for the high thrust and the second stall is caused by the elastic deformation due to the torsion dynamics. The standard UH-60A rotor was run for seven CFD-CSD coupling iterations to converge to the desired thrust, rolling moment, and pitching moment targets. The results are similar to results report by Potsdam [31] except these computations use a coarser grid which does not capture all the events. The results are compared with experimental data in Figures 39-41 at several span stations. The first stall is slightly under predicted which leads to a significant under prediction of the second stall. Due to the coarse off-body grid spacing of 0.2 chords, the wake is significantly dissipated resulting in loss of the high frequency content in the aft portion of the rotor disk. It has been previously noted that the integrated thrust is 13% higher than the measured thrust. The pitching moments are plotted with mean removed to eliminate the effect of steady state offset.

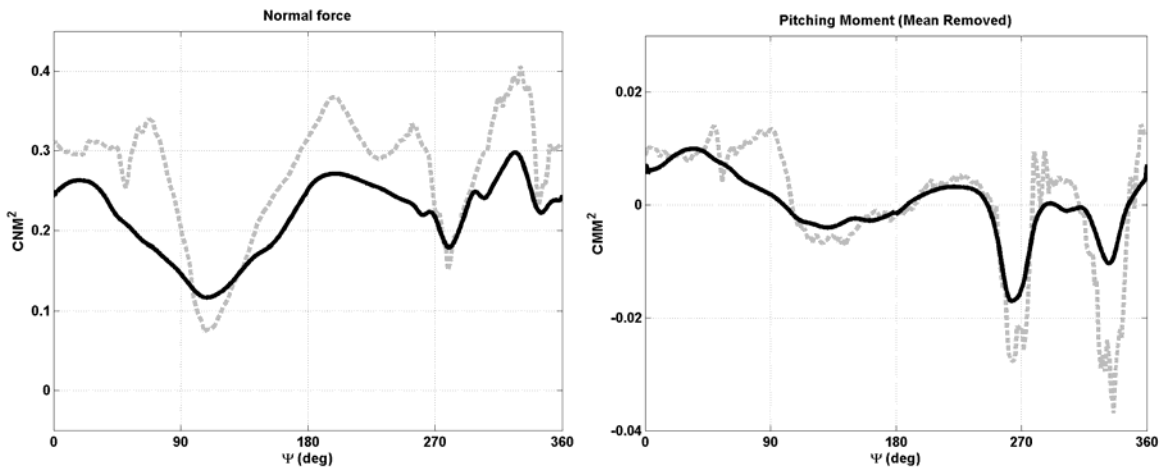


Figure 39. Sectional Loads at 0.865 r/R --- Experiment — Computed

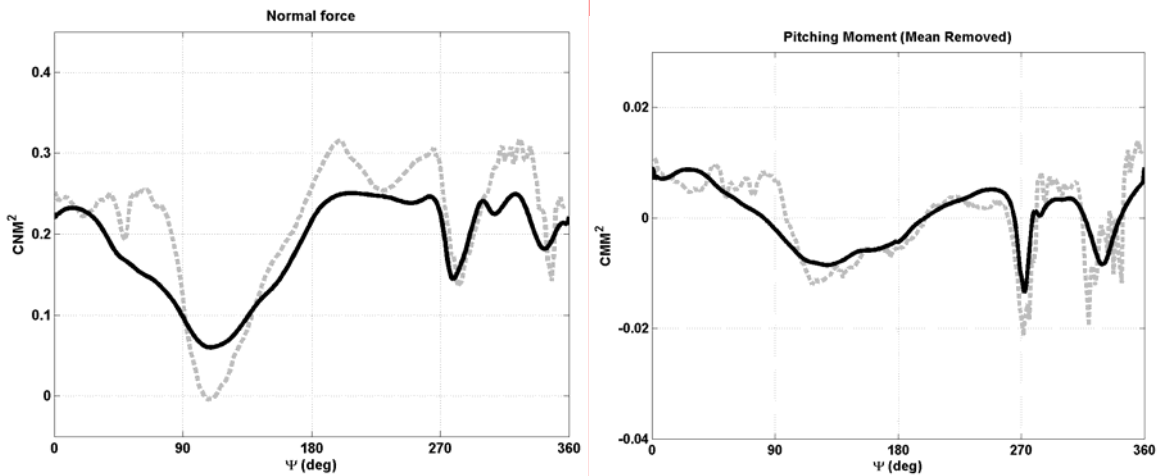


Figure 40. Sectional Loads at 0.920 r/R --- Experiment — Computed

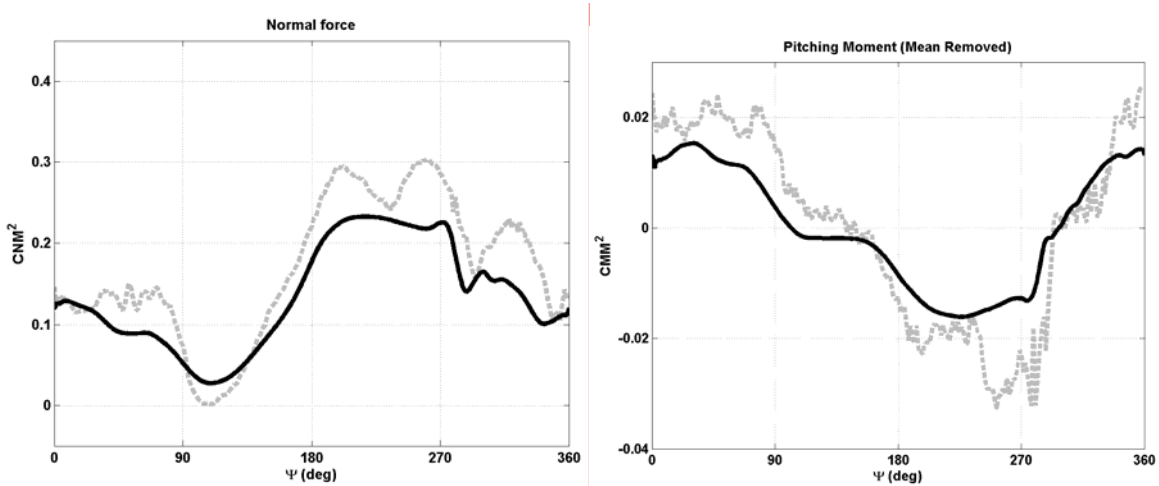


Figure 41. Sectional Loads at 0.990 r/R **---** Experiment **—** Computed

A droop schedule was designed to reduce the effect of the two stalls on the outer portion of the rotor. The extent of the VDLE airfoil part of the blade was limited to 25% of the span from $r/R=0.7$ to 0.95 . The minimum feasible amount of time for the actuator to go from no deflection to a maximum of 15° was taken from a requirement for a VDLE mechanical system from an Army SBIR that specified the mechanism be capable of 5/rev motion [31]. The droop schedule was implemented using a slower 4/rev motion that began to droop at $\psi=220^\circ$ achieving a maximum of 15° droop at $\psi=265^\circ$. A maximum droop of 15° was chosen based off the SC1095 computations. The leading edge returns to the undeformed shape from $\psi=305^\circ$ to $\psi=350^\circ$ as shown in Figure 42.

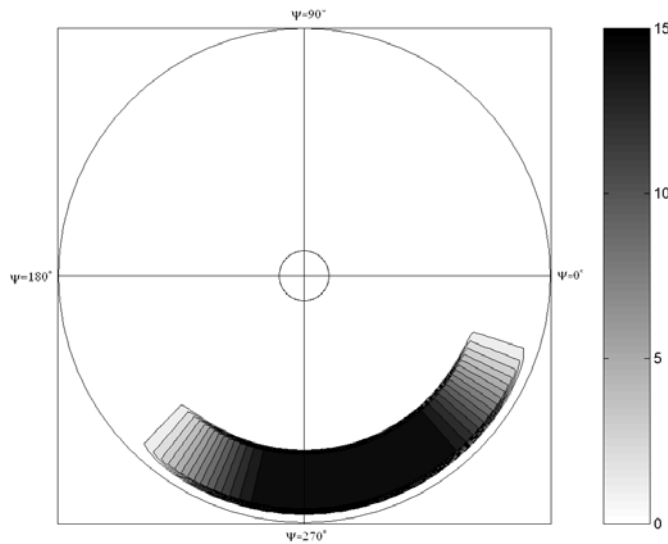


Figure 42. Droop Schedule Implemented for C9017

The VDLE based rotor was run for seven CFD-CSD coupling iterations to converge to the thrust, rolling moment, and pitching moment targets. The total and elastic pitch at the tip of the rotor blade is shown in Figure 43. The pitch is nearly identical on the advancing side as that the collective and cyclic values are within 0.1° of each other. The VDLE section has an increased nose down pitching moment when the VDLE section begins to droop at $\psi=220^\circ$ and the

maximum pitch at the tip at $\psi = 305^\circ$ is reduced by nearly 2° . Due to the elastic nature of rotor blades, the increased pitching moment in the VDLE section when it begins to droop affects the pitch of the entire blade. Figures 44 - 46 show the results for sectional pitching moment, normal force and chord-wise force polar plots. The discontinuity in the loads at $r/R=0.7$ and $r/R=0.85$ is due to the increased chord with the tab. Figure 47 shows the local sectional loads at $r/R = 0.9$. The advancing side of the rotor for both cases is very similar with only slight differences in the trim state. The VDLE based rotor increases the pitching moment when it begins to droop at $\psi = 220^\circ$ but the large spike in moment in the baseline rotor at $\psi = 270^\circ$ from the dynamic stall has been eliminated. The magnitude of the second stall has also been reduced. From the polar plot, a higher pitching moment is evident over the wide area where the rotor droops but maximum magnitude has been reduced. The pitching moment is significantly increased and the normal force is decreased for the VDLE blade around $r/R=0.7$ where the VDLE section begins. This indicates that the leading edge has drooped too much at this span station and that the VDLE section does not need to extend this far inboard. Experimental data near this region shows a stall begins around 220° that was not captured in the baseline computations.

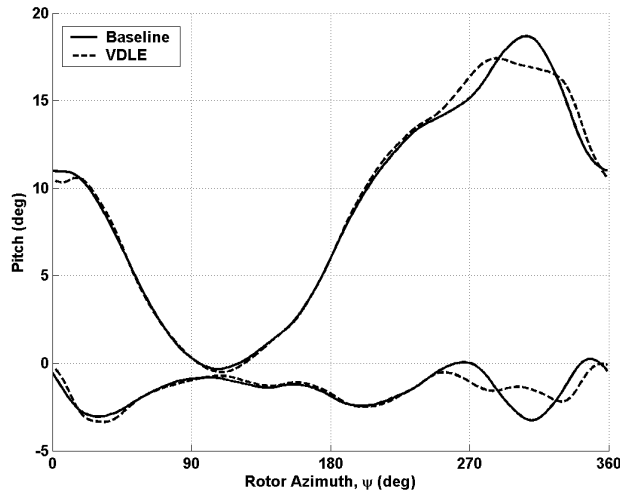


Figure 43. Comparison of Total and Elastic Pitch at Tip of Blade for the Baseline and VDLE Rotor

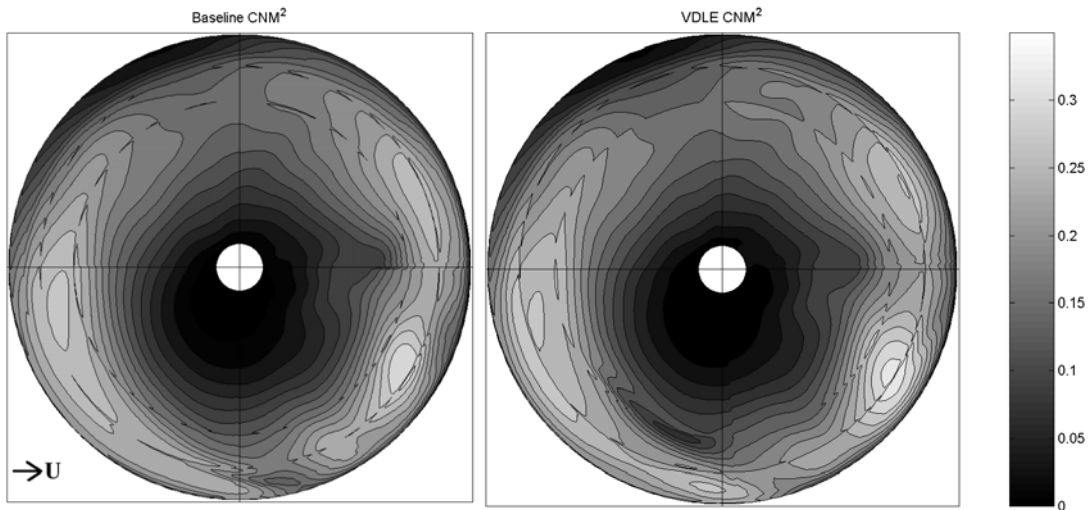


Figure 44. Local Normal Force Polar Plots

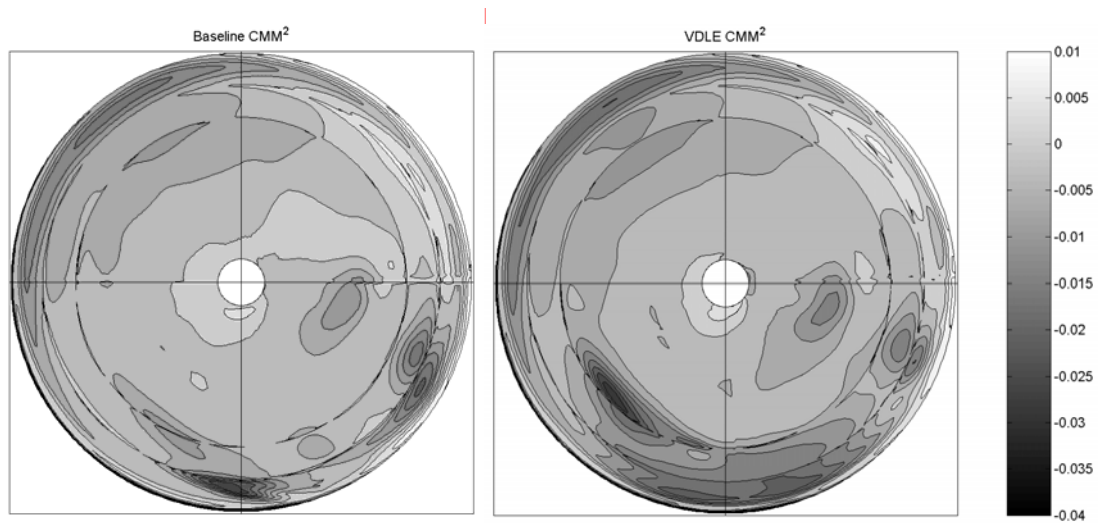


Figure 45. Local Pitching Moment Polar Plots

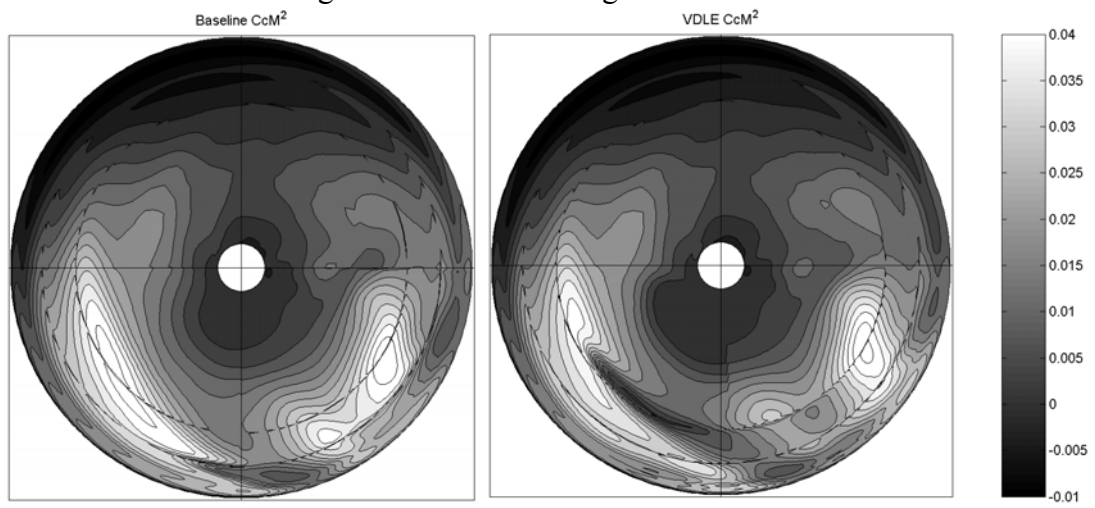


Figure 46. Local Chordwise Force Polar Plots

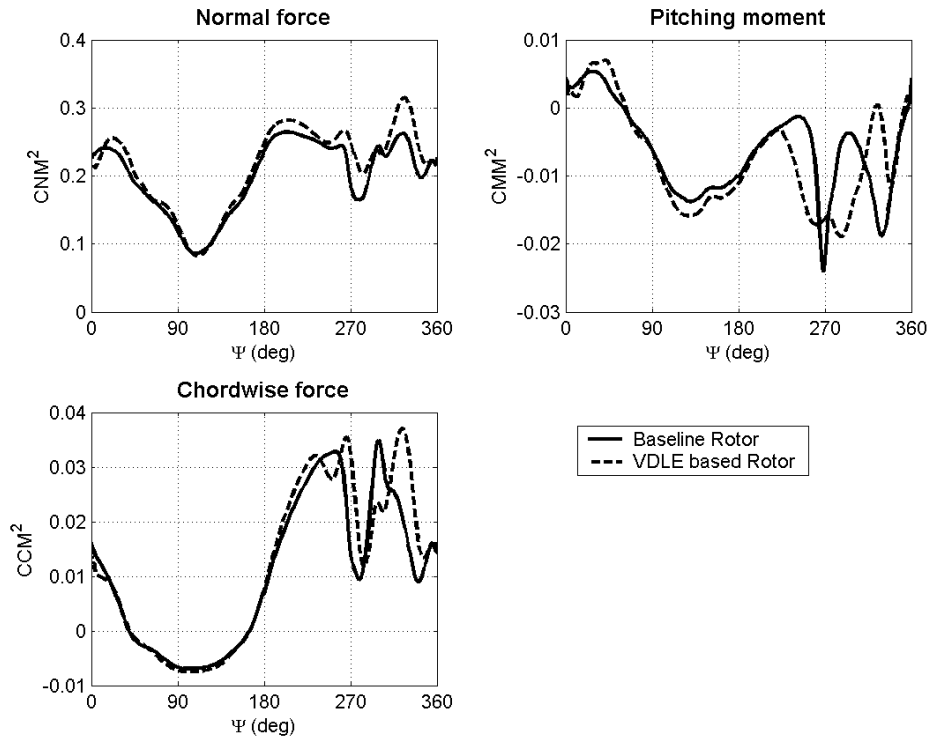


Figure 47. Sectional Loads Forces at $r/R=0.9$.

The effect of the VDLE blade on the stall at $\psi=270^\circ$ is shown in Figures 48 and 49 using an iso-surface of constant vorticity. The baseline blade has a large pocket of separated flow on the upper surface of the blade that is not present for the VDLE blade. The vorticity for the VDLE blade is confined to the tip vortex and over the attached boundary layer. The flow remains attached or very mildly separated over the entire rotor disk for the VDLE blade.

The two rotors were compared using the effective lift to drag ratio, L/D_e . The VDLE based rotor had a 2.9% improved L/D_e of 3.49 from 3.39 of the baseline rotor. This is mainly due to a 3.3% reduction in the torque required to power the main rotor. The edge force of the VDLE based rotor was less than the baseline rotor resulting in less propulsive force.

It is instructive to examine how the effect of the VDLE airfoil on local pitching moment and normal force effects the vibration. A primary contributor to vibration is the 4/rev vertical force component. The VDLE blade had a 7.96% reduction in 4/rev vertical force component. A 4/rev motion of the VDLE section of the blade for the entire rotor disk could potentially significantly reduce the vibration.

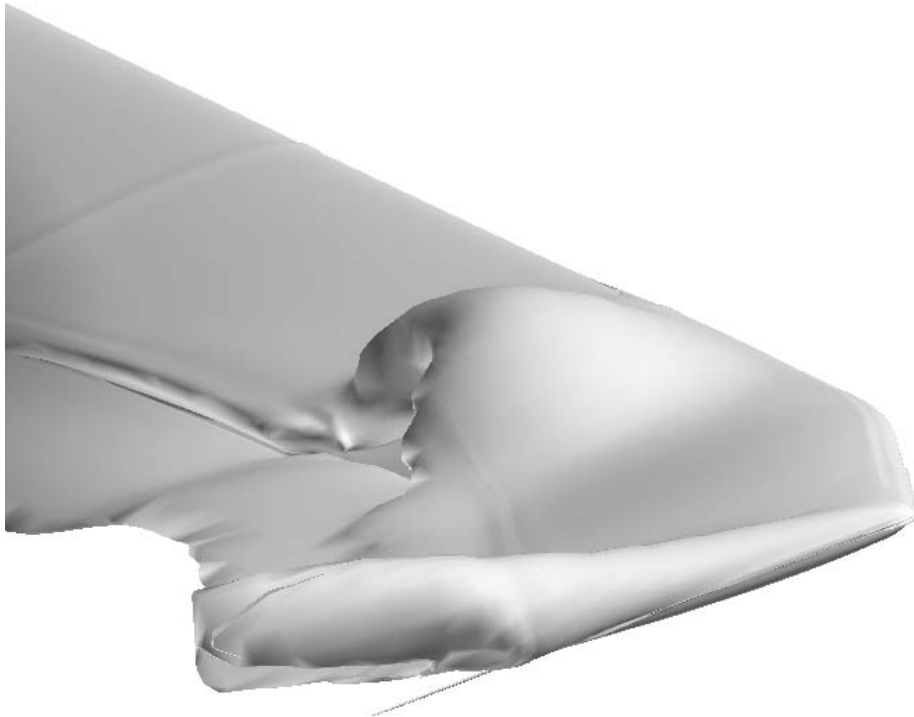


Figure 48. Iso-Surface of Constant Vorticity at $\psi=270^\circ$ on Baseline UH-60A Blade.

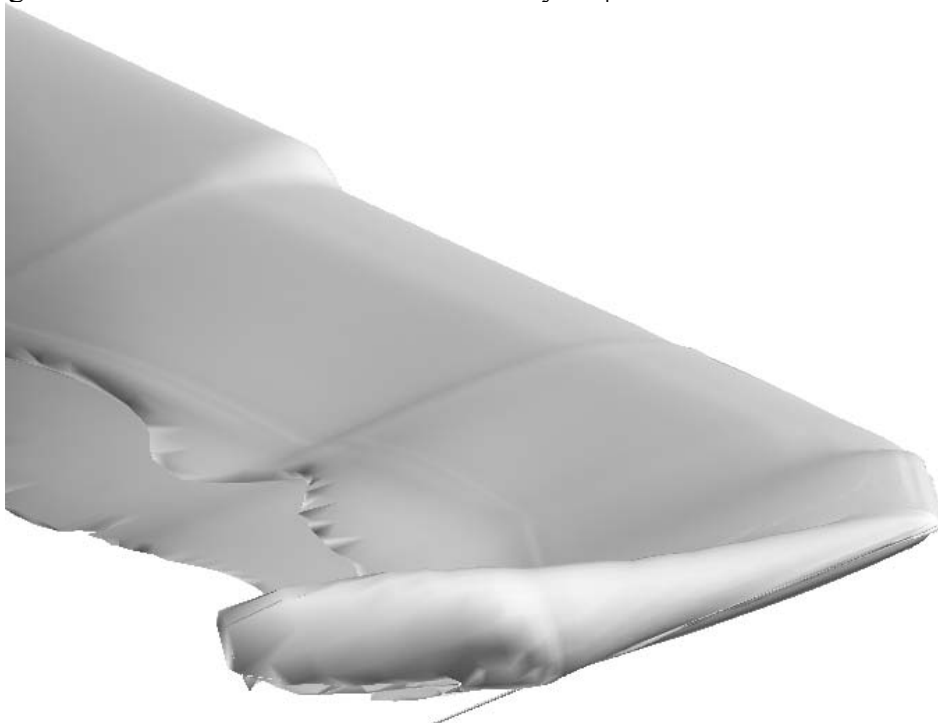


Figure 49. Iso-Surface of Constant Vorticity at $\psi=270^\circ$ on VDLE Based UH-60A Blade

TASK 2. DEVELOPMENT OF REDUCED ORDER MODELS

The objectives of this task are to:

- Develop a data base of the impact of selected OBC concepts on blade aerodynamics from available test data and from high fidelity CFD simulations of a limited set of configuration parameters.
- Develop reduced order models that capture the essential physics of the impact of selected OBC concepts on blade aerodynamics and evaluate prediction accuracy through comparisons with high fidelity CFD results and available test data.

During the course of this study, three approaches were explored.

Superposition of Indicial Response

In this approach calculations are done to extract the indicial response of actuation concepts for a range of mean flow conditions. The gain (i.e. increase in 2-D lift, drag, pitching moments) per unit actuation is extracted. The time constants that account for time lag between the actuation and response are also extracted. The unsteady effects due to the actuation are superposed over steady airloads using Duhamel integrals.

This approach works well when the indicial response is linear, i.e. proportional to the actuation amplitude. In transonic flows, and in stalled flows, a small deflection of the actuator surface may produce a large non-linear aerodynamic response. Furthermore, the nonlinear response may be opposite in magnitude and sign to the actuator deflection. For example, in transonic flow, a small downward deflection of the flap intended to increase lift may cause strengthening of the shock wave over the airfoil surface and trigger shock induced stall. For these reasons this approach was not pursued.

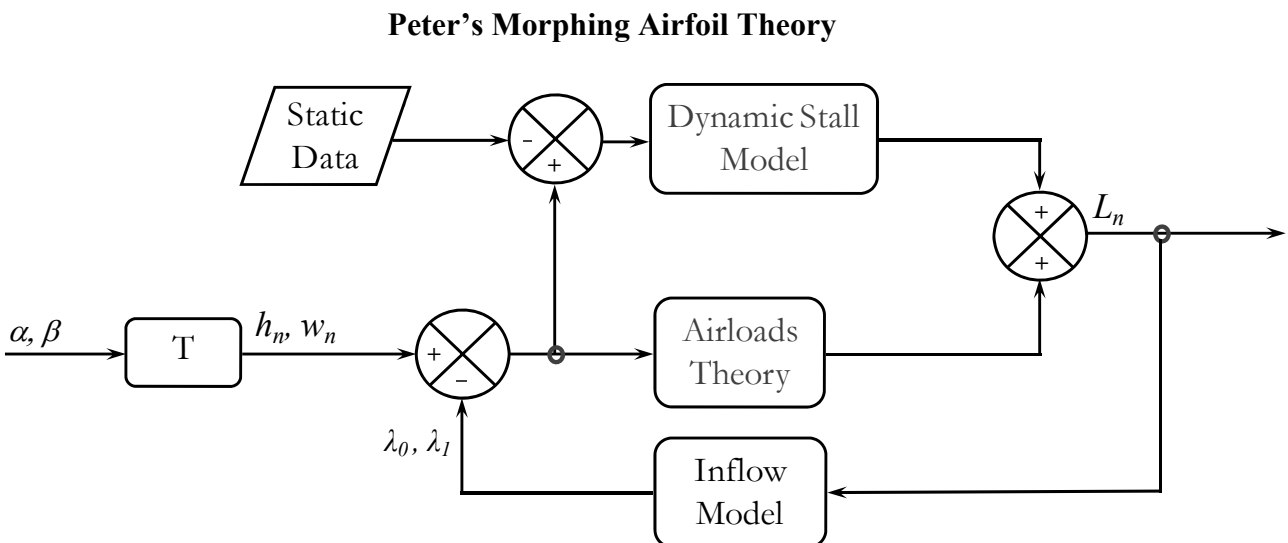


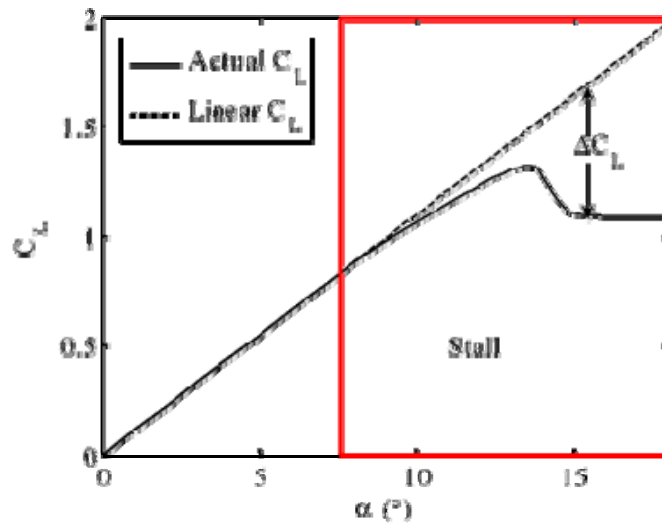
Figure 50. Schematic of Airfoil Morphing Model.

A schematic of the model is shown in Figure 50. The airfoil motions are transformed into generalized coordinates. These coordinates drive the airloads theory. As vorticity is deposited into the flow, it affects the downwash velocity that the airfoil sees. For this reason, an inflow model incorporated in a feedback loop. These linear loads are then compared with the static data, which drive the dynamic stall model. These three effects (static airloads, unsteady airloads from a linear theory, and dynamic stall model) are combined to compute the total loads.

The dynamic stall model is based on the ONERA model, which hypothesizes that dynamic stall may be modeled as a transfer function based on wind tunnel data. ONERA has investigated what form that transfer function should take. In the stalled regime, a second order transfer function is needed in order to capture the time delay of the vortex passage.

$$\ddot{\Gamma}_n + \eta \dot{\Gamma}_n + \omega^2 \Gamma_n = -\omega^2 \left[\Delta \Gamma_n + e \frac{\partial \Delta \Gamma_n}{\partial \theta} \theta^* \right]$$

ONERA proposed that the total loads could be separated into two parts. The linear portion, that follows the first order equation, and the dynamic stall, that follows a second order equation. The three constants in the above model ω , η , and e may be empirically extracted from static airloads data as shown in Figure 51.



$$\omega = \omega_0 + \omega_2 \Delta C_L^2$$

$$\eta = \eta_0 + \eta_2 \Delta C_L^2$$

$$e = e_0 + e_2 \Delta C_L^2$$

Figure 51. Extraction of Constants of a Second Order Model from Static Airloads Data.

Neural Network based Reduced order Models

The development of a reduced order model (ROM) was aimed at capturing the essential physics of the impact of selected OBC concepts on blade aerodynamics. A Neural Network (NNET) technique was adopted for the ROM derivation. Neural Networks, or artificial neural networks to be more precise, represent a technique that is rooted in many disciplines: neuroscience, mathematics, physics, computer science, and engineering [36].

Neural networks find widespread applications in such diverse fields as modeling and data processing. A neural network, made up of an interconnection of nonlinear neurons, is itself nonlinear. Nonlinearity is a highly important property, particularly for mapping rotorcraft aerodynamics, which are inherently nonlinear.

The reduced order model (ROM) for selected OBC concepts was developed based on the airloads database generated from the Navier-Stokes CFD simulations. The modern high fidelity CFD was first applied to evaluate the impact of selected OBC concepts on blade aerodynamics and create the airloads database accordingly. The airloads database for the OBC concepts of interest was developed with properly selected model variables. The database thus generated is then used to extract the reduced order model (ROM) through neural network technique [36]. The details of the CFD simulation and database generation were discussed in the previous section. The following describes the details of the formulated reduced order modeling framework that captures the essential dynamics and aerodynamics of the on-blade control concepts in consideration.

For OBC applications, the reduced order airloads model is formulated as a superposition of a baseline airloads model and the incremental difference between the baseline and the CFD simulation. The baseline airloads model can be a conventional engineering model without the effects of OBC. The incremental difference or the delta airloads is derived by subtracting the CFD results from the baseline airloads model and formulated as a NNET presentation. The following summarizes the formulation of the ROM.

- Baseline airloads model:

$$[\mathbf{C}_L \ \mathbf{C}_M \ \mathbf{C}_D]_{base} = f_{base}(\alpha, \dot{\alpha}, M)$$

- CFD data with OBC effects:

$$[\mathbf{C}_L \ \mathbf{C}_M \ \mathbf{C}_D]_{cfid} = f_{cfid}(\alpha, \dot{\alpha}, M, \delta, \dot{\delta})$$

- Difference between the CFD and the baseline:

$$\Delta[\mathbf{C}_L \ \mathbf{C}_M \ \mathbf{C}_D]_{OBC} = [\mathbf{C}_L \ \mathbf{C}_M \ \mathbf{C}_D]_{cfid} - [\mathbf{C}_L \ \mathbf{C}_M \ \mathbf{C}_D]_{base}$$

- NNET approximation of $\Delta[\mathbf{C}_L \ \mathbf{C}_M \ \mathbf{C}_D]_{OBC}$:

$$\Delta[\mathbf{C}_L \ \mathbf{C}_M \ \mathbf{C}_D]_{nnet} = f_{nnet}(\alpha, \dot{\alpha}, M, \delta, \dot{\delta})$$

- Reduced order model (ROM):

$$[\mathbf{C}_L \ \mathbf{C}_M \ \mathbf{C}_D]_{ROM} = f_{nnet} + f_{base}$$

For implementation, a quasi-unsteady airloads model in FLIGHTLAB was used as the baseline reference. The CFD simulation was performed for a range of α , $\dot{\alpha}$, M , δ , and $\dot{\delta}$. The incremental airloads were then computed from the differences between the CFD and the baseline. The baseline reference airloads model selected for the implementation does not include any effect of OBC devices. Therefore, the incremental airloads thus derived reflect both the effects of OBC and differences between the baseline airloads model and Navier-Stokes based high fidelity CFD simulation. Figure 52 below illustrates the NNET formulation for the ROM that reflects the OBC effects.

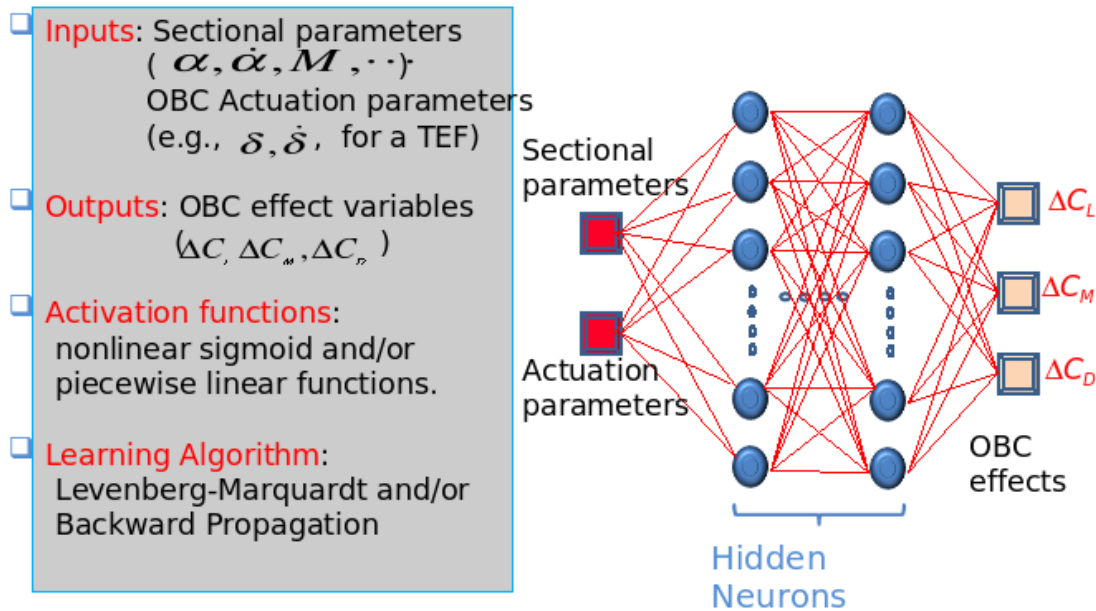


Figure 52. Reduced Order Model based on Neural Network

The NNET model training is a very time consuming task. By organizing the lift, drag, and pitch moment coefficients into three individual NNET modules, both the NNET model training effort and accuracy were dramatically improved.

Results and Discussion

Calculations were done to develop each of the above three approaches.

Indicial response Approach:

In this approach, the steady state over the airfoil is first obtained. A step change to the OBC device resulting in small changes to angle of attack, leading slat, or trailing edge flap was applied. The evolution of the sectional lift, drag, and pitching moment were analyzed to extract the gains (i.e. change in lift, drag, or pitching moment per unit change in the actuation amplitude) and time constants.

Figures 53 through 56 show sample results for the gain in lift and drag, due to active twist and flap deflection, for a range of freestream Mach numbers and mean angles of attack.

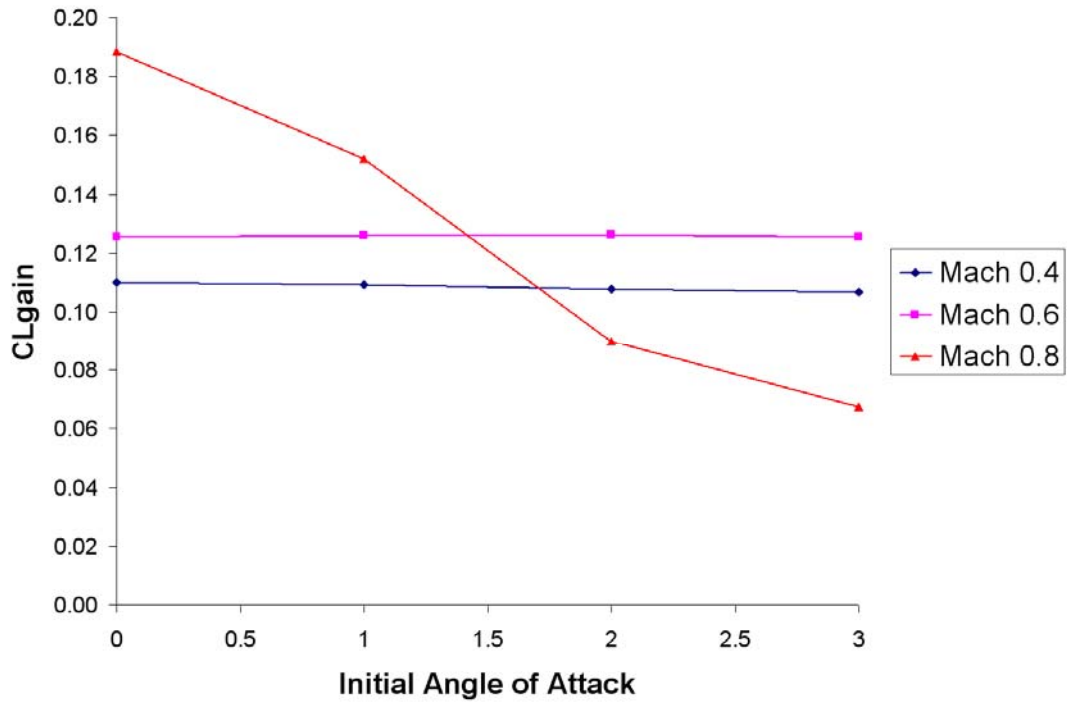


Figure 53. Step C_L Gain per degree of twist

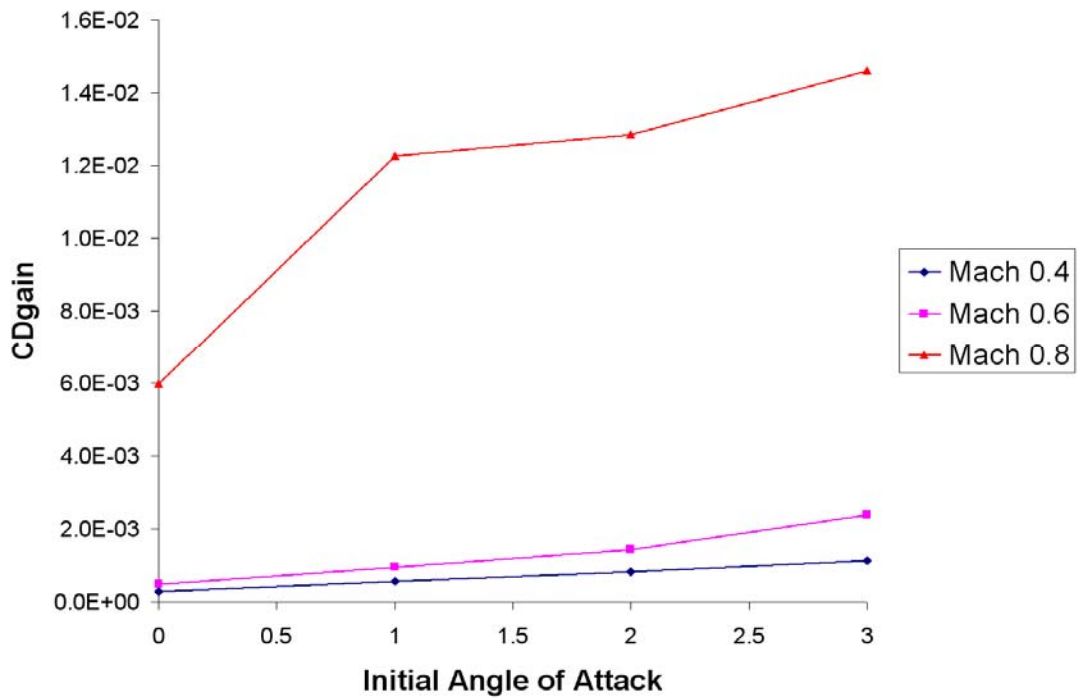


Figure 54. Step C_D Gain per degree of twist

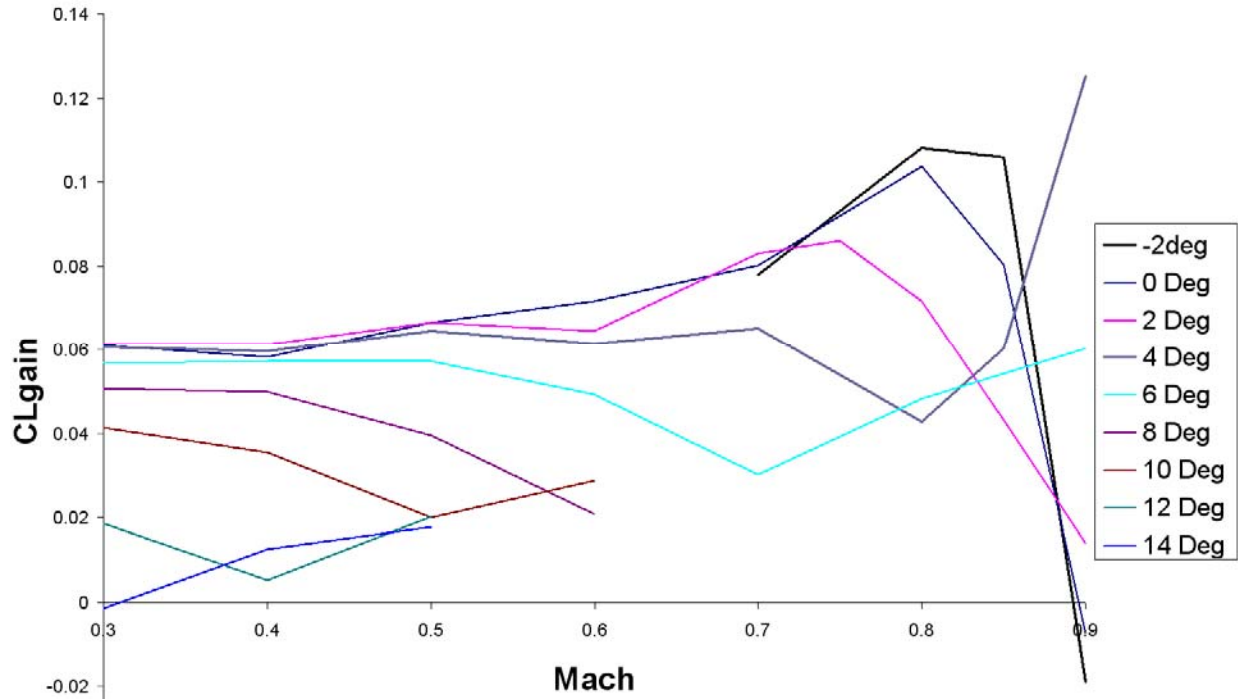


Figure 55. Step C_L Gain per degree of flap deflection for Various Mean Angles and Mean Alpha

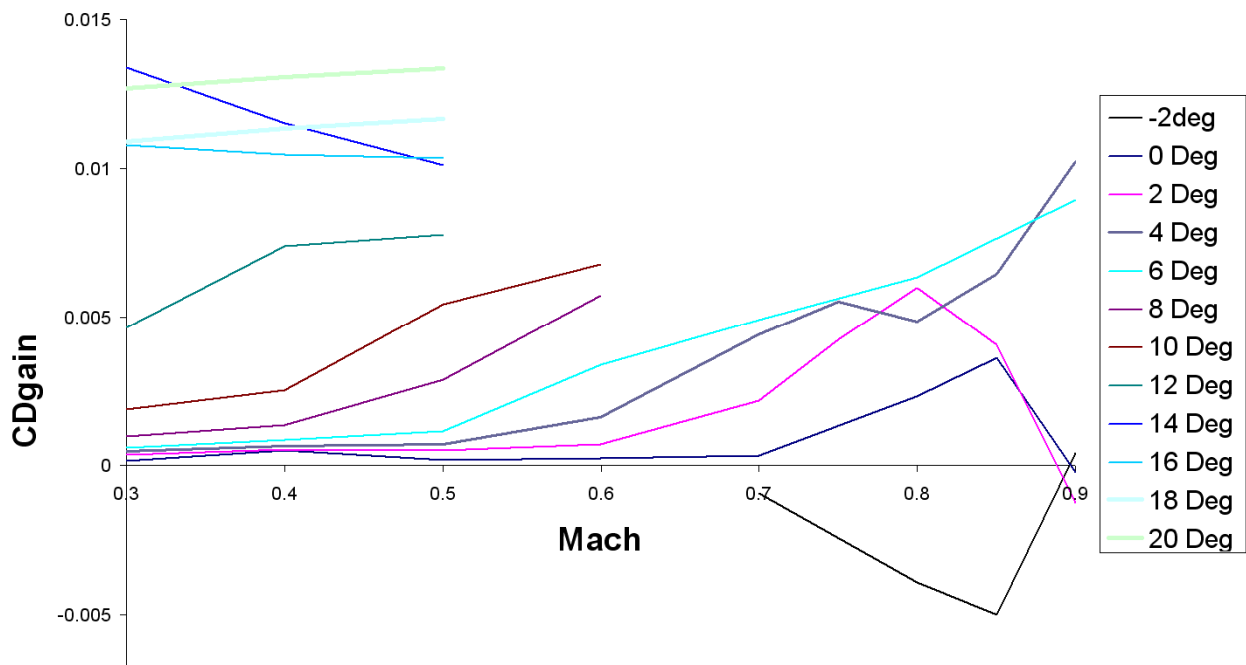
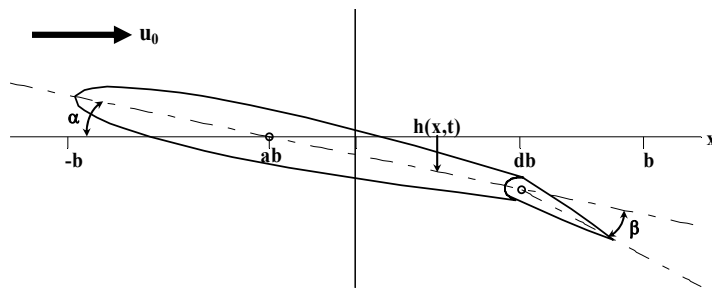


Figure 56. Step C_d Gain per degree of flap deflection for Various Mean Angles and Mean Alpha

As discussed earlier, the indicial response approach was found unsuitable for modeling nonlinear phenomena and was not pursued.

Peter's morphing airfoil approach:

This approach has been coded in a form suitable for incorporation in flight simulation software such as FLIGHTLAB. Experimental data for an oscillating airfoil equipped with an oscillating trailing edge flap was used to validate the approach. Figure 57 shows the configuration considered, while Figures 58 through 60 show representative results in the attached flow, light stall, and deep stall regimes.



Andrzej Krzysiak
 Institute of Aviation
 Warsaw, Poland

Janusz Narkiewicz
 Warsaw Univ. of Tech.
 Warsaw, Poland

- Intended airfoil motion

$$\alpha = \alpha_0 + \bar{\alpha} \sin(k\tau) \quad \beta = \beta_0 + \bar{\beta} \sin(2k\tau - \phi)$$
- Actual airfoil motion had irregularities near extremes

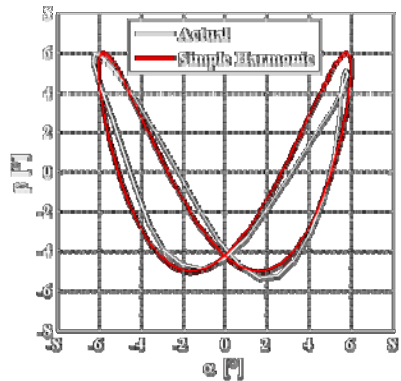


Figure 57. Configuration Used to Validate Prof. Peter's Morphing Airfoil Theory

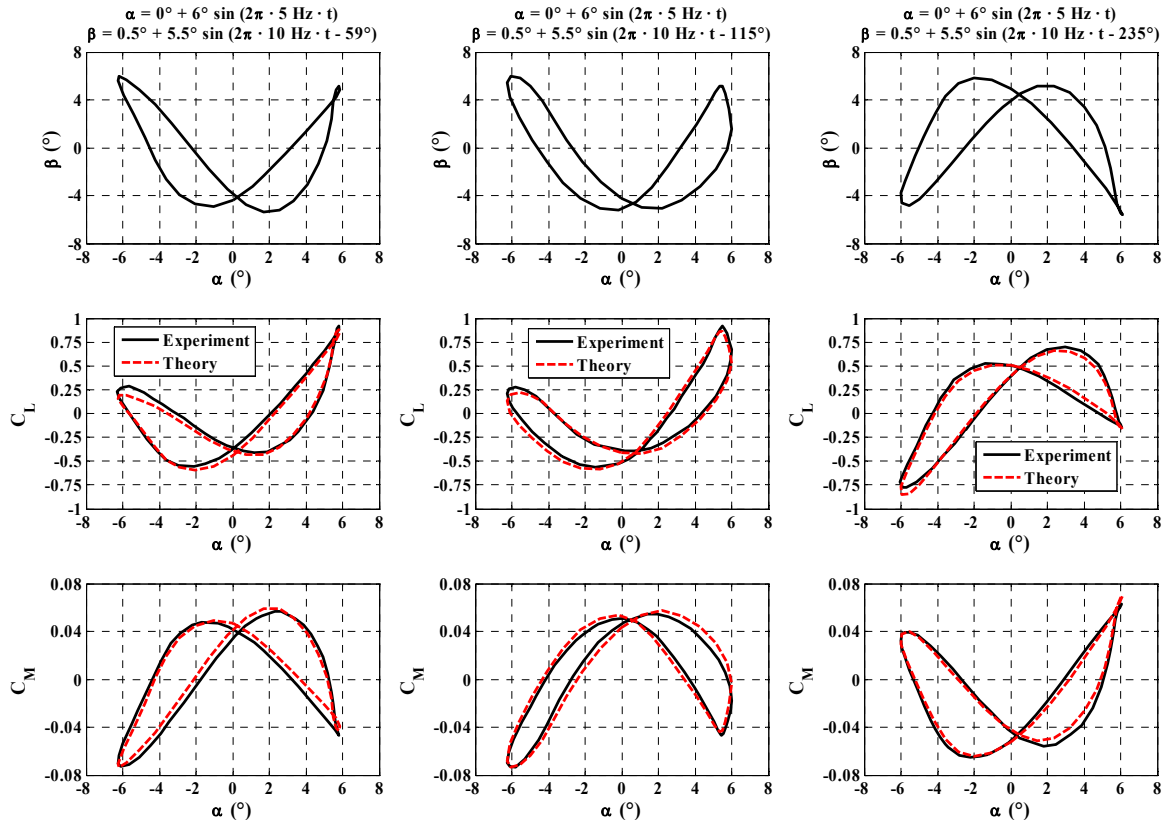


Figure 58. Comparison of test data against Prof. Peter's Morphing Airfoil Theory (Attached Flow)

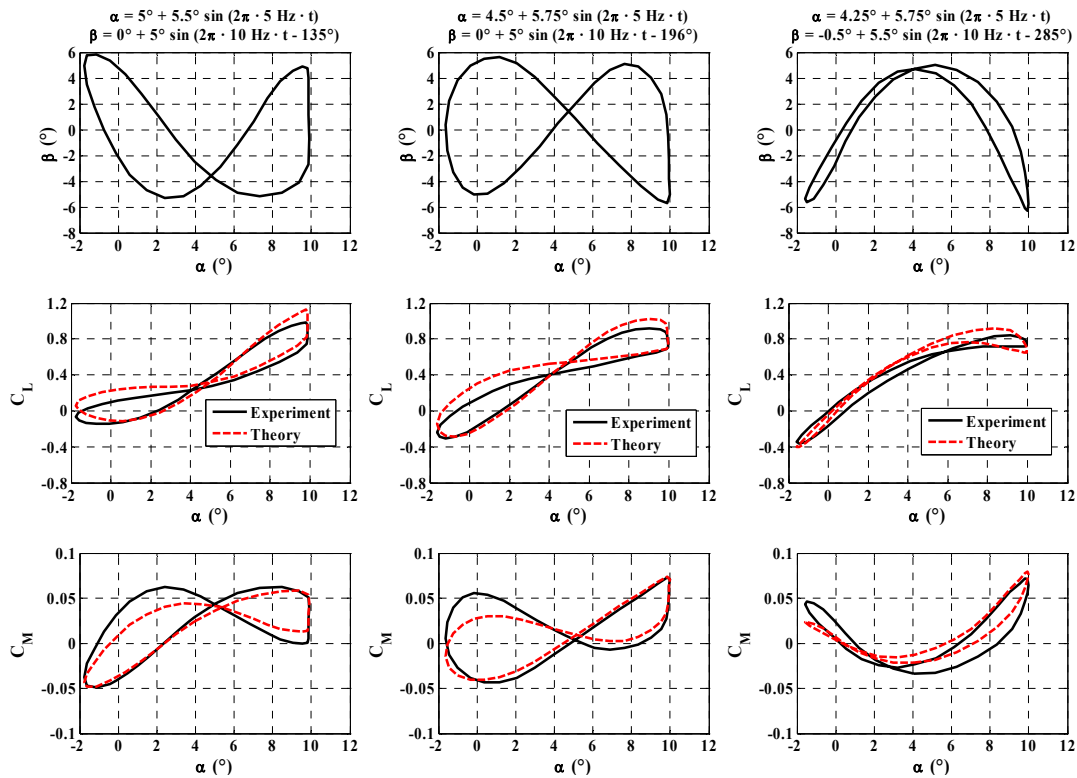


Figure 59. Comparison of test data against Prof. Peter's Morphing Airfoil Theory (Light Stall)

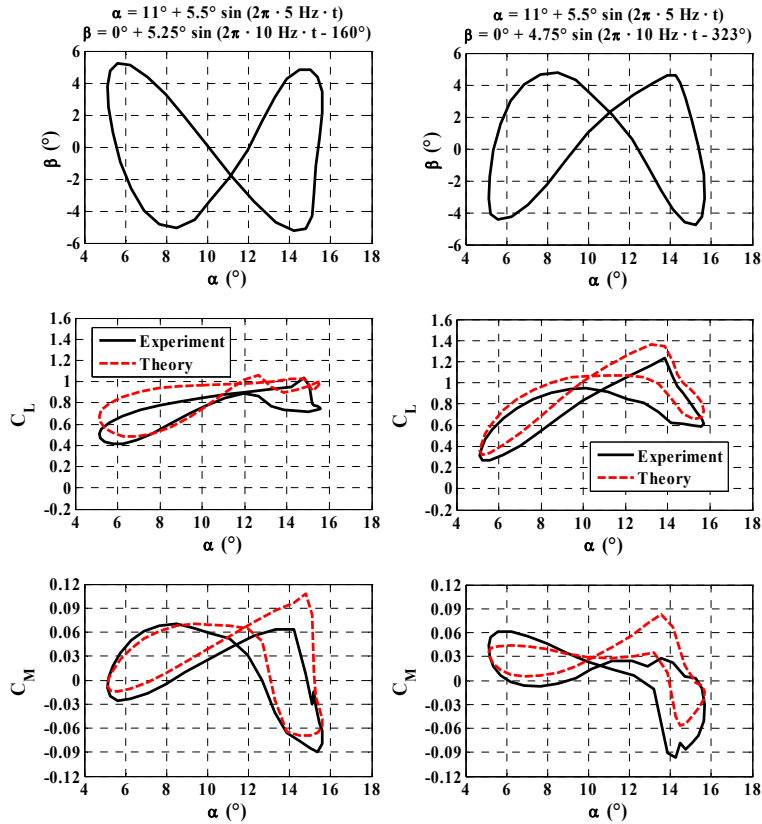


Figure 60. Comparison of test data against Prof. Peter's Morphing Airfoil Theory (Deep Stall)

Neural Network based approach:

The current study considers the development of a NNET based reduced order model for capturing the unsteady aerodynamic effects of a trailing edge flap actuator. The reduced order model is arrived at by first obtaining the changes due to a trailing edge flap deflection on 2D airfoil data through CFD analysis. The compressible Navier-Stokes solver OVERFLOW version 2.0y was used for this study [37]. Those changes are combined with an existing baseline 2D airfoil data without a trailing edge flap. The changes in 2D airfoil data due to the deflection of a trailing edge flap is captured using a pre-trained NNET model from extensive CFD analysis data. Even for a limited range of inputs (see Table 4), a large amount of CPU time is required to produce all the training data required for the NNET model. However, this is needed only once for a given airfoil and TEF configuration.

For the selected distribution of the input parameters of Table 4, CFD runs are designed for an airfoil (SC1095) with an integral quarter chord trailing edge flap (TEF) concept. Both airfoil and TEF angle are defined as sinusoidal functions as

$$\alpha = \alpha_o + \alpha_c \sin(\omega \cdot t)$$

$$\delta = \delta_c \sin(\omega_\delta \cdot t + \psi_\delta)$$

where ω is the oscillation frequency of the airfoil angle of attack, ω_δ is the oscillation frequency of the trailing edge flap deflection and ϕ_δ is the phase angle between angle of attack and TEF angle. The reduced frequency of the airfoil angle of attack and the trailing edge flap deflection are obtained using

$$k_\alpha = \frac{\omega b}{V}$$

$$k_\delta = \frac{\omega_\delta b_\delta}{V} \text{ where } 4b_\delta = b$$

Table 4. Parameters for CFD runs

Mach Number	Airfoil AoA	OBC Angle
M=[0.3 0.4]	$\alpha_o=[15 \ 10 \ 5 \ 0 \ -6]$	$\delta_c=[7 \ 4 \ 0]$
	$\alpha_c=[10 \ 5 \ 2.5]$	$\phi_\delta=[0 \ 90 \ 180]$
	$k=[0 \ 0.03 \ 0.05 \ 0.10]$	$k_\delta=[0.5 \ 1.0]k$
M=[0.5 0.6]	$\alpha_o=[7 \ 3 \ 0 \ -3]$	$\delta_c=[5 \ 3 \ 0]$
	$\alpha_c=[4 \ 2]$	$\phi_\delta=[0 \ 90 \ 180]$
	$k=[0 \ 0.03 \ 0.05 \ 0.10]$	$k_\delta=[0.5 \ 1.0]k$
M=[0.7]	$\alpha_o=[5 \ 2 \ 0 \ -2]$	$\delta_c=[3 \ 1.5 \ 0]$
	$\alpha_c=[2 \ 1]$	$\phi_\delta=[0 \ 90 \ 180]$
	$k=[0 \ 0.03 \ 0.05 \ 0.10]$	$k_\delta=[0.5 \ 1.0]k$

Mach Number	Airfoil AoA	OBC Angle
M=[0.3 0.4]	$\alpha_o=[15 \ 10 \ 5 \ 0 \ -6]$	$\delta_c=[7 \ 4 \ 0]$
	$\alpha_c=[10 \ 5 \ 2.5]$	$\phi_\delta=[0 \ 90 \ 180]$
	$k=[0 \ 0.03 \ 0.05 \ 0.10]$	$k_\delta=[0.5 \ 1.0]k$
M=[0.5 0.6]	$\alpha_o=[7 \ 3 \ 0 \ -3]$	$\delta_c=[5 \ 3 \ 0]$
	$\alpha_c=[4 \ 2]$	$\phi_\delta=[0 \ 90 \ 180]$
	$k=[0 \ 0.03 \ 0.05 \ 0.10]$	$k_\delta=[0.5 \ 1.0]k$
M=[0.7]	$\alpha_o=[5 \ 2 \ 0 \ -2]$	$\delta_c=[3 \ 1.5 \ 0]$

	$\alpha_c=[2 \ 1]$	$\phi_\delta=[0 \ 90 \ 180]$
	$k=[0 \ 0.03 \ 0.05 \ 0.10]$	$k_\delta=[0.5 \ 1.0]k$

The discrete sets of parameter values considered in the CFD analysis are given in Table 4. Each CFD run is conducted with a combination of these input parameters for a complete cycle. The values of the NNET input variables and the computed aerodynamic coefficients from the CFD analysis are extracted at each of the integration steps used.

Baseline aerodynamic coefficient values are subtracted from the CFD data in order to obtain the changes due to the effect of a TEF deflection. Separate databases are recorded for each aerodynamic coefficient since individual training for each set is found to be computationally more efficient as each set may require different settings for the NNET training. Construction of the developed ROM is given in a generic equation form as

$$\begin{aligned}
[c_d \ c_l \ c_m]_{base} &= f_{table}(\alpha, M) \\
[c_d \ c_l \ c_m]_{cfd} &= f_{cfd}(\alpha, \dot{\alpha}, M, \delta, \dot{\delta}) \\
\Delta[c_d \ c_l \ c_m] &= [c_d \ c_l \ c_m]_{cfd} - [c_d \ c_l \ c_m]_{base} \\
\Delta[c_d \ c_l \ c_m] &\cong \Delta[c_d \ c_l \ c_m]_{nnet} \\
&\text{where} \\
\Delta[c_d \ c_l \ c_m]_{nnet} &= f_{nnet}(\alpha, \dot{\alpha}, M, \delta, \dot{\delta}) \\
[c_d \ c_l \ c_m]_{rom} &= f_{nnet} + f_{base}
\end{aligned}$$

The NNET model training is performed with a dedicated module within the FLIGHTLAB [38]. The NNET training makes use of Levenberg-Marquardt algorithm [36, 38] for the training of all three coefficients, i.e., ΔC_l , ΔC_m , and ΔC_d . The selected values of various parameters such as the number of neurons, type of basis function, error tolerance, etc., for the NNET training are shown in Table 5. The number of neurons is selected to be much higher for the drag coefficient as compared to those for the lift and moment coefficients since the drag coefficient data from the CFD analysis shows significantly higher nonlinearity when compared to lift or pitching moment coefficients.

Table 5. Parameters for NNET training.

	ΔC_d	ΔC_l	ΔC_m
Hidden Neurons	34	17	17

Hidden Activation Function	Tangent Hyperbolic	Tangent Hyperbolic	Tangent Hyperbolic
Output Activation Function	Linear $(-\infty, +\infty)$	Linear $(-\infty, +\infty)$	Linear $(-\infty, +\infty)$
Error Tolerance	10^{-6}	10^{-6}	10^{-6}
Maximum number of iterations	10	10	10

In order to make use of the reduced order model component of the trailing edge flap element in the form of the baseline plus the NNET airfoil data, the aerodynamic modules within the FLIGHTLAB are modified to include the effects of trailing edge flaps at user defined locations along a rotor blade. The selected baseline component in FLIGHTLAB makes use of Mach number and angle of attack as inputs. The NNET component makes use of the TEF deflection, TEF deflection rate, local value of the Mach number, angle of attack and its time rate as inputs in order to run the NNET model for evaluating incremental changes of aerodynamic coefficients due to TEF deflections.

The accuracy of the reduced order model was evaluated through comparisons with the CFD results from which the ROM was extracted. Sample results for the case of SC 1095 airfoil with a trailing edge flap are shown in Figures 61 through 67. Figure 61 compares the ROM prediction of the lift coefficient of an SC-1095 airfoil with zero flap deflection in a deep dynamic stall. The ROM result correlates well with the CFD simulation in terms of both trend and magnitude. The ROM prediction also closely follows the trend of the secondary oscillation of C_L during the early stage of the stall recovery as shown in the CFD results, but it is not as oscillatory as the CFD data. This could be improved by refining the NNET neuron structure. However, such a minor discrepancy is not a concern for practical applications. Similarly, good correlation of the pitch moment coefficient prediction by ROM with CFD was also achieved (see Figure 62). Figures 63 and 64 compare ROM results with the CFD data for the case of SC 1095 plus flap combination. After the model was trained using CFD data, it was tested for additional data sets that were not used in the training. In general, very good agreement was found as shown in Figures 63 and 64.

The fidelity of the trained NNET model in capturing the individual components of airloads, i.e., lift, drag and pitching moment, is evaluated after integrating it with the baseline model within FLIGHTLAB. Example cases of CFD runs from Table 4 are used in the NNET fidelity evaluations. Figures 65 through 67 show example comparisons between the CFD results and results from the NNET plus the baseline model. These results indicate that the lift and moment coefficient comparisons show very good correlation, while the drag coefficient comparisons show similar trends with a larger relative error.

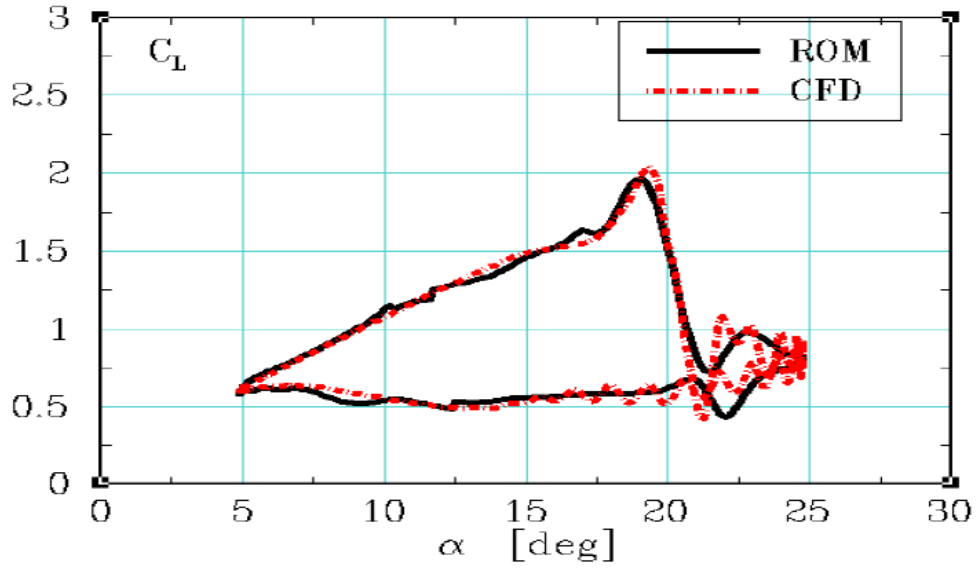


Figure 61. Computed and Predicted Lift Hysteresis Loops for a SC 1095 Airfoil in Deep Stall

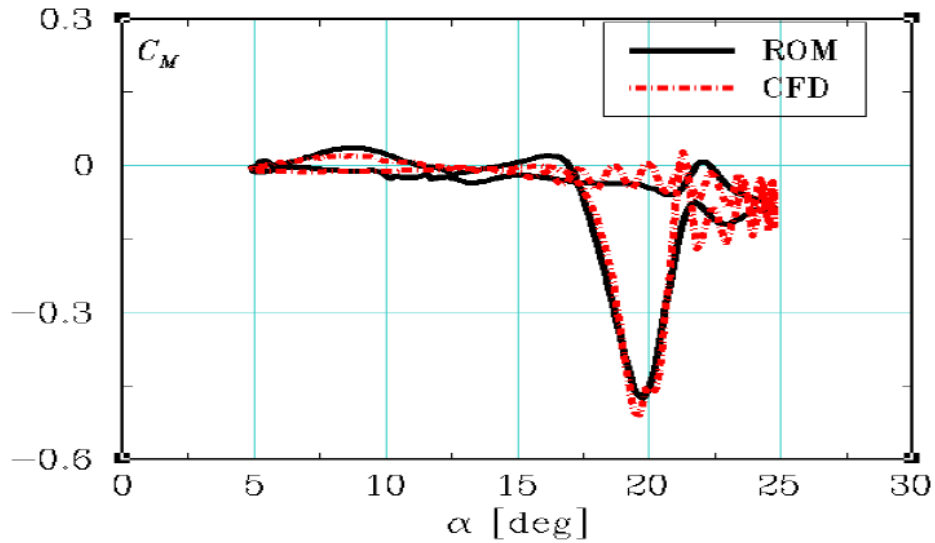


Figure 62. Computed and Predicted Moment Hysteresis Loops for a SC 1095 Airfoil in Deep Stall

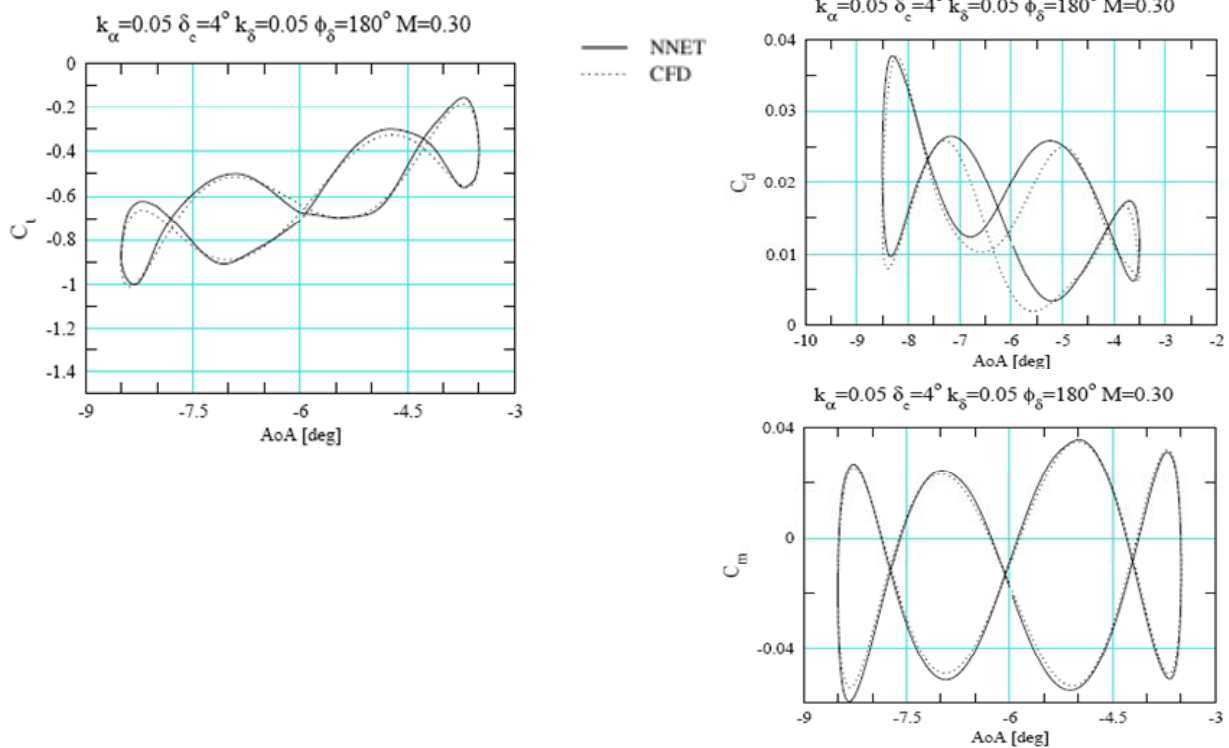


Figure 63. Computed and Predicted Moment Hysteresis Loops for a SC 1095 Airfoil +Flap Combination

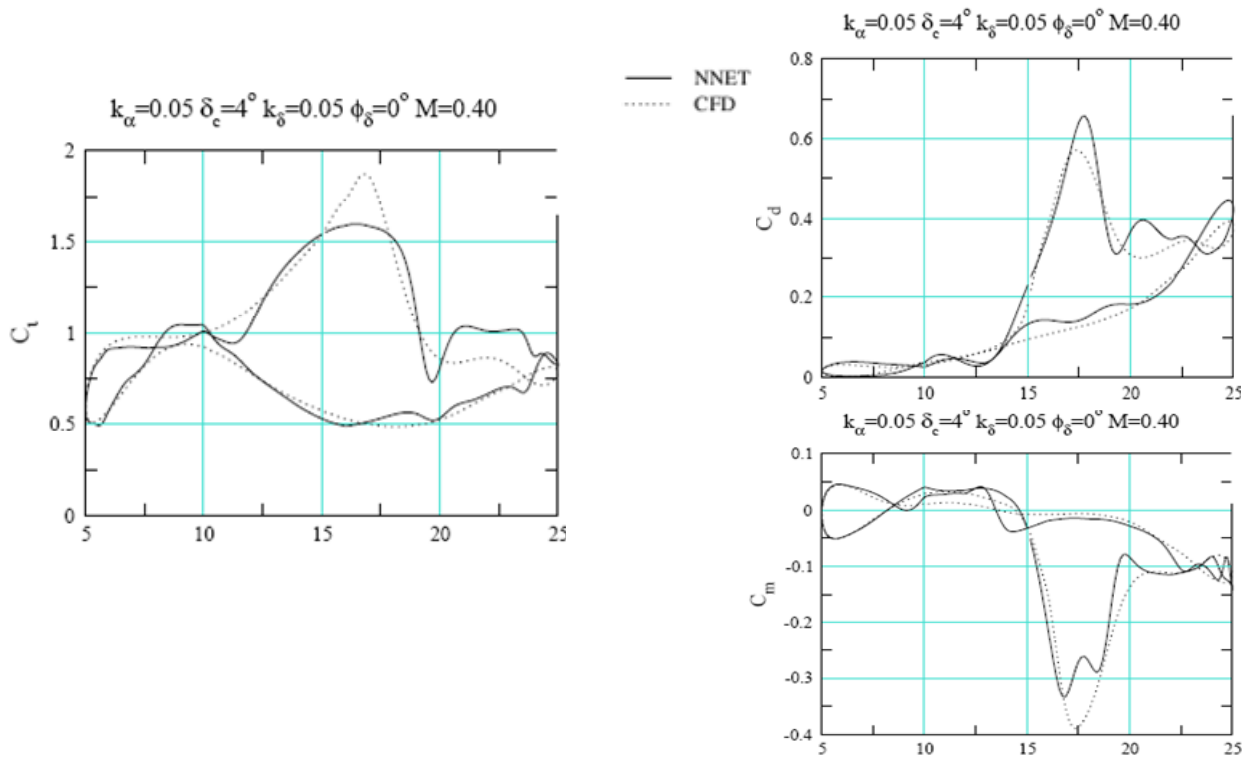


Figure 64. Computed and Predicted Moment Hysteresis Loops for a SC 1095 Airfoil +Flap Combination

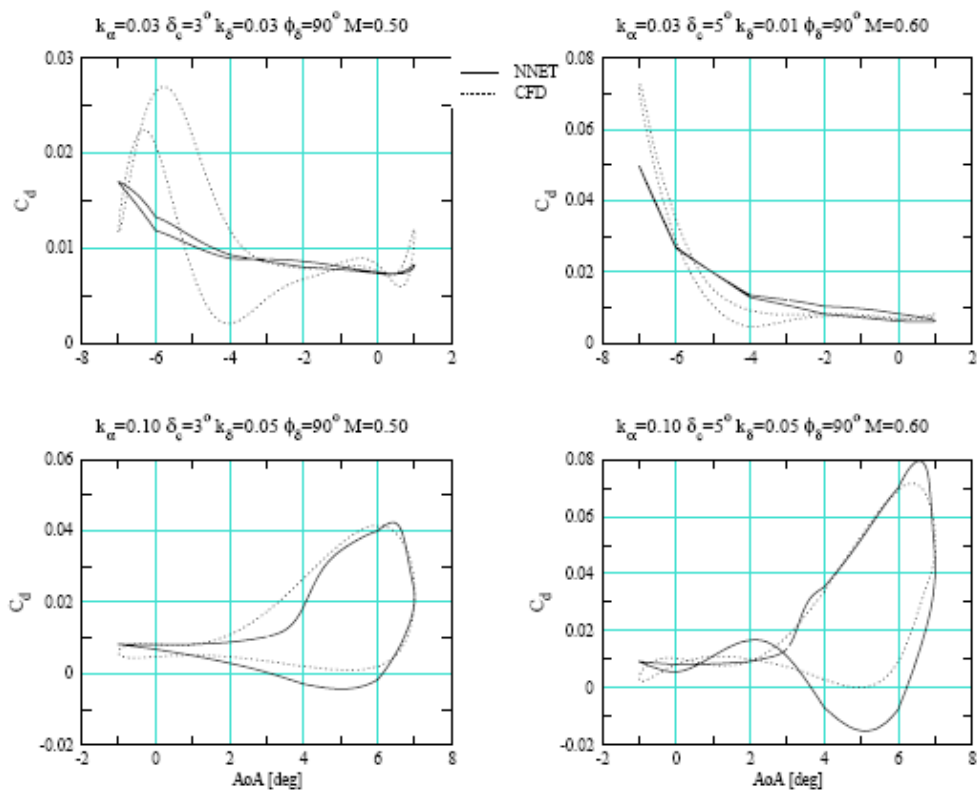


Figure 65. Drag Coefficient NNET Estimations Compared to CFD Data

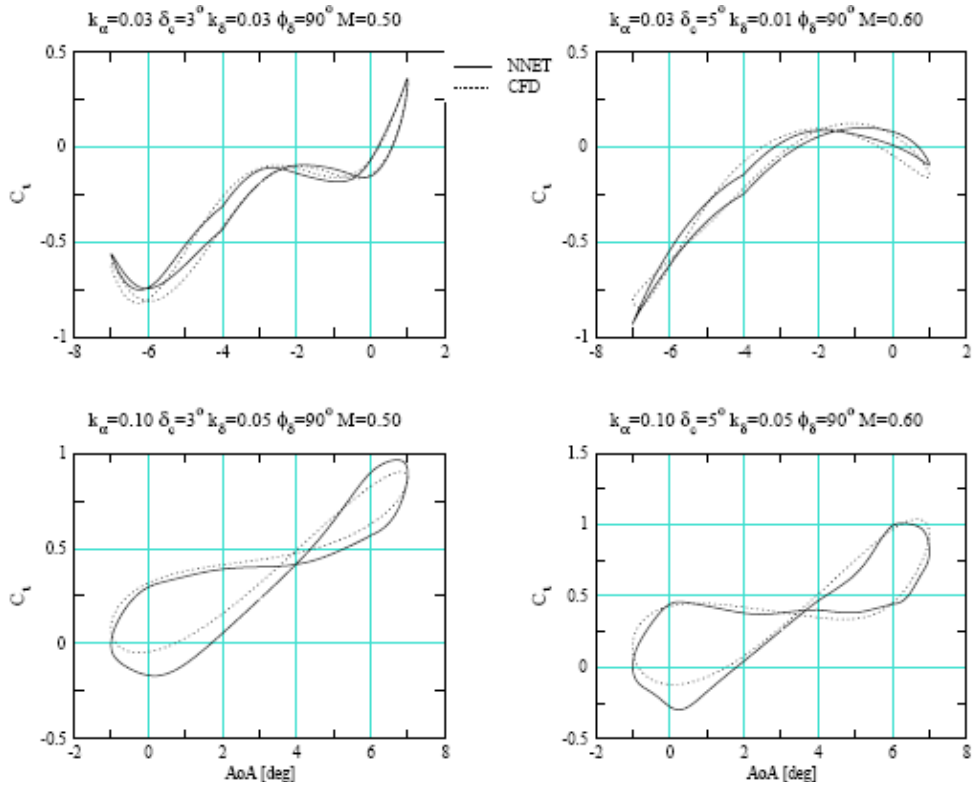


Figure 66. Lift Coefficient NNET Estimations Compared to CFD Data

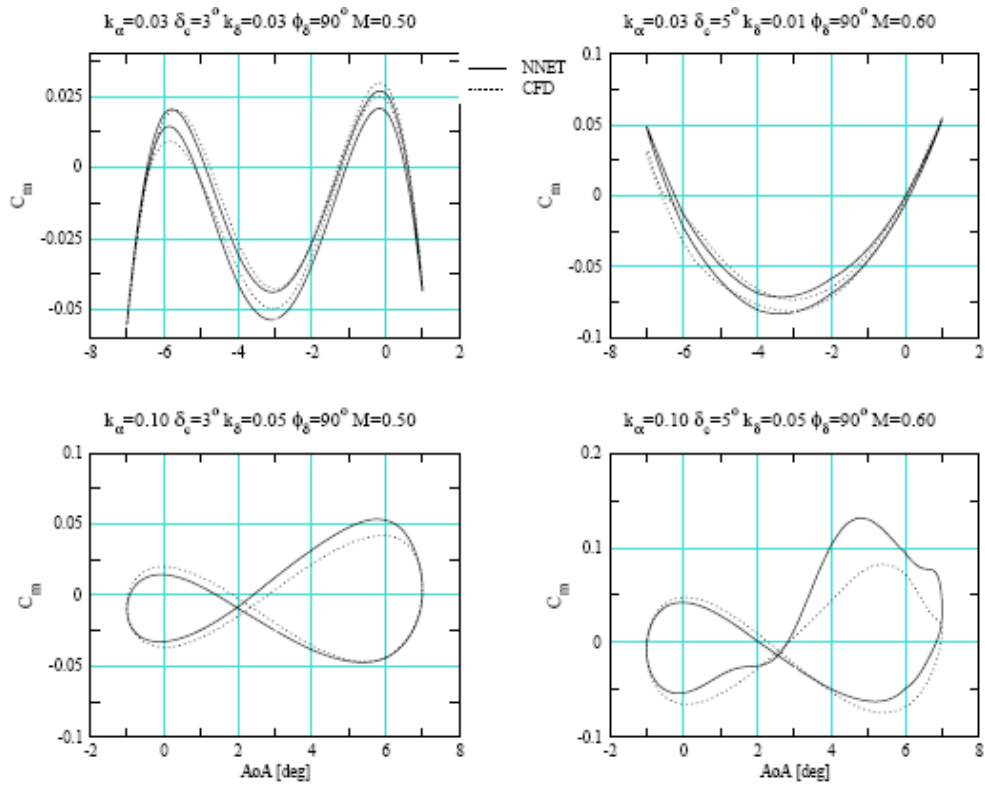


Figure 67. Moment Coefficient NNET Estimations Compared to CFD Data

Selected Approach for Reduced Order Modeling of OBC

Three approaches were considered for reduced order modeling of OBC. Among these three, the neural network based model was found to be most robust and accurate for a range of flow conditions, mean angles of attack, and actuation amplitudes. Training may be done offline. The resulting neural network models may be readily incorporated in flight simulation software.

TASK 3: INTEGRATION OF OBC REDUCED ORDER MODELS AND EVALUATIONS

The objectives of this task are to integrate the reduced order models developed in the previous section into a comprehensive flight simulation model and to evaluate the functionality of the integrated model through simulations.

In order to make use of the reduced order model component of the trailing edge flap element in the form of the baseline plus the NNET airfoil data, the aerodynamic modules within the FLIGHTLAB are modified to include the effects of trailing edge flaps at user defined locations along a rotor blade. The selected baseline component in FLIGHTLAB makes use of Mach number and angle of attack as inputs. The NNET component makes use of the TEF deflection, TEF deflection rate, local value of the Mach number, angle of attack and its time rate as inputs in order to run the NNET model for evaluating incremental changes of aerodynamic coefficients due to TEF deflections.

The reduced order models of a trailing edge flap developed in the previous section was applied to a testing rotor for evaluation of advanced on-blade control concepts. For illustration, an example on-blade control using active trailing edge flap was evaluated. Figure 68 illustrates the testing example where the trailing edge flap was applied over a blade section from 0.55 to 0.91 of the rotor radius for a generic 4-bladed articulated rotor. The effect of OBC in terms of active trailing edge flap was evaluated. For this, an example profile of the trailing edge flap was applied

$$\delta = 2 \sin(2\psi - 30^\circ)$$

Figure 69 shows the variation of the longitudinal rotor hub force under the excitation of the 2/rev active trailing flap. Compared to the baseline without the active flap excitation, the effect of the on-blade control is apparent in the ROM simulation. Figures 70 and 71 show the variation of the lateral and normal rotor hub force components, respectively. A similar effect from OBC as presented in the ROM can be observed. The application of the active trailing edge flap with the above selected second harmonic profile significantly reduces the oscillatory component of the hub shear force. Notice that the prescribed second harmonic active flap control is an estimated control for functional testing only, instead of an optimized one for overall rotor hub vibratory load reduction. In fact, this profile caused some increase in the hub moment components although it did reduce all the vibratory shear components.

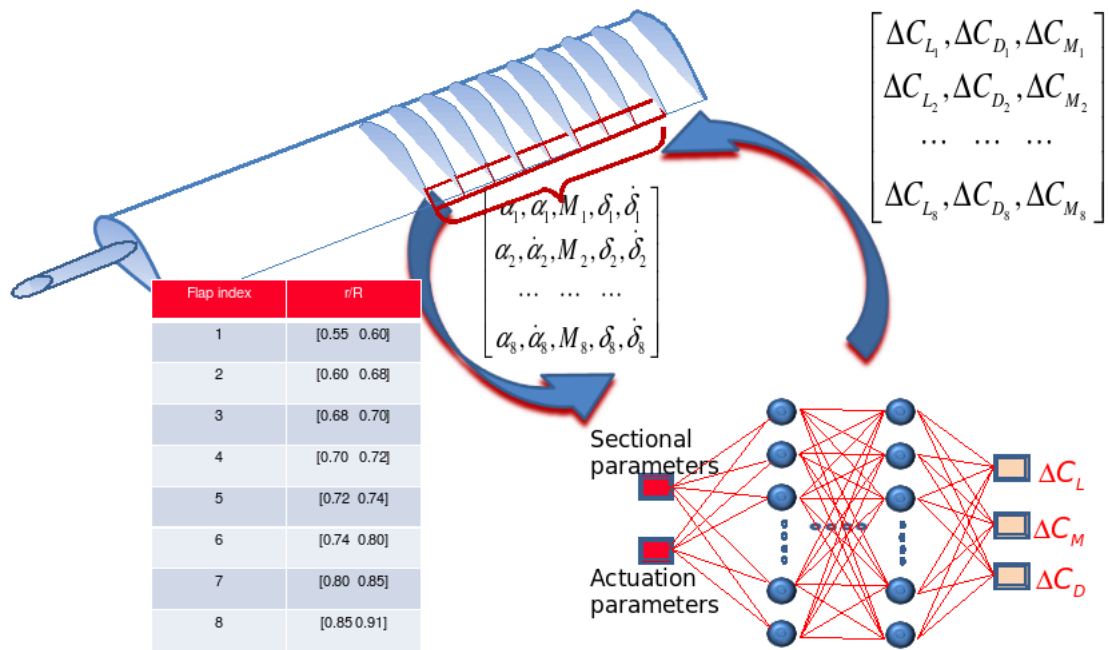


Figure 68. Implementation of ROM for active trailing flap control studies

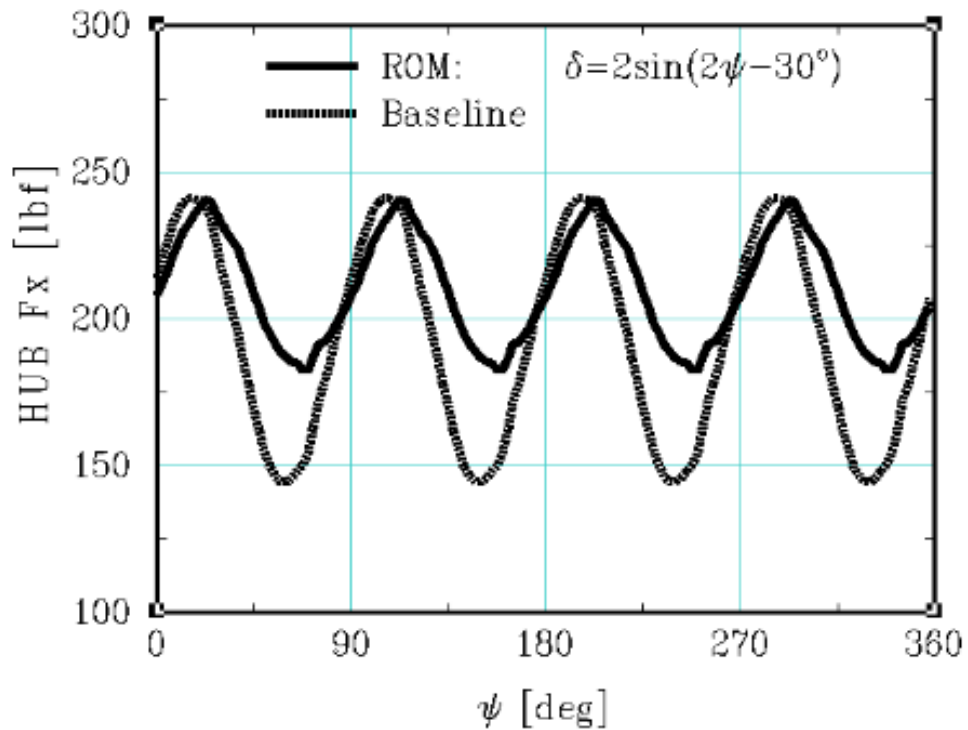


Figure 69. Effect of active trailing flap on rotor hub force (F_x)

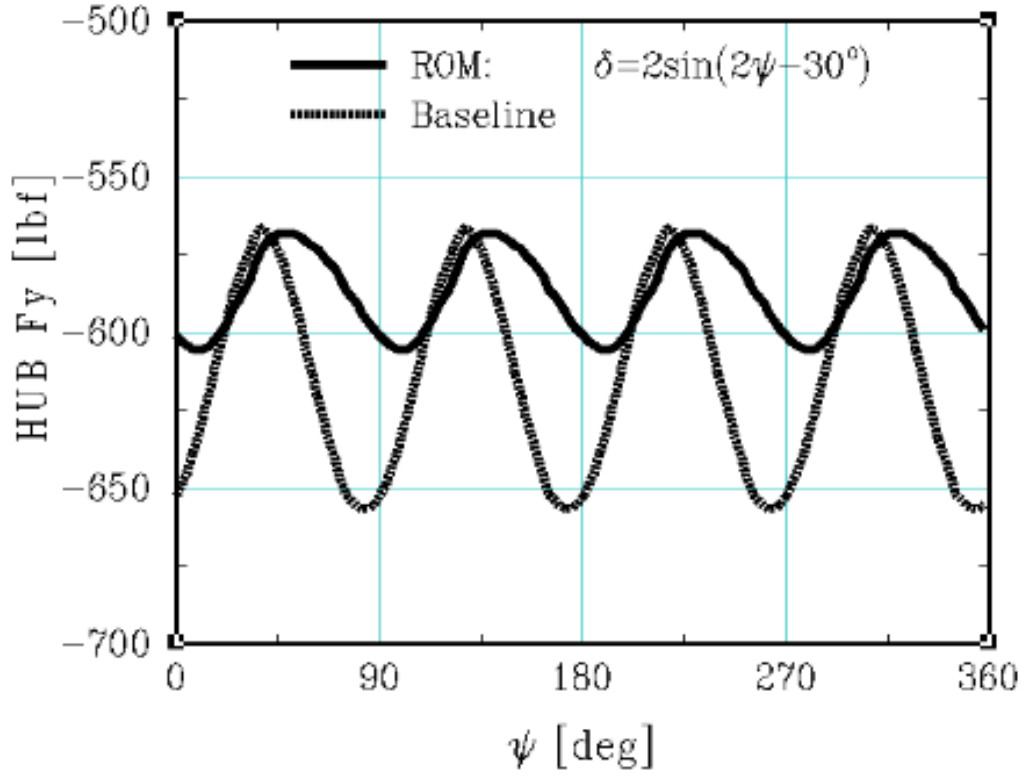


Figure 70. Effect of active trailing flap on rotor hub force (F_y)

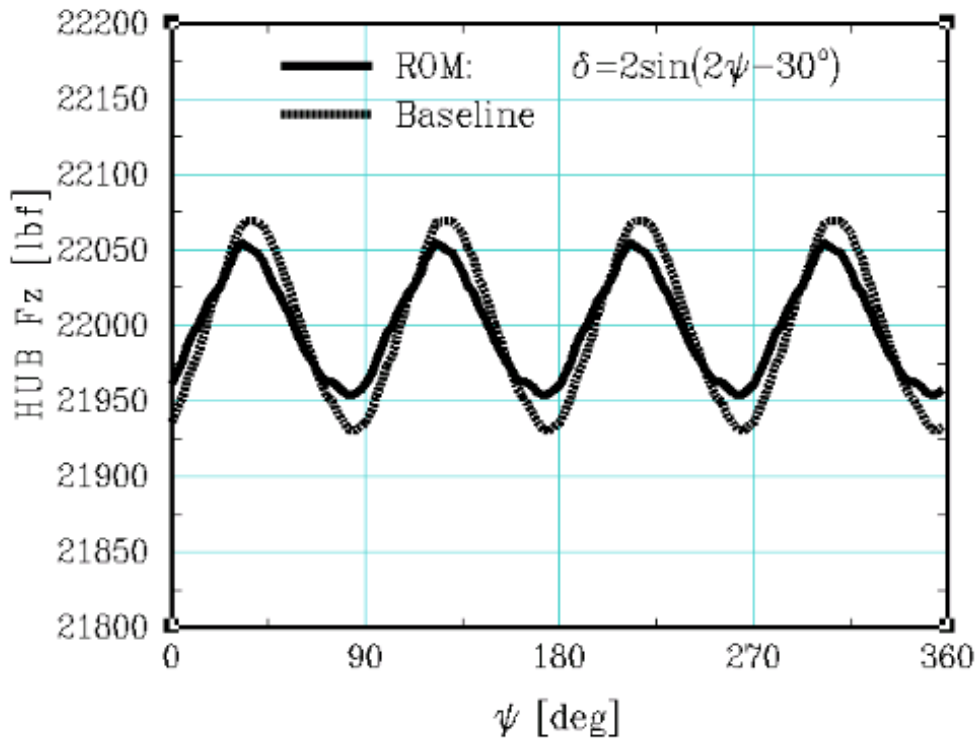


Figure 71. Effect of active trailing flap on rotor hub force (F_z)

TASK 4: DEVELOPMENT OF EFFICIENT ALGORITHMS FOR EXTRACTION OF LINEAR TIME INVARIANT MODELS

The objectives of this task are to develop a methodology and efficient algorithms for extraction of linear time invariant (LTI) models from a nonlinear model that include important coupling effects between body and rotor degrees of freedom.

This section first provides a mathematical formulation for obtaining linearized models in time invariant form about a periodic equilibrium of a nonlinear system. Next, details on implementation of the developed methodology in the form of computational algorithms within a comprehensive flight simulation model are provided.

LTI Model Formulation from a Nonlinear Model

Consider a nonlinear system of the form

$$f(X, \dot{X}, \ddot{X}, U) = 0 \quad (1)$$

where X , \dot{X} and \ddot{X} are respectively the position, velocity and acceleration vectors, and U is the control vector. Let $((\bar{X}(\psi), \bar{U}(\psi)))$ represents a periodic equilibrium of the system of Eq. (1) such that

$$\bar{X}(\psi + 2\pi) = \bar{X}(\psi), \quad \bar{U}(\psi + 2\pi) = \bar{U}(\psi) \quad (2)$$

A linearization of Eq. (1) can be obtained by considering changes from equilibrium as

$$x(\psi) = X(\psi) - \bar{X}(\psi), \quad u(\psi) = U(\psi) - \bar{U}(\psi) \quad (3)$$

and expanding Eq. (1) about the periodic equilibrium in Taylor series to first order as

$$f(\bar{X}, \dot{\bar{X}}, \ddot{\bar{X}}, \bar{U}) + \left[\frac{\partial f}{\partial \ddot{X}} \right] \ddot{x} + \left[\frac{\partial f}{\partial \dot{X}} \right] \dot{x} + \left[\frac{\partial f}{\partial X} \right] x + \left[\frac{\partial f}{\partial U} \right] u = 0 \quad (4)$$

The partial derivatives in Eq. (4) are obtained at the selected periodic equilibrium. Since the periodic equilibrium also must satisfy Eq. (1), the above equation reduces to

$$\left[\frac{\partial f}{\partial \ddot{X}} \right] \ddot{x} + \left[\frac{\partial f}{\partial \dot{X}} \right] \dot{x} + \left[\frac{\partial f}{\partial X} \right] x + \left[\frac{\partial f}{\partial U} \right] u = 0 \quad (5)$$

which can be rearranged into the form

$$\ddot{x} = -K(\psi)x - D(\psi)\dot{x} + G(\psi)u \quad (6)$$

where

$$\begin{aligned}
K(\psi) &= \left[\frac{\partial f}{\partial \ddot{X}} \right]^{-1} \left[\frac{\partial f}{\partial X} \right] \\
D(\psi) &= \left[\frac{\partial f}{\partial \ddot{X}} \right]^{-1} \left[\frac{\partial f}{\partial \dot{X}} \right] \\
G(\psi) &= - \left[\frac{\partial f}{\partial \ddot{X}} \right]^{-1} \left[\frac{\partial f}{\partial U} \right]
\end{aligned} \tag{7}$$

Likewise, defining the output equation of the nonlinear system of Eq. (1) as

$$Y = g(X, \dot{X}, \ddot{X}, U) \tag{8}$$

where Y is a vector of outputs. At a periodic equilibrium, the value of the out vector is

$$\bar{Y} = g(\bar{X}, \dot{\bar{X}}, \ddot{\bar{X}}, \bar{U}) \tag{9}$$

A linearized form of the output equation is obtained by expanding Eq. (8) about the periodic equilibrium in Taylor series to first order as

$$Y = g(\bar{X}, \dot{\bar{X}}, \ddot{\bar{X}}, \bar{U}) + \left[\frac{\partial g}{\partial \ddot{X}} \right] \ddot{x} + \left[\frac{\partial g}{\partial \dot{X}} \right] \dot{x} + \left[\frac{\partial g}{\partial X} \right] x + \left[\frac{\partial g}{\partial U} \right] u \tag{10}$$

Substituting Eqs. (6) and (9) into Eq. (10) results in

$$y = P(\psi)x + Q(\psi)\dot{x} + R(\psi)u \tag{11}$$

where y represents change in the output Y from its equilibrium value \bar{Y} , and P, Q and R matrices can be obtained using

$$\begin{aligned}
P(\psi) &= \left[\frac{\partial g}{\partial X} \right] - \left[\frac{\partial g}{\partial \ddot{X}} \right] K(\psi) \\
Q(\psi) &= \left[\frac{\partial g}{\partial \dot{X}} \right] - \left[\frac{\partial g}{\partial \ddot{X}} \right] D(\psi) \\
R(\psi) &= \left[\frac{\partial g}{\partial U} \right] + \left[\frac{\partial g}{\partial \ddot{X}} \right] G(\psi)
\end{aligned} \tag{12}$$

The linear time periodic (LTP) model of Eqs. (6) and (11) is converted into a linear time invariant (LTI) form using the following approximation to x:

$$x = x_o + \sum_{n=1}^N x_{nc} \cos n\psi + x_{ns} \sin n\psi \quad (13)$$

where x_o is the average component and x_{nc} and x_{ns} are respectively the n /rev cosine and sine harmonic components of x . Likewise, control (u) and output (y) are expanded in terms of harmonic components as

$$u = u_o + \sum_{m=1}^M u_{mc} \cos m\psi + u_{ms} \sin m\psi \quad (14)$$

$$y = y_o + \sum_{l=1}^L y_{lc} \cos l\psi + y_{ls} \sin l\psi \quad (15)$$

Now defining an augmented state, control and output vectors in terms of their respective average and harmonic components as

$$\begin{aligned} x_{aug} &= \left[x_o^T \dots x_{ic}^T \quad x_{is}^T \dots x_{jc}^T \quad x_{js}^T \dots \dot{x}_o^T \dots \dot{x}_{ic}^T \quad \dot{x}_{is}^T \dots \dot{x}_{jc}^T \quad \dot{x}_{js}^T \dots \right]^T \\ u_{aug} &= \left[u_o^T \dots u_{mc}^T \quad u_{ms}^T \dots \right]^T \\ y_{aug} &= \left[y_o^T \dots y_{lc}^T \quad y_{ls}^T \dots \right]^T \end{aligned}$$

where x_o is the average component, x_{ic} and x_{is} are respectively the i^{th} harmonic cosine and sine components of x , u_o is the average component and u_{mc} and u_{ms} are respectively the m^{th} harmonic cosine and sine components of u , and y_o is the average component and y_{lc} and y_{ls} are respectively the l^{th} harmonic cosine and sine components of y . Using the augmented state, control and output vectors, the LTP model of Eqs. (6) and (11) can be approximated into a LTI form as

$$\dot{x}_{aug} = \begin{bmatrix} A_{11} & A_{12} \\ A_{21} & A_{22} \end{bmatrix} x_{aug} + \begin{bmatrix} B_1 \\ B_2 \end{bmatrix} u_{aug} \quad (16)$$

$$y_{aug} = \begin{bmatrix} C_1 \\ C_2 \end{bmatrix} x_{aug} + [E] u_{aug} \quad (17)$$

where

$$A_{11} = \begin{bmatrix} 0 & \dots & 0 & 0 & \dots & 0 & 0 & \dots \\ \dots & \dots \\ 0 & \dots & 0 & 0 & \dots & 0 & 0 & \dots \\ 0 & \dots & 0 & 0 & \dots & 0 & 0 & \dots \\ \dots & \dots \\ 0 & \dots & 0 & 0 & \dots & 0 & 0 & \dots \\ 0 & \dots & 0 & 0 & \dots & 0 & 0 & \dots \\ \dots & \dots \end{bmatrix} \quad (18)$$

$$A_{12} = \begin{bmatrix} I & \dots & 0 & 0 & \dots & 0 & 0 & \dots \\ \dots & \dots \\ 0 & \dots & I & 0 & \dots & 0 & 0 & \dots \\ 0 & \dots & 0 & I & \dots & 0 & 0 & \dots \\ \dots & \dots \\ 0 & \dots & 0 & 0 & \dots & I & 0 & \dots \\ 0 & \dots & 0 & 0 & \dots & 0 & I & \dots \\ \dots & \dots \end{bmatrix} \quad (19)$$

$$A_{21} = \begin{bmatrix} -H_{oK} \dots (-H_{oKic} + i\Omega H_{oDis}) & (-H_{oKis} - i\Omega H_{oDic}) \dots (-H_{oKjc} + j\Omega H_{oDjs}) & (-H_{oKjs} - j\Omega H_{oDjc}) \dots & \dots \\ \dots & \dots & \dots & \dots \\ -H_{icK} \dots (i^2\Omega^2 I - H_{icKic} + i\Omega H_{icDis}) & (-H_{icKis} - i\Omega H_{icDic}) \dots (-H_{icKjc} + j\Omega H_{icDjs}) & (-H_{icKjs} - j\Omega H_{icDjc}) \dots & \dots \\ -H_{isK} \dots (-H_{isKic} + i\Omega H_{isDis}) & (i^2\Omega^2 I - H_{isKis} - i\Omega H_{isDic}) \dots (-H_{isKjc} + j\Omega H_{isDjs}) & (-H_{isKjs} - j\Omega H_{isDjc}) \dots & \dots \\ \dots & \dots & \dots & \dots \\ -H_{jcK} \dots (-H_{jcKic} + i\Omega H_{jcDis}) & (-H_{jcKis} - i\Omega H_{jcDic}) \dots (j^2\Omega^2 I - H_{jcKjc} + j\Omega H_{jcDjs}) & (-H_{jcKjs} - j\Omega H_{jcDjc}) \dots & \dots \\ -H_{jsK} \dots (-H_{jsKic} + i\Omega H_{jsDis}) & (-H_{jsKis} - i\Omega H_{jsDic}) \dots (-H_{jsKjc} + j\Omega H_{jsDjs}) & (j^2\Omega^2 I - H_{jsKjs} - j\Omega H_{jsDjc}) \dots & \dots \\ \dots & \dots & \dots & \dots \end{bmatrix} \quad (20)$$

$$A_{22} = \begin{bmatrix} -H_{oD} \dots - H_{oDic} & -H_{oDis} \dots - H_{oDjc} & -H_{oDjs} \dots & \dots \\ \dots & \dots & \dots & \dots \\ -H_{icD} \dots - H_{icDic} & (-2i\Omega I - H_{icDis}) \dots - H_{icDjc} & -H_{icDjs} \dots & \dots \\ -H_{isD} \dots (2i\Omega I - H_{isDic}) & -H_{isDis} \dots - H_{isDjc} & -H_{isDjs} \dots & \dots \\ \dots & \dots & \dots & \dots \\ -H_{jcD} \dots - H_{jcDic} & -H_{jcDis} \dots - H_{jcDjc} & (-2j\Omega I - H_{jcDjs}) \dots & \dots \\ -H_{jsD} \dots - H_{jsDic} & -H_{jsDis} \dots (2j\Omega I - H_{jsDjc}) & -H_{jsDjs} \dots & \dots \\ \dots & \dots & \dots & \dots \end{bmatrix} \quad (21)$$

$$B_1 = \begin{bmatrix} 0 \\ \cdot \\ 0 \\ 0 \\ \cdot \\ 0 \\ 0 \\ \cdot \end{bmatrix} \quad (22)$$

$$B_2 = \begin{bmatrix} H_{oG} \dots H_{oG^{mc}} & H_{oG^{ms}} \dots \\ \dots \\ H_{icG} \dots H_{icG^{mc}} & H_{icG^{ms}} \dots \\ H_{isG} \dots H_{isG^{mc}} & H_{isG^{ms}} \dots \\ \dots \\ H_{jcG} \dots H_{jcG^{mc}} & H_{jcG^{ms}} \dots \\ H_{jsG} \dots H_{jsG^{mc}} & H_{jsG^{ms}} \dots \\ \dots \end{bmatrix} \quad (23)$$

$$C_1 = \begin{bmatrix} H_{oP} \dots (H_{oP^{ic}} - i\Omega H_{oQ^{is}}) & (H_{oP^{is}} + i\Omega H_{oQ^{ic}}) \dots (H_{oP^{jc}} - j\Omega H_{oQ^{js}}) & (H_{oP^{js}} + j\Omega H_{oQ^{ic}}) \dots \\ \dots \\ H_{lcP} \dots (H_{lcP^{ic}} - i\Omega H_{lcQ^{is}}) & (H_{lcP^{is}} + i\Omega H_{lcQ^{ic}}) \dots (H_{lcP^{jc}} - j\Omega H_{lcQ^{js}}) & (H_{lcP^{js}} + j\Omega H_{lcQ^{ic}}) \dots \\ H_{lsP} \dots (H_{lsP^{ic}} - i\Omega H_{lsQ^{is}}) & (H_{lsP^{is}} + i\Omega H_{lsQ^{ic}}) \dots (H_{lsP^{jc}} - j\Omega H_{lsQ^{js}}) & (H_{lsP^{js}} + j\Omega H_{lsQ^{ic}}) \dots \\ \dots \end{bmatrix} \quad (24)$$

$$C_2 = \begin{bmatrix} \cdot H_{oQ} \dots H_{oQ^{ic}} & H_{oQ^{is}} \dots H_{oQ^{jc}} & H_{oQ^{js}} \dots \\ \dots \\ \cdot H_{lcQ} \dots H_{lcQ^{ic}} & H_{lcQ^{is}} \dots H_{lcQ^{jc}} & H_{lcQ^{js}} \dots \\ H_{lsQ} \dots H_{lsQ^{ic}} & H_{lsQ^{is}} \dots H_{lsQ^{jc}} & H_{lsQ^{js}} \dots \\ \dots \end{bmatrix} \quad (25)$$

$$E = \begin{bmatrix} H_{oR} \dots H_{oR^{mc}} & H_{oR^{ms}} \dots \\ \dots \\ H_{lcR} \dots H_{lcR^{mc}} & H_{lcR^{ms}} \dots \\ H_{lsR} \dots H_{lsR^{mc}} & H_{lsR^{ms}} \dots \\ \dots \end{bmatrix} \quad (26)$$

Closed form expressions for the various elements of A_{12} , A_{22} , B_2 , C_1 , C_2 and E can be obtained in terms of harmonic components of the LTP model matrices D , K , G , P , Q and R . For example, if the matrix $D(\psi)$ is expanded in terms of its harmonic components as

$$D(\psi) = D_o + \sum_{k=1}^{\infty} (D_{kc} \cos k\psi + D_{ks} \sin k\psi) \quad (27)$$

where D_o is the average component and D_{kc} and D_{ks} are respectively the k^{th} harmonic cosine and sine components of the matrix $D(\psi)$ such that

$$D_o = \frac{1}{2\pi} \int_0^{2\pi} D(\psi) d\psi$$

$$D_{kc} = \frac{1}{\pi} \int_0^{2\pi} D(\psi) \cos k\psi d\psi \quad (28)$$

$$D_{ks} = \frac{1}{\pi} \int_0^{2\pi} D(\psi) \sin k\psi d\psi$$

$$k = 1, 2, 3, \dots$$

then

$$\begin{aligned}
H_{oD} &= \frac{1}{2\pi} \int_0^{2\pi} D(\psi) d\psi = D_o \\
H_{oD^{ic}} &= \frac{1}{2\pi} \int_0^{2\pi} D(\psi) \cos i\psi d\psi = \frac{D_{ic}}{2} \\
H_{oD^{is}} &= \frac{1}{2\pi} \int_0^{2\pi} D(\psi) \sin i\psi d\psi = \frac{D_{is}}{2} \\
& i = 1, 2, 3, \dots
\end{aligned} \tag{29}$$

$$\begin{aligned}
H_{icD} &= \frac{1}{\pi} \int_0^{2\pi} D(\psi) \cos i\psi d\psi = D_{ic} \\
H_{isD} &= \frac{1}{\pi} \int_0^{2\pi} D(\psi) \sin i\psi d\psi = D_{is} \\
& i = 1, 2, 3, \dots
\end{aligned} \tag{30}$$

$$\begin{aligned}
H_{icD^{jc}} &= \frac{1}{\pi} \int_0^{2\pi} D(\psi) \cos j\psi \cos i\psi d\psi \\
&= D_o + \frac{D_{kc}}{2} \text{ for } i = j \text{ where } k = i + j \\
&= \frac{D_{kc} + D_{lc}}{2} \text{ for } i \neq j \text{ and } i > j \\
& \text{ where } k = i + j, \quad l = i - j \\
&= \frac{D_{kc} + D_{mc}}{2} \text{ for } i \neq j \text{ and } j > i \\
& \text{ where } k = i + j, \quad m = j - i \\
& i = 1, 2, \dots \text{ and } j = 1, 2, \dots
\end{aligned} \tag{31}$$

$$\begin{aligned}
H_{icD^{js}} &= \frac{1}{\pi} \int_0^{2\pi} D(\psi) \sin j\psi \cos i\psi d\psi \\
&= \frac{D_{ks}}{2} \text{ for } i = j \text{ where } k = i + j \\
&= \frac{D_{ks} - D_{ls}}{2} \text{ for } i \neq j \text{ and } i > j \\
& \text{ where } k = i + j, \quad l = i - j \\
&= \frac{D_{ks} + D_{ms}}{2} \text{ for } i \neq j \text{ and } j > i \\
& \text{ where } k = i + j, \quad m = j - i \\
& i = 1, 2, \dots \text{ and } j = 1, 2, \dots
\end{aligned} \tag{32}$$

$$\begin{aligned}
H_{isD^{jc}} &= \frac{1}{\pi} \int_0^{2\pi} D(\psi) \cos j\psi \sin i\psi d\psi \\
&= \frac{D_{ks}}{2} \text{ for } i=j \text{ where } k=i+j \\
&= \frac{D_{ks}+D_{ls}}{2} \text{ for } i \neq j \text{ and } i>j \\
&\quad \text{where } k=i+j, \quad l=i-j \\
&= \frac{D_{ks}-D_{ms}}{2} \text{ for } i \neq j \text{ and } j>i \\
&\quad \text{where } k=i+j, \quad m=j-i \\
&\quad i=1,2,\dots \text{ and } j=1,2,\dots
\end{aligned} \tag{33}$$

$$\begin{aligned}
H_{isD^{js}} &= \frac{1}{\pi} \int_0^{2\pi} D(\psi) \sin j\psi \sin i\psi d\psi \\
&= D_o - \frac{D_{kc}}{2} \text{ for } i=j \text{ where } k=i+j \\
&= \frac{D_{lc}-D_{kc}}{2} \text{ for } i \neq j \text{ and } i>j \\
&\quad \text{where } k=i+j, \quad l=i-j \\
&= \frac{D_{mc}-D_{kc}}{2} \text{ for } i \neq j \text{ and } j>i \\
&\quad \text{where } k=i+j, \quad m=j-i \\
&\quad i=1,2,\dots \text{ and } j=1,2,\dots
\end{aligned} \tag{34}$$

Likewise, expressions similar to the above can be obtained for the elements of the LTI model matrices involving K , G , P , Q and R .

Example 1:

For example, if one considers only the average component (x_o) and the 4th harmonic components (x_{4c} , x_{4s}) for an approximate LTI model, with

$$x_{aug} = \left[x_o^T \quad x_{4c}^T \quad x_{4s}^T \quad \dot{x}_o^T \quad \dot{x}_{4c}^T \quad \dot{x}_{4s}^T \right]^T$$

then

$$\dot{x}_{aug} = \begin{bmatrix} A_{11} & & & & & \\ & A_{12} & & & & \\ & & A_{22} & & & \\ & & & & & \\ & & & & & \\ & & & & & \end{bmatrix} x_{aug} + [B]\mu$$

where

$$A_{11} = \begin{bmatrix} 0 & 0 & 0 \\ 0 & 0 & 0 \\ 0 & 0 & 0 \end{bmatrix}$$

$$A_{12} = \begin{bmatrix} I & 0 & 0 \\ 0 & I & 0 \\ 0 & 0 & I \end{bmatrix}$$

$$A_{21} = \begin{bmatrix} -H_{oK} & (-H_{oK_{4c}} + 4\Omega H_{oD_{4s}}) & (-H_{oK_{4s}} - 4\Omega H_{oD_{4c}}) \\ -H_{4cK} & (16\Omega^2 I - H_{4cK_{4c}} + 4\Omega H_{4cD_{4s}}) & (-H_{4cK_{4s}} - 4\Omega H_{4cD_{4c}}) \\ -H_{4sK} & (-H_{4sK_{4c}} + 4\Omega H_{4sD_{4s}}) & (16\Omega^2 I - H_{4sK_{4s}} - 4\Omega H_{4sD_{4c}}) \end{bmatrix}$$

$$A_{22} = \begin{bmatrix} -H_{oD} & -H_{oD_{4c}} & -H_{oD_{4s}} \\ -H_{4cD} & -H_{4cD_{4c}} & (-8\Omega I - H_{4cD_{4s}}) \\ -H_{4sD} & (8\Omega I - H_{4sD_{4c}}) & -H_{4sD_{4s}} \end{bmatrix}$$

$$[B]u = \begin{bmatrix} 0 \\ 0 \\ 0 \\ H_{oG}u_o + \sum_{m=1}^M (H_{oG_{mc}}u_{mc} + H_{oG_{ms}}u_{ms}) \\ H_{4cG}u_o + \sum_{m=1}^M (H_{4cG_{mc}}u_{mc} + H_{4cG_{ms}}u_{ms}) \\ H_{4sG}u_o + \sum_{m=1}^M (H_{4sG_{mc}}u_{mc} + H_{4sG_{ms}}u_{ms}) \end{bmatrix}$$

Example 2:

If one considers only the average and the 1st harmonic components only, with

$$x_{aug} = \begin{bmatrix} x_o^T & x_{1c}^T & x_{1s}^T & \dot{x}_o^T & \dot{x}_{1c}^T & \dot{x}_{1s}^T \end{bmatrix}^T$$

then

$$\dot{x}_{aug} = \begin{bmatrix} A_{11} & A_{12} \\ A_{21} & A_{22} \end{bmatrix} x_{aug} + \begin{bmatrix} B_1 \\ B_2 \end{bmatrix} u$$

where

$$A_{11} = \begin{bmatrix} 0 & 0 & 0 \\ 0 & 0 & 0 \\ 0 & 0 & 0 \end{bmatrix}$$

$$A_{12} = \begin{bmatrix} I & 0 & 0 \\ 0 & I & 0 \\ 0 & 0 & I \end{bmatrix}$$

$$A_{12} = \begin{bmatrix} -H_oK & (-H_oK_{1c} + \Omega H_oD_{1s}) & (-H_oK_{4s} - \Omega H_oD_{1c}) \\ -H_{1c}K & (\Omega^2 I - H_{1c}K_{1c} + \Omega H_{1c}D_{1s}) & (-H_{1c}K_{1s} - \Omega H_{1c}D_{1c}) \\ -H_{1s}K & (-H_{1s}K_{1c} + \Omega H_{1s}D_{1s}) & (\Omega^2 I - H_{1s}K_{1s} - \Omega H_{1s}D_{1c}) \end{bmatrix}$$

$$A_{22} = \begin{bmatrix} -H_oD & -H_oD_{1c} & -H_oD_{1s} \\ -H_{1c}D & -H_{1c}D_{1c} & (-2\Omega I - H_{1c}D_{1s}) \\ -H_{1s}D & (2\Omega I - H_{1s}D_{4c}) & -H_{1s}D_{1s} \end{bmatrix}$$

$$[B_1]u = \begin{bmatrix} 0 \\ 0 \\ 0 \end{bmatrix} \quad [B_2]u = \begin{bmatrix} H_oG u_o + \sum_{m=1}^M (H_oG_{mc} u_{mc} + H_oG_{ms} u_{ms}) \\ H_{1c}G u_o + \sum_{m=1}^M (H_{1c}G_{mc} u_{mc} + H_{1c}G_{ms} u_{ms}) \\ H_{1s}G u_o + \sum_{m=1}^M (H_{1s}G_{mc} u_{mc} + H_{1s}G_{ms} u_{ms}) \end{bmatrix}$$

LTI Models from FLIGHTLAB

The LTI model extraction method described in the previous section is implemented within FLIGHTLAB™ [38, 39] using the generalized force formulation written as

$$\Xi = f(U, X, \dot{X}, \ddot{X}) \quad (35)$$

where Ξ is the equation imbalance of Eq. (35). The control at each time step is iteratively solved to drive Ξ to zero for trim. The nonlinear model is first trimmed at a specified flight condition. Then a reference blade is set to the zero azimuth position and the periodic trim condition is recorded over one rotor revolution. With the reference blade at selected azimuthal steps, the values of Ξ due to perturbations in state/control are computed at each azimuthal step, and system matrices are obtained by computing the partial derivatives of Ξ with respect to individual state/control through central finite differencing. For example,

$$\frac{\partial f}{\partial X} \approx \frac{f(\bar{X} + \Delta X, \dot{\bar{X}}, \ddot{\bar{X}}, \bar{U}) - f(\bar{X} - \Delta X, \dot{\bar{X}}, \ddot{\bar{X}}, \bar{U})}{2\Delta X} \quad (36)$$

where ΔX is the selected value of the numerical perturbation. Likewise, partial derivatives of the output with respect to state/control perturbations are obtained. The numerically computed partial derivatives are used to assemble the LTP model matrices $D(\psi)$, $K(\psi)$, etc., using Eqs. (7) and (12) at the current azimuthal step. Also, additional components, such as $D(\psi)\cos(k\psi)$, $D(\psi)\sin(k\psi)$, $K(\psi)\cos(k\psi)$, $K(\psi)\sin(k\psi)$, etc., $k=0, 1, 2, \dots$ required for harmonic decomposition (see Eq. 28) are also generated at each azimuthal step of the linearization. Therefore, once the linearization process is completed over one rotor revolution, it only takes a few algebraic operations (using Eqs. 18 through 26 and 29 through 34) to obtain a LTI model of selected order. The linearization can be configured to generate either a full linearized model or a reduced order model as desired. For reduced order models, a quasi-static model reduction technique is applied by selecting the dynamically retained states while residualizing the neglected dynamics.

TASK 5: LTI MODEL FIDELITY EVALUATIONS

The objectives of this task are to carry out LTI model fidelity evaluations both in time and frequency domains using a generic helicopter flight dynamics model which includes the effects of individual blade control (IBC) and on-blade control (OBC).

This section provides an evaluation of the computational efficiency of the developed method for the extraction of LTI models from a nonlinear model of a generic helicopter. This is followed by a description of metrics used in LTI model fidelity evaluations. Next, fidelity evaluation results are provided for the case of individual blade control applications followed by results for the case of on-blade trailing edge flap control applications.

Computational Efficiency

Individual blade control (IBC) or On-Blade Control (OBC) inputs excite higher frequency response. A careful study is required to make an assessment on the number of harmonic states needed for good fidelity. As the number of harmonic rotor states required increases, the computational effort involved in the extraction of LTI model also increases. An assessment is made of the number of floating point operations (FLOPS) needed for a LTI model extraction. It is seen that with the current approach, the number of FLOPS increases linearly with an increase in the number of harmonic states of the LTI model. This is in contrast to roughly a quadratic increase in FLOPS with the number of harmonic states using the numerical scheme proposed in [15] which involves individual harmonic component perturbations.

Metrics for Evaluation of Model Fidelity

Tischler and Remple [40] suggest the use of the following metrics for checking the fidelity of flight mechanics models identified from test data in time and frequency domains:

Time-domain metric:

$$J^{(1)} = \sqrt{\frac{1}{n_t \cdot n_o} \sum_{i=1}^{n_t} [(\Delta y_{data} - \Delta y)_i^T W (\Delta y_{data} - \Delta y)_i]} \quad (37)$$

Frequency-domain metric:

$$J^{(2)} = \frac{20}{n_\omega} \sum_{\omega_1}^{\omega_{n_\omega}} W_\gamma \left[W_g (|T_c| - |T|)^2 + W_p (\angle T_c - \angle T)^2 \right] \quad (38)$$

$$\text{where } W_\gamma(\omega) = [1.58 \cdot (1 - e^{-\gamma \omega})]^2,$$

$$W_g = 1.0$$

$$W_p = 0.01745$$

The above metrics are adapted in this study by treating y_{data} as the response from the nonlinear model and y as the response from the LTI model. Δy in Eq. (37) is the perturbation time history of response from trim, n_t is the number of response points and n_o is the number of outputs. In Eq. (38), T_c is the transfer function from the nonlinear model, T is the transfer

function from the LTI model, γ_{xy} is the coherence function, and n_ω is the number of discrete frequency points used.

The normalized fixed system hub forces and moments are used as outputs for model evaluations in this study.

$$y = \begin{bmatrix} \frac{F_x}{m} & \frac{F_y}{m} & \frac{F_z}{m} & \frac{M_x}{I_{xx}} & \frac{M_y}{I_{yy}} & \frac{M_z}{I_{zz}} \end{bmatrix}^T \quad (39)$$

It is suggested in [40] that 1 deg/s error is equivalent to 1 ft/s or 1 ft/s². Here, this equivalence is extended to 1 deg/s² as well. Hence, the fixed system hub forces and moments are normalized by the vehicle mass and the corresponding mass moments of inertia, respectively, as shown in Eq. (39). The elements of the weighting matrix W in J of Eq. (37) are appropriately selected to achieve this equivalency. It is suggested in [40] that for good model fidelity, the value of the time domain error index ($J^{(1)}$) needs to be less than 1 ~ 2 and the value of the frequency domain error index ($J^{(2)}$) needs to be less than 100.

Helicopter Model for Fidelity Evaluations

A generic helicopter model available in FLIGHTLABTM is used for LTI model fidelity evaluations in this study. The vehicle weight is 15000 lb and it has a four bladed articulated rotor, conventional tail rotor, horizontal stabilizer and a vertical fin. The analog and digital SAS portions of the control system are disabled in this study. The nonlinear model includes one rigid plus one elastic mode for flap as well as lead-lag motions of each blade and a 15-state dynamic inflow model. The blade feathering is assumed to be rigid.

LTI Model Fidelity Evaluations with IBC

The number of average states in the LTI model is 55 which includes 8 body states (vehicle mass center velocity components, angular velocity components, body pitch and roll attitudes), 15 inflow states (4 harmonic distributions combining with 4th power radial representation [39]), and 32 Multi Blade Coordinate (MBC) rotor states (16 for the rigid flap and lead-lag motions and 16 for the elastic flap and lag motions). The number of harmonic components of rotor MBC states is 256 for the case when one includes 1/rev to 4/rev harmonic sine and cosine components (64 for rigid mode flap, 64 for elastic mode flap, 64 for rigid mode lead-lag and 64 for elastic mode lead-lag) resulting in a LTI model order of 311. When one includes 1/rev to 8/rev sine and cosine harmonics of rotor MBC states, the resulting LTI model order is 567, which includes 55 average states and 512 harmonic sine and cosine components of rotor MBC states. In case of an isolated rotor representation, the body states are absent, thus reducing the LTI model order by 8.

LTI model fidelity evaluations are carried out for a forward flight case of 0.15 advance ratio. The types of IBC inputs used are taken to be similar to those used in the literature for vibration and noise control applications (for example, see [3, 4, 7]). In time domain evaluations, the simulation time is set at 5 seconds for all cases. In each case, simulation begins at trim, and the selected input is applied at 1 sec into the simulation. The input is turned off at 3 sec into the run, and the simulation is continued till 5 sec. All fidelity evaluations in this study are carried out

using the generic helicopter model with an elastic blade representation and a 15-state dynamic inflow model.

For frequency domain evaluations, time response is extracted using a sine sweep excitation in the input channel in order to obtain frequency response. Tabulated time data is transferred as an input to CIPHER [40]. CIPHER performs frequency response analyses using 5 different window sizes within its FRESPID module. Each FRESPID result with a different window size becomes an input to the COMPOSITE module in order to obtain frequency response from a set of input/output data.

Appropriate time response data can be obtained with proper sampling rate, response duration and excitation of frequencies of interest. A sine sweep input is used in the frequency response analysis with varying frequency. The initial and final frequencies are selected to obtain a broad band of frequency response. The starting frequency is taken to be close to the lowest body mode and the final frequency is taken to be N_b/rev harmonic where N_b is number of blades. Duration of the signal is determined based on the CIPHER guideline [40] as 2.5 times the highest period.

Time Domain Evaluations using IBC

Higher harmonic inputs (2/rev, 3/rev, 4/rev, etc.) are used in the literature for reductions in vibration, noise and rotor power [3, 4, 7]. For reducing rotor power, a 2/rev individual blade control (IBC) input is suggested in [3]. In order to evaluate the fidelity of the extracted LTI models for their use in active rotor power reduction studies, a 2/rev IBC input of 2° magnitude (similar in magnitude to what has been tried in [3]) and (an arbitrarily selected) 125° phase is used in the LTI model fidelity evaluations. The resulting fixed hub load variations with time as predicted from FLIGHTLAB and from the extracted LTI model are compared in Figure 72a. The LTI model includes up to 4/rev harmonic components of rotor MBC states. Figure 72b is a zoom-in of results from Figure 72a. The time-domain error index computed using Eq. (37) is obtained as 0.316 indicating good fidelity of the extracted LTI model. It is interesting to see that 2/rev IBC inputs impact the steady state components of rotor thrust and torque as evident from the response predictions of F_z and M_z in Figure 72a.

It is well known that N/rev vibration in the fixed system arises from blade force variations in the rotating frame at $(N-1)/\text{rev}$, N/rev and $(N+1)/\text{rev}$ vibrations, where N is the number of blades [41]. Hence, as suggested from several studies in the literature (for example, [3]), it is expected that IBC inputs at these frequencies can be used for vibration control. An IBC input consisting of 3/rev, 4/rev and 5/rev components is used as a way to test the fidelity of the extracted LTI models for their use in active vibration control studies. The magnitudes of the harmonic components of IBC are selected to be 1.5° of 3/rev, 1° of 4/rev and 0.5° of 5/rev. These values are similar to the IBC harmonic component magnitudes used in [3]. The phases of the individual harmonic components of IBC are selected arbitrarily. The extracted LTI model includes up to 4/rev harmonic components of rotor states. The fixed system hub load responses to the selected IBC input as predicted from FLIGHTLAB is compared with those predicted using the LTI model in Figure 73a with a zoom-in of the results shown in Figure 73b. The time-domain error index computed using Eq. (37) is obtained as 0.612 indicating good model fidelity of the extracted LTI model, suggesting that the proposed LTI model extraction process can be used in active vibration control studies.

It is suggested in [4] that a combination of 6/rev and 7/rev may be used for simultaneous vibration and noise control. In order to verify the LTI model fidelity for its use in active vibration and noise control studies, a test case IBC input with 6/rev and 7/rev components of magnitudes (0.5° of 6/rev and 0.5° of 7/rev) similar to those considered in [4] is used. Two different orders of LTI model approximations are used, one that includes up to 4/rev harmonic components of rotor states and the second one that includes up to 8/rev harmonic components of rotor states. The predicted fixed system hub load responses from FLIGHTLAB are compared with those from the LTI model predictions in Figure 74a with a zoom-in of the results shown in Figure 74b. It is seen that the inclusion of up to 8/rev harmonic components of rotor states in the LTI model improves the LTI model fidelity significantly (error index of 0.037) when compared to that of the LTI model with only up to 4/rev harmonic components of rotor states (error index 0.71). The higher frequency variations in the fixed hub load responses seen in the FLIGHTLAB results are well captured in the predictions from the LTI model that includes up to 8/rev harmonic components of rotor states (see Figure 74b).

Next, the LTI model fidelity is evaluated using pulse inputs of IBC when a blade is passing through a selected azimuthal range. This input has been suggested in the literature [7] for avoidance of blade vortex interactions (BVI) using a trailing edge flap actuation. A similar type of input is used with IBC in the present study. The selected IBC input as a function of rotor azimuth angle is shown in Figure 75. The isolated rotor with the elastic blade and 15-state dynamic inflow model is used in this case. The predicted flapping response is shown in Figure 76 in terms of vertical deflection from the hub (shown in inches) at three different locations along the radius of a reference blade. A visual comparison of the isolated rotor elastic blade flapping responses from FLIGHTLAB and those from the LTI model indicates that the fidelity of the extracted LTI model is good, suggesting that the proposed LTI model extraction process can be used in active BVI control studies.

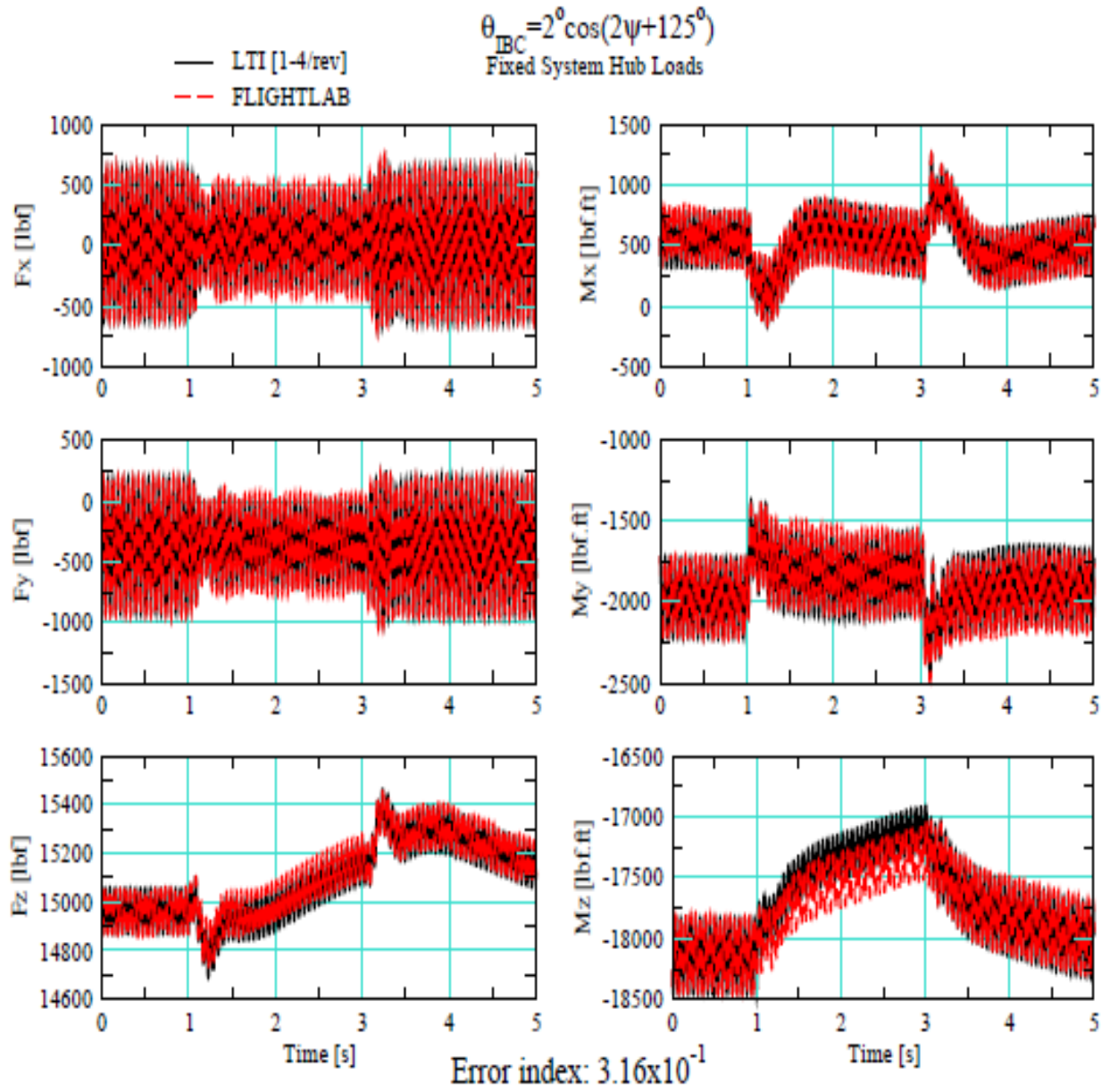


Figure 72a. Predicted Fixed System Hub Load Variations to 2/rev IBC Input.

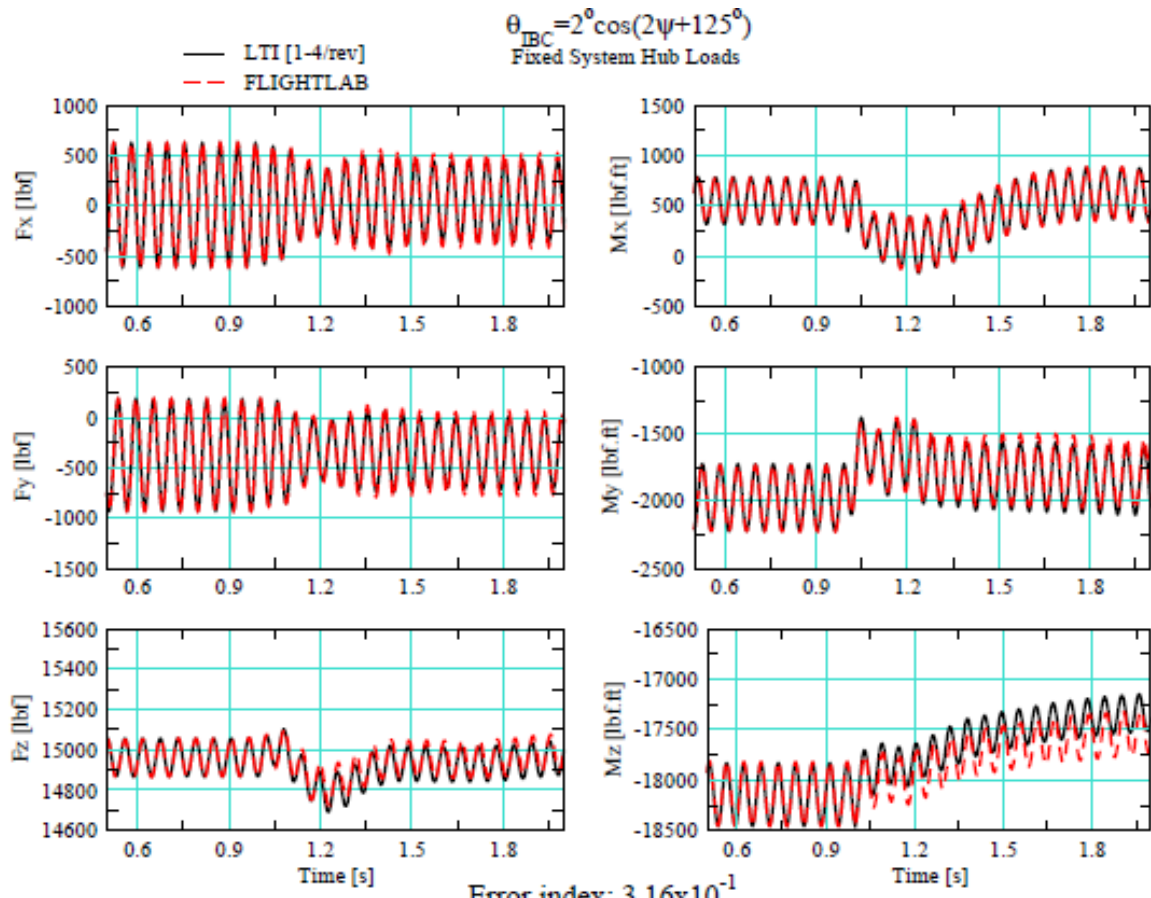


Figure 72b. A Zoom-In of Fig. 72a.

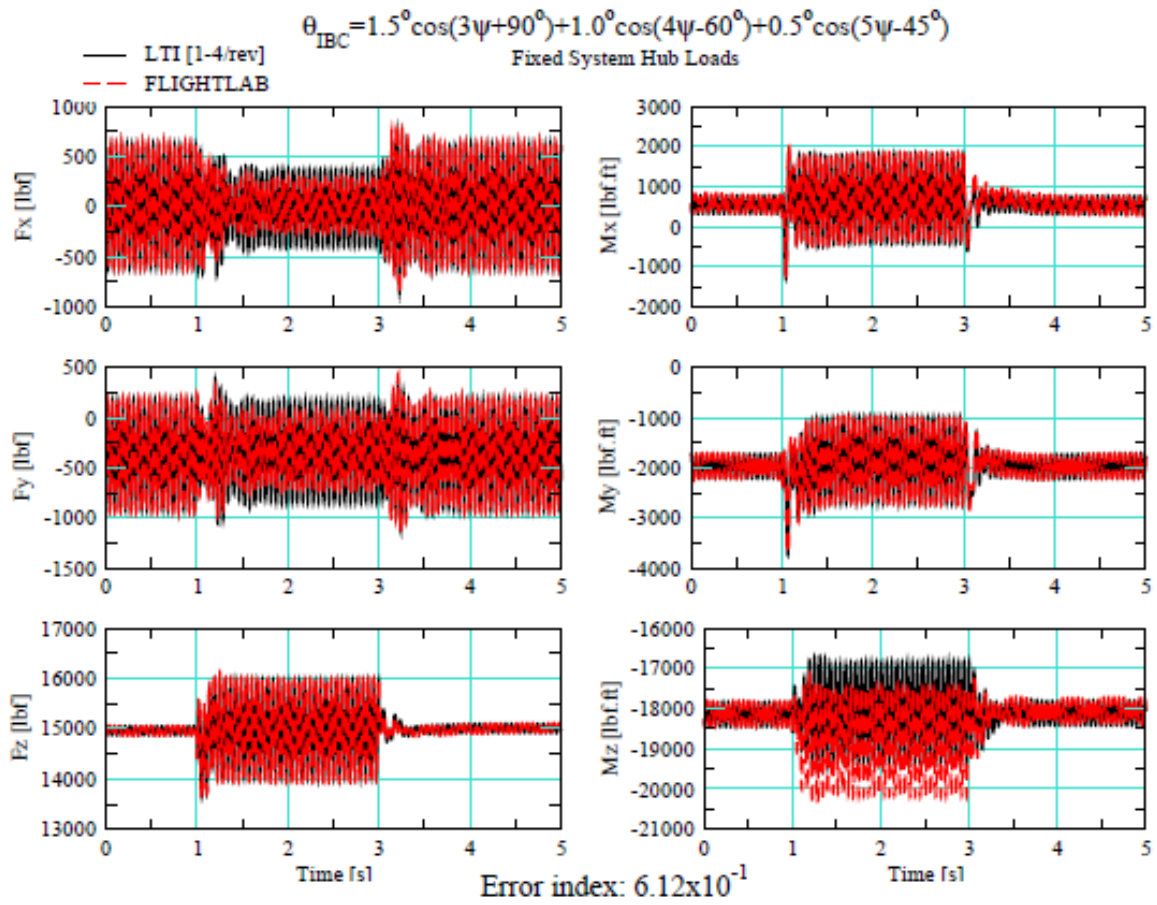


Figure 73a. Predicted Fixed Stem Hub Load Variations to IBC Inputs with 3/rev, 4/rev and 5/rev Components.

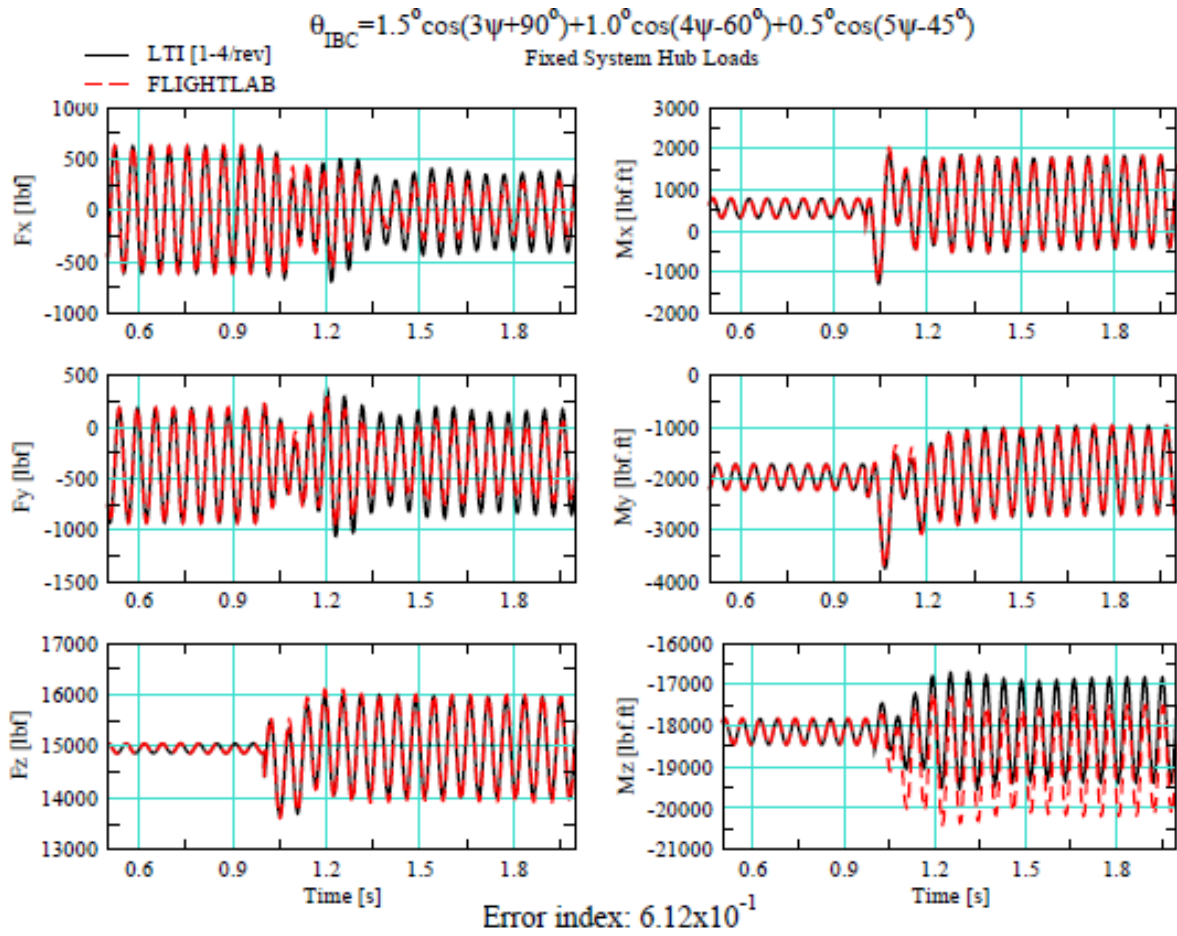


Figure 73b. A zoom-In of Fig. 73a.

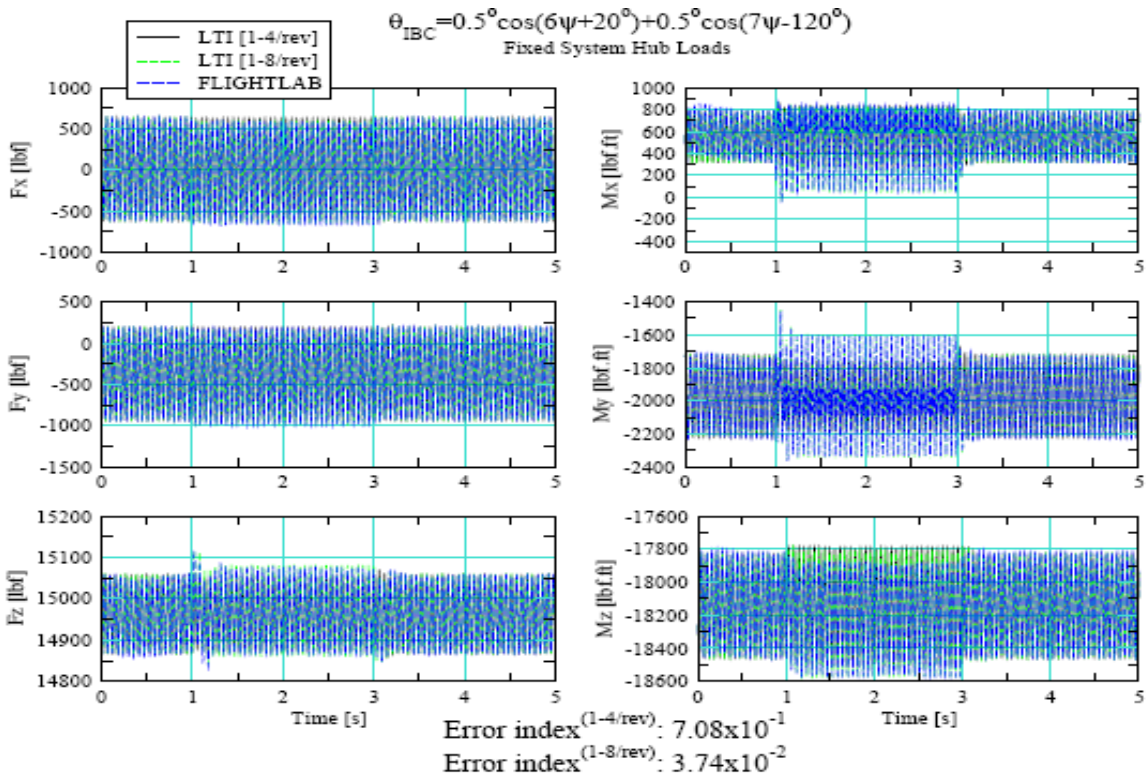


Figure 74a. Predicted Fixed Stem Hub Load Variations to IBC Inputs with 6/rev and 7/rev Components.

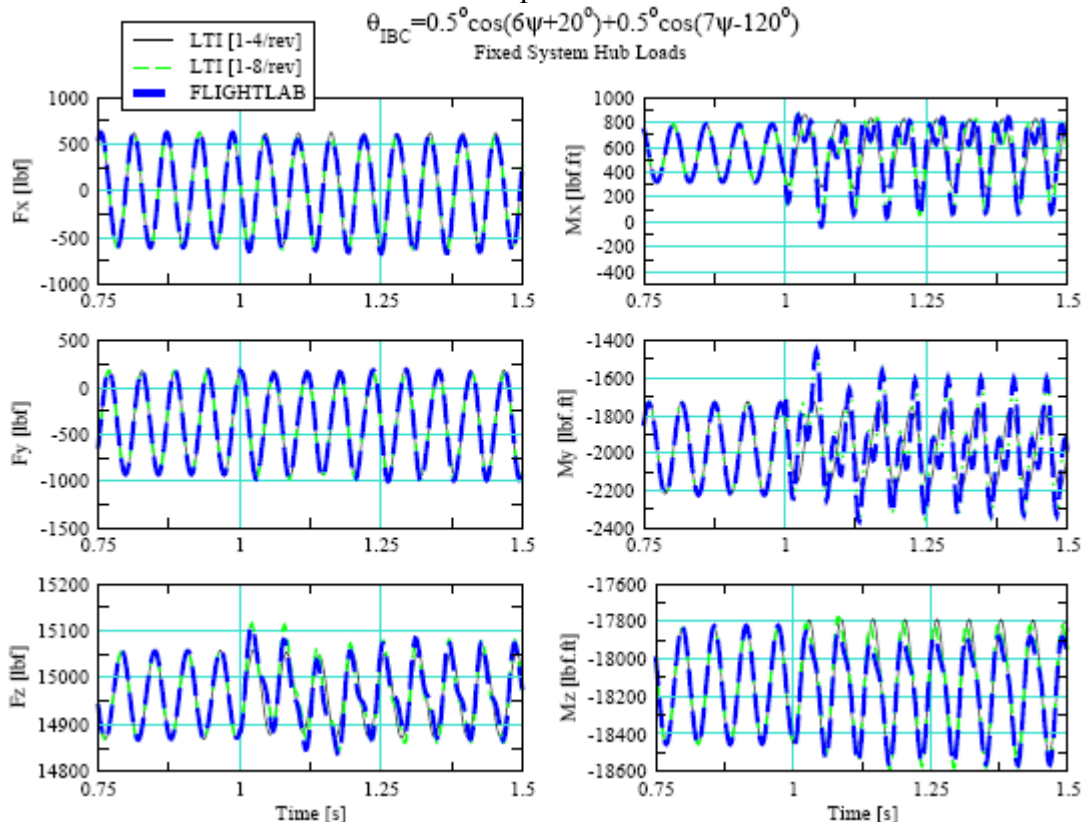


Figure 74b. A Zoom-In of Fig. 74a.

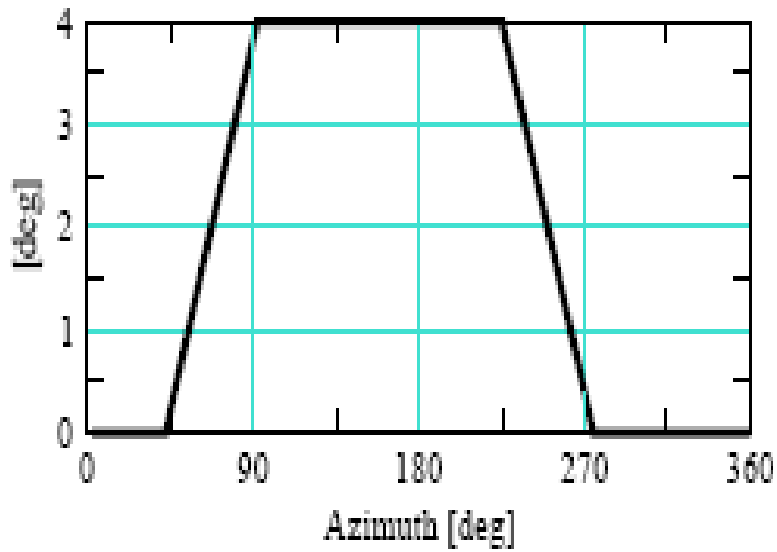


Figure 75. Selected Azimuth Dependent IBC Input.

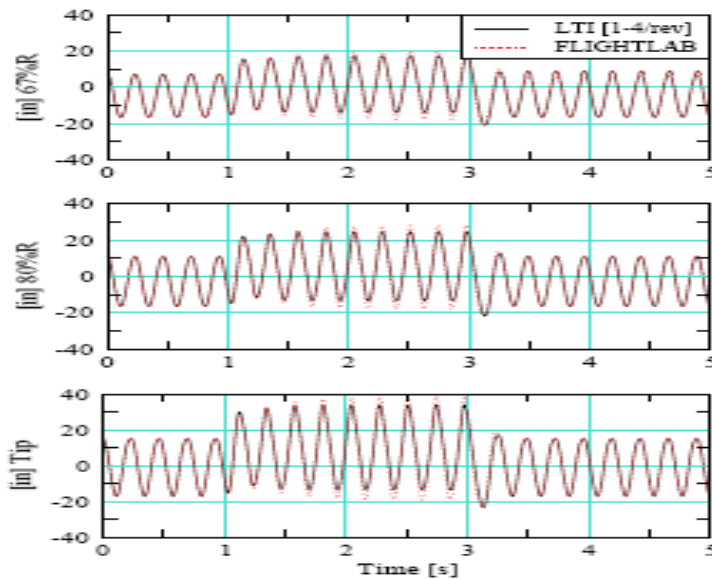


Figure 76. Predicted Elastic Blade Vertical Deflection (inches) in Response to the Selected IBC Pulse Input.

Frequency Domain Evaluations using IBC

The Comprehensive System Identification from Frequency Responses (CIFER) [40] is used to obtain frequency responses between the fixed system hub loads and a single blade IBC input.

Both FLIGHTLAB and LTI models are excited through a single blade IBC frequency sweep input. The frequency sweep magnitude is set at 1 deg and the frequency is linearly varied from 0.3 rad/sec to 135 read/sec ($=5\Omega$) with time. The duration of the frequency sweep is set at 120 seconds and the azimuthal increment (sampling rate) is set at $\Delta\psi=2.5^\circ$. Five different sizes of moving windows (24 sec, 12sec, 8 sec, 2 sec and 1 sec) are used in the construction of a composite frequency response from the frequency sweep input and output data. The generic helicopter with the elastic blade and 15-state dynamic inflow model is used.

The predicted frequency responses between the fixed system rotor thrust (F_z) and rotor torque (M_z) to single blade IBC input are shown in Figures 77 and 78, respectively. The frequency domain error index for model fidelity is computed using Eq. (38), which are obtained as 17.6 and 16.8 for the cases of F_z and M_z cases, respectively. These values are well within the bound of 100 suggested in [40], indicating a good fidelity of the extracted LTI model.

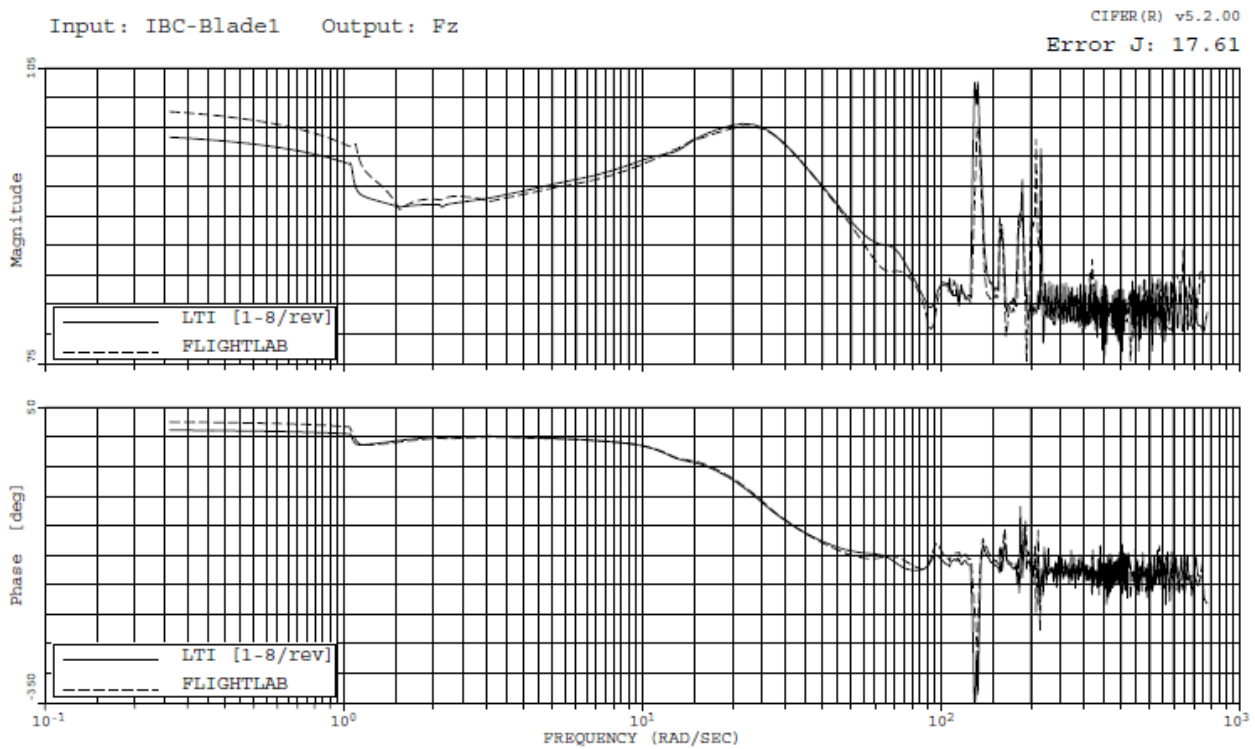


Figure 77. Predicted Frequency Response of Rotor Thrust to a Single Blade IBC Input.

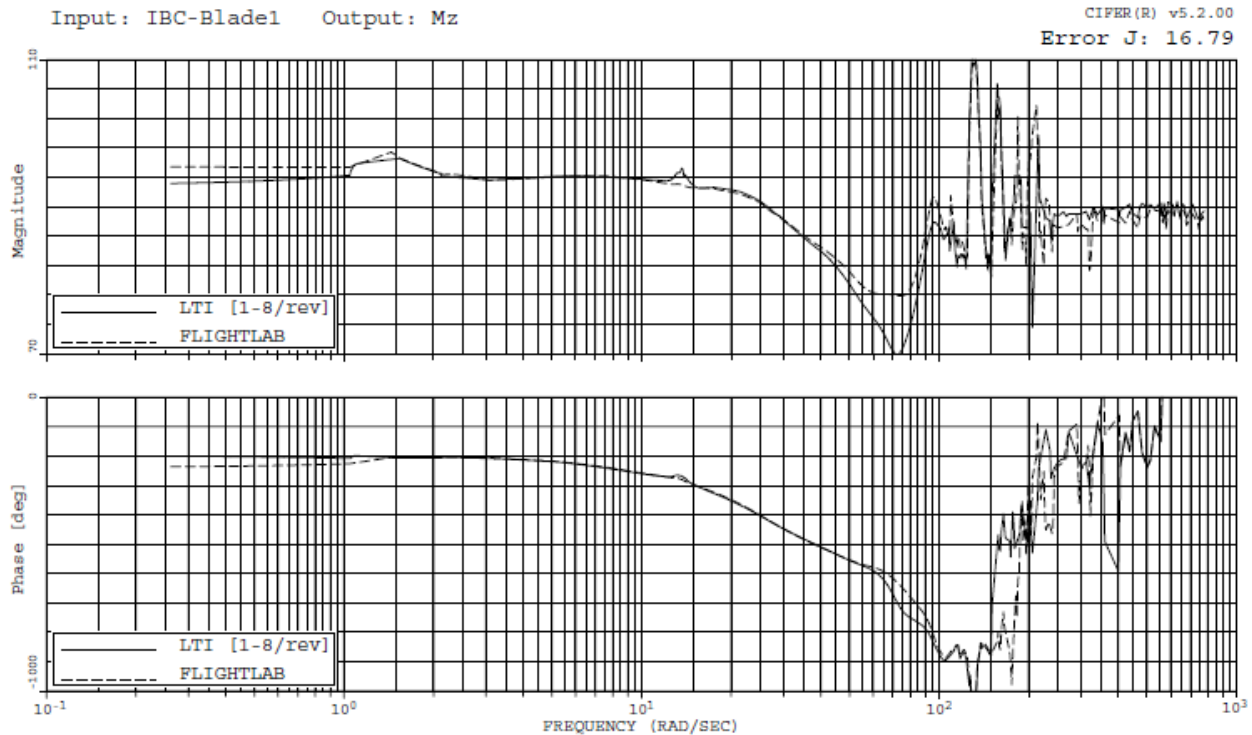


Figure 78. Predicted Frequency Response of Rotor Torque to a Single Blade IBC Input.

LTI Model Fidelity Evaluations with OBC

LTI model fidelity evaluations with OBC are carried out for an advance ratio of 0.15. The types of inputs used in this study are taken from vibration and performance enhancement studies from the literature. In all cases considered, each simulation is carried out over 2.5 seconds with the selected TEF input turned on for 1 second over 0.5 sec to 1.5 sec interval. The predicted fixed system hub forces and moments are shown for each evaluation case. As the scope of this study is limited to validation of LTI models and not necessarily to determine the optimum input needed for vibration reduction etc., an arbitrary phasing is used for the harmonic input while the magnitudes of the inputs are taken to be relatively similar to those used in past experimental studies. All fidelity evaluations in this study are carried out using the modified version of a generic helicopter model with an elastic blade representation and 33-state inflow model. The number of states (N_s) for the extracted LTI model is given by

$$N_s = ns_o + ns_r(2 \cdot n_h + 1)$$

where n_h is the number of harmonics, ns_o is the number of body and inflow states, and ns_r is the number of rotor MBC states. Due to the nature of the aerodynamic effects from TEF deflections,

higher harmonic excitations are expected, and hence, up to 8/rev harmonic representation is used in all of the evaluations.

For frequency domain evaluations, time response is extracted using a sine sweep excitation in the input channel in order to obtain frequency response. Tabulated time data is transferred as an input to CIPHER [40]. CIPHER performs frequency response analyses using 5 different window sizes within its FRESPID module. Each FRESPID result with a different window size becomes an input to the COMPOSITE module in order to obtain frequency response from a set of input/output data.

Appropriate time response data can be obtained with proper sampling rate, response duration and excitation of frequencies of interest. A sine sweep input is used in the frequency response analysis with varying frequency. The initial and final frequencies are selected to obtain a broad band of frequency response. The starting frequency is taken to be close to the lowest body mode and the final frequency is taken to be N_b /rev harmonic where N_b is number of blades. Duration of the signal is determined based on the CIPHER guideline [40] as 2.5 times the highest period.

Time Domain Evaluations using OBC

Higher harmonic inputs (2/rev, 3/rev, 4/rev, etc.) are used in the literature for reductions in vibration, noise and rotor power [3-5]. For reducing rotor power, a 2/rev individual blade control (IBC) input is suggested in [3]. In order to evaluate the fidelity of the extracted LTI models for their use in active rotor power reduction studies, a 2/rev TEF input of 0.5° magnitude and (an arbitrarily selected) 70° phase is used in the LTI model fidelity evaluations. The resulting fixed hub load variations with time as predicted from FLIGHTLAB and from the extracted LTI model are compared in Figure 79a. The LTI model includes up to 8/rev harmonic components of rotor MBC states. These include rigid (flap & lag) and elastic modes (first elastic flap and first elastic lag), both. Figure 79b is a zoom-in of results from Figure 79a. The time-domain error index computed using Eq. (37) is less than 0.001 indicating good fidelity of the extracted LTI model.

It is well known that N /rev vibration in the fixed system arises from blade force variations in the rotating frame at $(N-1)$ /rev, N /rev and $(N+1)$ /rev vibrations, where N is the number of blades [41]. Hence, as suggested from several studies in the literature (for example, [3]), it is expected that OBC inputs at these frequencies can be used for vibration control. A TEF input consisting of 3/rev, 4/rev and 5/rev components is used as a way to test the fidelity of the extracted LTI models for their use in active vibration control studies. The magnitudes of the harmonic components of TEF inputs are selected to be 1.0° of 3/rev, 0.5° of 4/rev and 0.25° of 5/rev. The phases of the individual harmonic components are selected arbitrarily. The extracted LTI model includes up to 8/rev harmonic components of rotor states. The fixed system hub load responses to the selected TEF input as predicted from FLIGHTLAB is compared with those predicted using the LTI model in Figure 80a with a zoom-in of the results shown in Figure 80b. Even though there is slight deviation in terms of both magnitude and phase visible in the zoom-in plot Figure 80b, the computed time-domain error index of 0.0135 indicates good model fidelity of the extracted LTI model.

It is suggested in [3] that a combination of 6/rev and 7/rev may be used for simultaneous vibration and noise control. In order to verify the LTI model fidelity for its use in active vibration and noise control studies, a test case TEF input with 6/rev and 7/rev components of magnitudes

(0.25° of both 6/rev and 7/rev) similar to those considered in [3] is used. The predicted fixed system hub load responses from FLIGHTLAB are compared with those from the LTI model predictions in Figure 81a with a zoom-in of the results shown in Figure 81b. Once again, these results demonstrate the fidelity of the extracted LTI models.

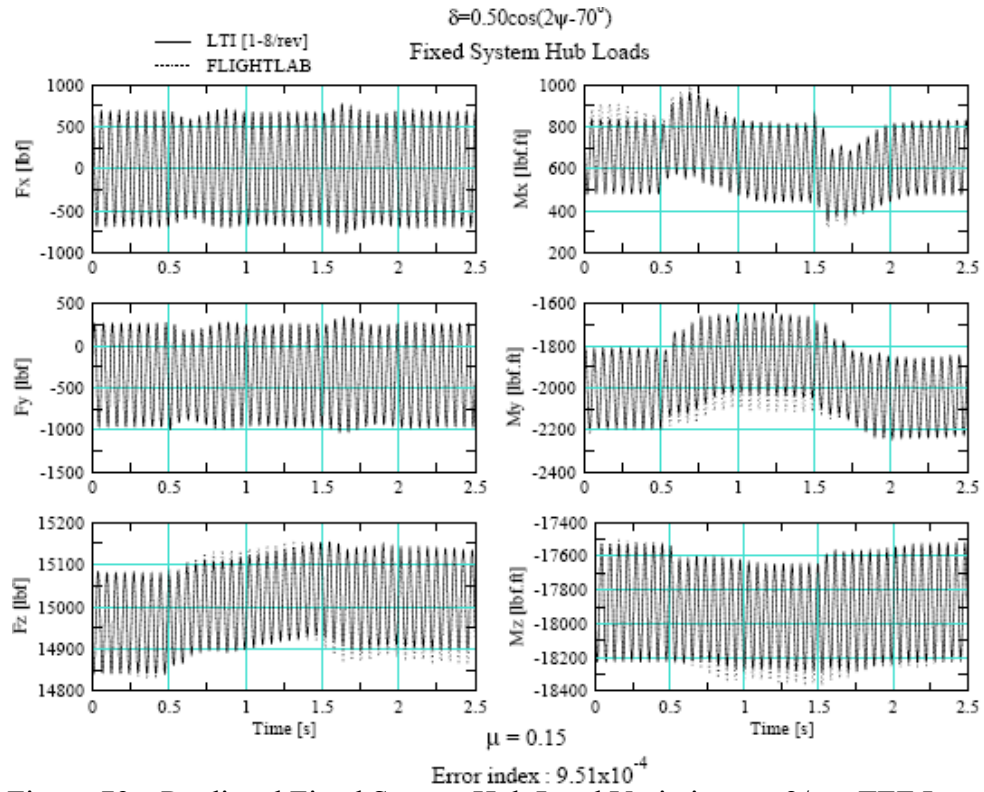


Figure 79a. Predicted Fixed System Hub Load Variations to 2/rev TEF Input

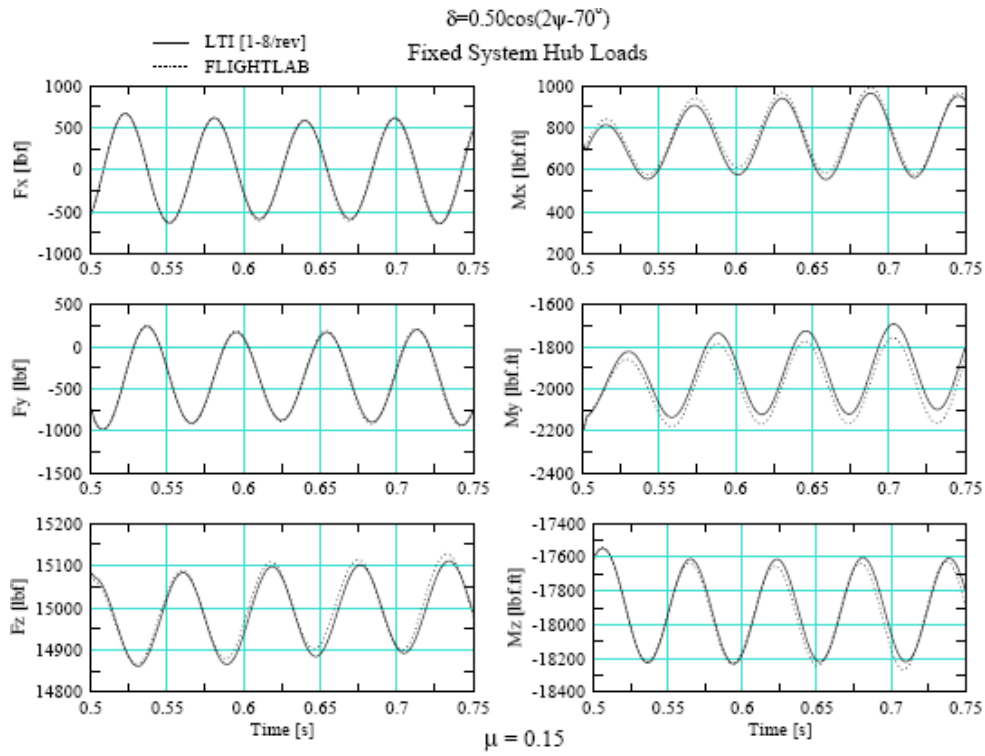


Figure 79b. Zoom-in of Fig. 79a.

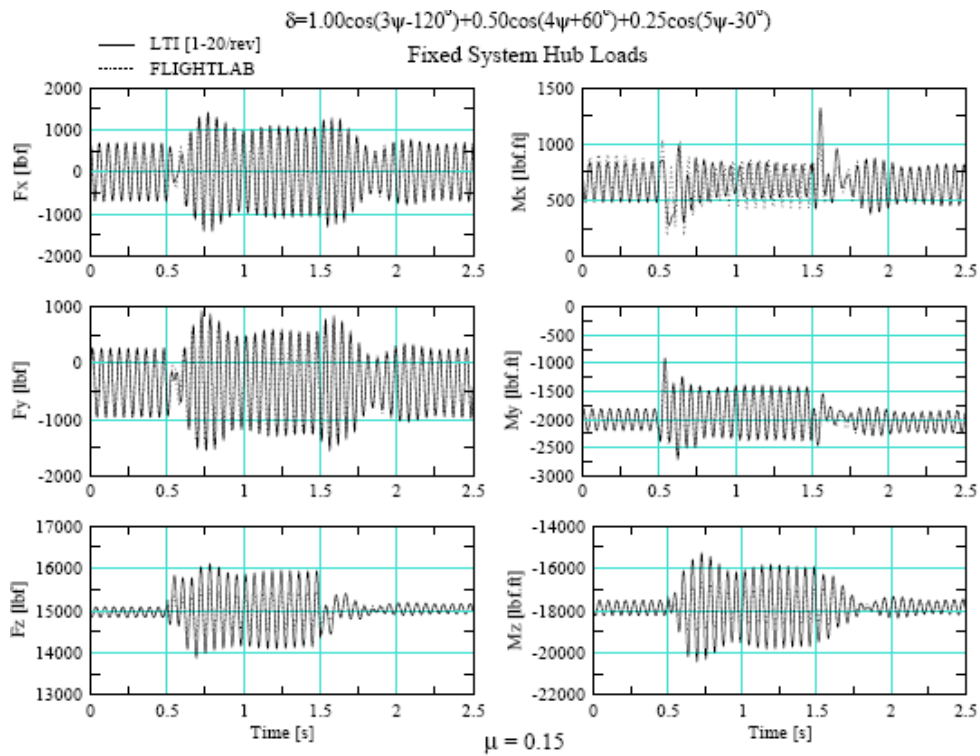
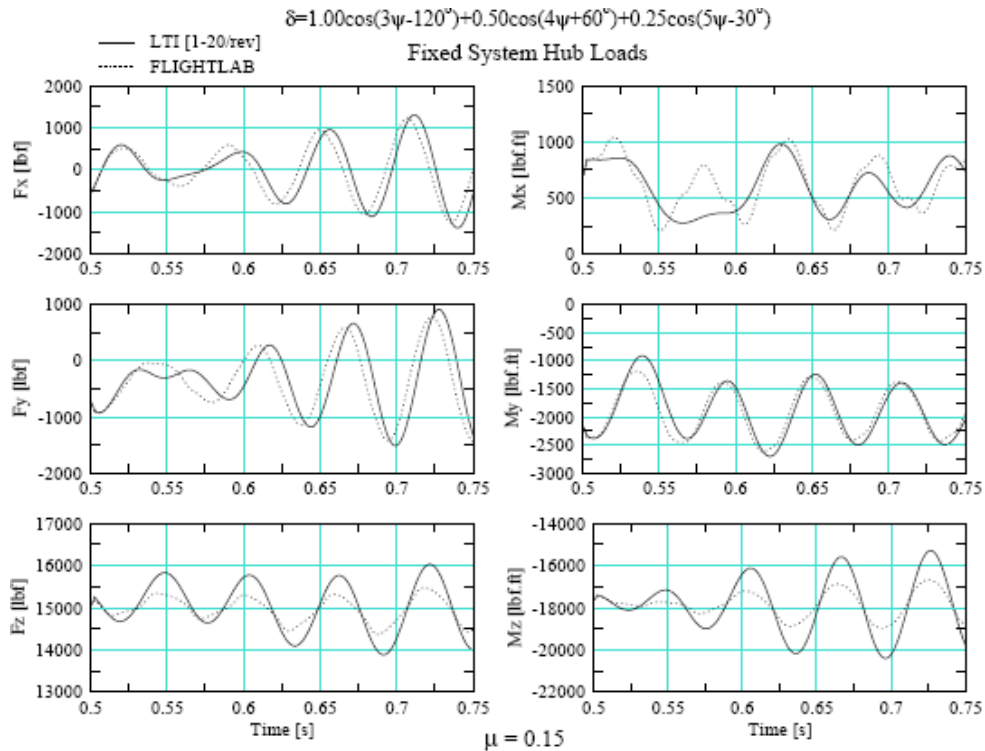
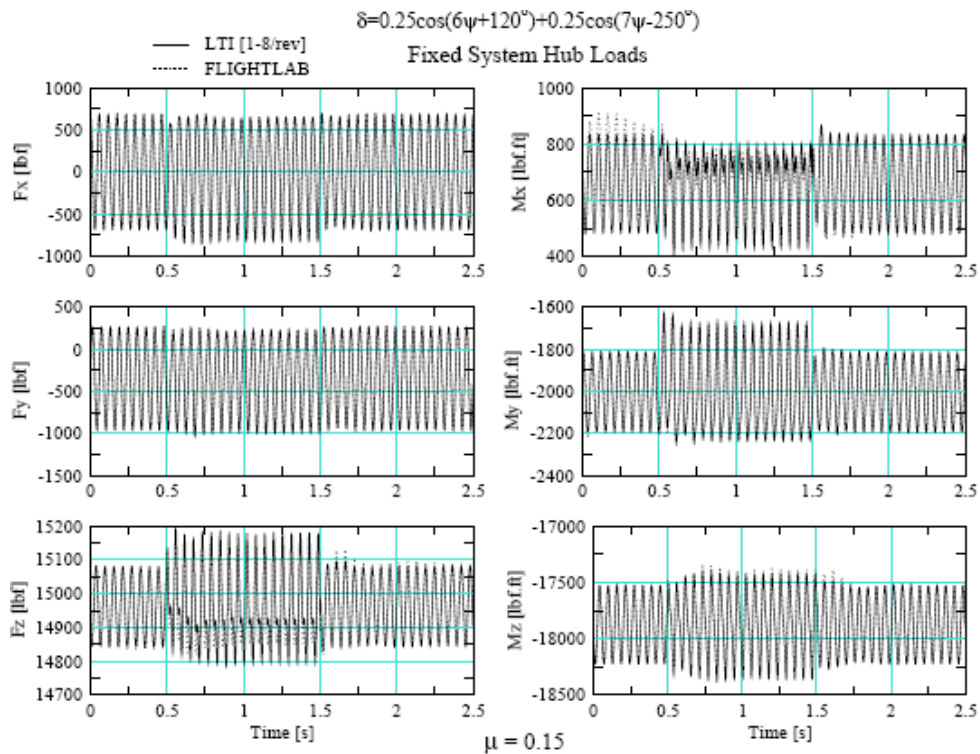


Figure 80a. Predicted Fixed System Hub Load Variations to Combination of 3,4 & 5/rev TEF Input



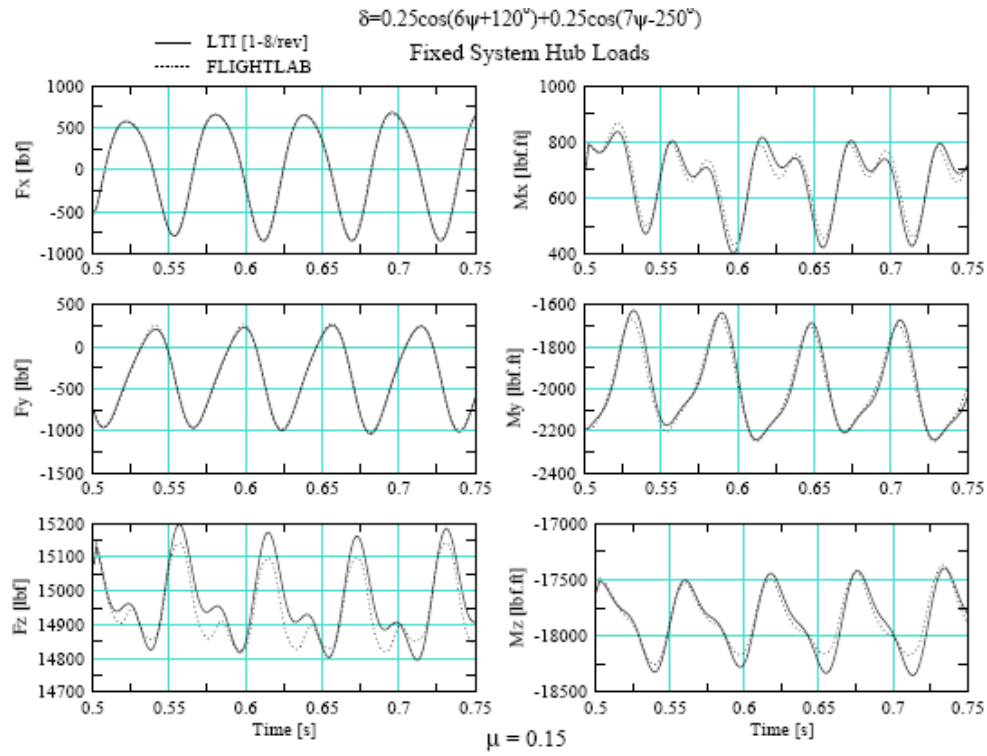
Error index : 1.35×10^{-1}

Figure 80b. Zoom-in of Fig. 80a.



Error index : 1.19×10^{-3}

Figure 81a. Predicted Fixed System Hub Load Variations to Combination of 6 & 7/rev TEF Input (1-8/rev)



Error index : 1.19×10^{-3}

Figure 81b. Zoom-in of Fig. 81a..

Frequency Domain Evaluations using OBC

In Figures 82 and 83 the computed frequency responses of rotor thrust and torque due to TEF inputs are shown. The selected TEF deflection magnitudes and rates considered as inputs are adjusted so as to ensure that the resulting aerodynamic effects due to TEF deflections stay within the linear range of the trained NNET. The composite responses of rotor thrust and torque along with the TEF inputs are used in CIFER [40] to arrive at frequency responses from TEF input to rotor thrust and TEF input to rotor torque. Figures 82 and 83 provide frequency response comparisons between FLIGHTLAB and LTI model results. The value of the frequency domain error index computed using Eq. (38) is 22.86 for the rotor thrust frequency response results and 4.57 for the rotor torque response results. These values are well within the suggested value of less than 100 for good model fidelity [40].

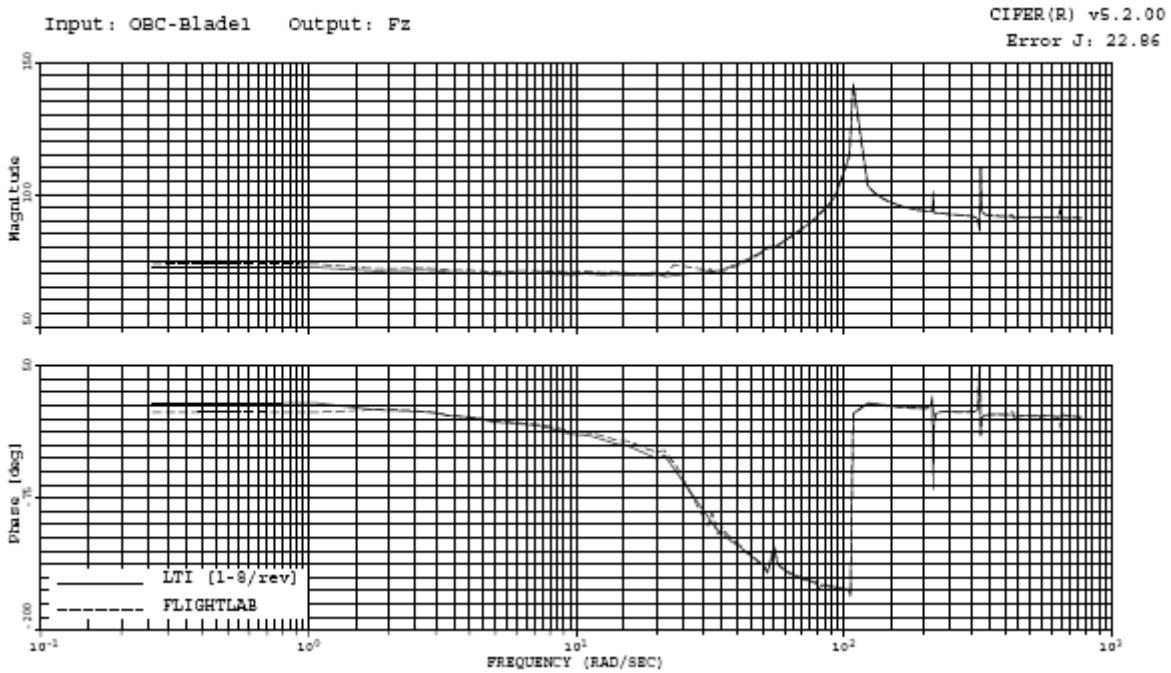


Figure 82. Predicted Frequency Response of Rotor Thrust to a Single Blade TEF Input.

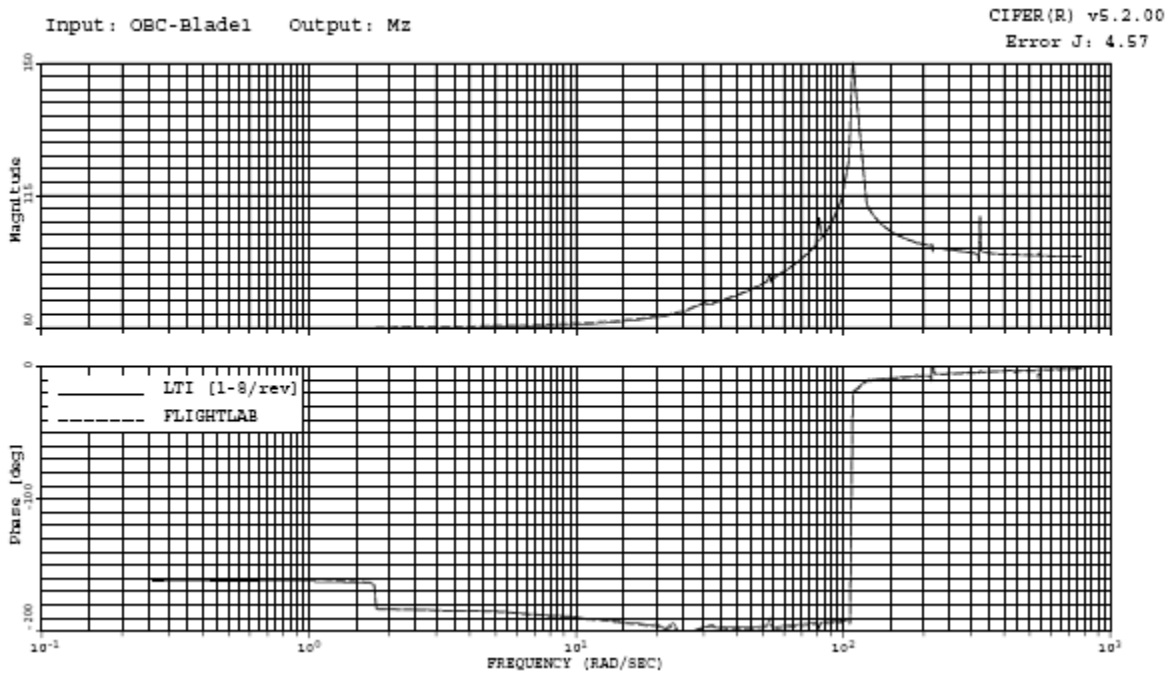


Figure 83. Predicted Frequency Response of Rotor Torque to a Single Blade TEF Input.

CONCLUDING REMARKS

A methodology for developing reduced order air loads models of on-blade control concepts based on artificial neural networks (NNET) is described in this study. The developed methodology consists of three steps; creating a CFD database for a selected OBC concept, training of a NNET as an addition to an existing baseline air loads model in order to capture the CFD data base to the required level of fidelity, and integration of the developed NNET of the selected OBC concept into a nonlinear helicopter model. The proposed methodology is evaluated for the case of a rotor blade with a trailing edge flap actuator.

Formulation of linear time invariant (LTI) models of a nonlinear system about a periodic equilibrium using the harmonic domain representation of LTI model states is well established in the literature. A computationally efficient scheme for extraction of linear time invariant (LTI) models of a nonlinear helicopter model about a periodic equilibrium is developed in this study. The developed computational approach makes use of closed form expressions relating various elements of a LTI model with harmonic components of a corresponding linear time periodic (LTP) model. A numerical perturbation scheme is used to compute various elements of a LTP model at discrete azimuthal steps over one rotor revolution from a helicopter nonlinear model about a periodic equilibrium. Simultaneously, computations needed for decomposition of LTP model matrices into harmonic components are performed. Once the linearization for a LTP model is completed over one rotor revolution, it takes only a few algebraic operations to assemble a LTI model of selected order. The developed numerical scheme is seen to improve computational speed by an order magnitude when it is compared with the numerical scheme from the literature involving individual harmonic components of state/control perturbations.

The developed computational scheme is implemented within FLIGHTLABTM and is used to extract LTI models of a generic helicopter nonlinear model in forward flight. The fidelity of the extracted LTI models is evaluated in both time and frequency domains by using error metrics from the literature. Simulation comparisons are made between the nonlinear model and the extracted linear models using predicted fixed system hub load responses to typical individual blade control (IBC) inputs that have been suggested in the literature for vibration and noise control applications. The evaluation results demonstrate the fidelity of the extracted LTI models, and thus, establish the validity of the LTI model extraction process for its use in integrated flight and rotor control studies.

The developed methodology for reduced order modeling of on-blade control concepts through artificial neural networks is evaluated for a selected case of airfoil and trailing edge flap combination. Future work is needed to evaluate the proposed reduced order modeling methodology by considering other types of on-blade control actuation, such as leading edge slats, micro trailing edge flaps, etc.

ACKNOWLEDGMENTS

The feedback received from Dr. Wayne Johnson and Mr. Bill Decker of NASA Ames and Dr. Mark Tischler of Aeroflightdynamics Directorate (AMRDEC) at NASA Ames throughout the course of this project is gratefully acknowledged.

REFERENCES

1. Shaw, J., Albion, N., Hanker, E.J. and Teal, R.S, "Higher Harmonic Control: Wind Tunnel Demonstration of Fully Effective Vibratory Hub Force Suppression", AHS 41st Annual Meeting, Texas, May 15-17, 1985.
2. Jacklin S.A. et al., "Full-Scale Wind Tunnel Test of the McDonnell Douglas Five-Bladed Advanced Bearingless Rotor: Performance, Stability, Loads, Control Power, Vibration and HHC Data", American Helicopter Society Aeromechanics Specialists Conference, San Francisco CA, January 19-21, 1994.
3. Jacklin, S. A., Blaas, A., Teves, D. and Kube, R., "Reduction of Helicopter BVI Noise, Vibration, and Power Consumption through Individual Blade Control," Proceedings of the 51st Annual Forum of the American Helicopter Society, Fort Worth TX, May 9-11, 1995.
4. Swanson, S. M., Jacklin, S. A., Blaas, A., Niesl, G. and Kube, R., "Acoustic Results from a Full-Scale Wind Tunnel Test Evaluating Individual Blade Control," Proceedings of the 51st Annual Forum of the American Helicopter Society, Fort Worth TX, May 9-11, 1995.
5. Norman et al., "Low-Speed Wind Tunnel Investigation of a Full-Scale UH-60 Rotor System", Proceedings of the 58th Annual Forum of the American Helicopter Society, Montreal Canada, June 11-13, 2002.
6. Jacklin et al., "Full-Scale Wind Tunnel Test of an Individual Blade Control System for a UH-60 Helicopter", Proceedings of the 58th Annual Forum of the American Helicopter Society, Montreal Canada, June 11-13, 2002.
7. Dawson et al., "Wind Tunnel Test of an Active Flap Rotor: BVI Noise and Vibration Reduction," Proceedings of the 51st Annual Forum of the American Helicopter Society, Fort Worth TX, May 9-11, 1995.
8. Kottapalli, S. and Straub, F., "Correlation of Smart Active Flap Rotor Loads", Proceedings of the 65th Annual Forum of the American Helicopter Society, Grapevine TX, May 27-29, 2009.
9. Montanye et al., "Shipboard Helicopter Gust Alleviation Using Active Trailing Edge Flaps", Proceedings of the 65th Annual Forum of the American Helicopter Society, Grapevine TX, May 27-29, 2009.
10. Arnold, U.T.P., Fürst, D., Neuheuser, T. and Bartels, R., "Development of an Integrated Electrical Swashplateless Primary and Individual Blade Control System", Cheeseman Award Paper of the 32nd European Rotorcraft Forum, Maastricht, 2006.
11. Boyd, D.D., "HART-II Acoustic Predictions using a Coupled CFD/CSD Method", Proceedings of the 65th Annual Forum of the American Helicopter Society, Grapevine TX, May 27-29, 2009.
12. Cheng, R.P., Tischler, M.B. and Celi, R., "A Higher-Order, Time-Invariant, Linearized Model for Application to HHC/AFCS Interaction Study," Proceedings of the 59th Annual Forum of the American Helicopter Society, Phoenix, AZ, May 6-8, 2003.
13. Pandyan, R. and Sinha, S.C., "Time-Varying Controller Synthesis for Nonlinear Systems subjected to Periodic Parametric Loading," Journal of Vibration and Control, Vol. 7, pp73-90, 2001.
14. Colaneri, P., Celi, R. and Bittanti, S., "Constant Coefficient Representations of Discrete Periodic Linear Systems," Proceedings of the 4th Decennial Specialists' Conference on Aeromechanics, San Francisco, CA, Jan 21-24, 2004.

15. Cheng, R.P., Tischler, M.B. and Celi, R., "A High Order, Linear Time Invariant Model for Application to Higher Harmonic Control and Flight Control Systems," NASA-TP-2006-213460, 2006.
16. Chandrasekhara, M. S. and Carr, L. W., "Unsteady stall Control using Dynamically Deforming Airfoils," AIAA Journal, Vol. 36, No. 10, 1998.
17. Sahin, M., Sankar L. N., Chandrasekhara, M. S., Tung, C. "Stall alleviation Using a Deformable Leading Edge Concept," AIAA 2000-0520, 38th AIAA Aerospace Sciences Meeting, Reno, NV 2000.
18. Bhagwat, M.J., Dimanlig, A., Saberi, H., Meadowcroft, E., Panda, B., Strawn, R., "CFD/CSD Coupled Trim Solution for the Dual-Rotor CH-47 Helicopter Including Fuselage Modeling," AHS Specialist Conference on Aeromechanics, San Francisco, CA, January 2008.
19. Duque, E.P.N, Sankar, L.N, Menon, S., Bauchau, O., Ruffin, S., Smith, M., Ahuja, A., Brentner, K.S., Long, L.N., Morris, P.J., Gandhi, F., "Revolutionary Physics-Based Design Tools for Quiet Helicopters," AIAA 2006-1068 44th AIAA Aerospace Sciences Meeting and Exhibit, Reno, NV January 2006.
20. Potsdam, M., Le Pape, A., "CFD Investigations on a NACA0036 Airfoil with Active Flow Control," 4th AIAA Flow Control Conference, Seattle, WA, June 2008, AIAA 2008-3869.
21. Bain, J., Mishra, S., Sankar, L., Menon, S., "Assessment of a Kinetic-Eddy Simulation Turbulence Model for 3D Unsteady Transonic Flows," 26th AIAA Applied Aerodynamics Conference, Honolulu, HI, August 2008, AIAA 2008-7176.
22. Fang, Y., Menon S., "A Two-Equation Subgrid Model for Large-Eddy Simulation of High Reynolds Number Flows," AIAA-2006-0116, January 2006.
23. Shelton, A.B., Braman, K., Smith, M.J., Menon, S., "Improved Turbulence Modeling for Rotorcraft," American Helicopter Society 62nd Annual Forum, Phoenix, AZ, May 2006.
24. Morton, S. A., Melville, R. B., Visbal, M. R., "Accuracy and Coupling Issues of Aeroelastic Navier-Stokes Solutions on Deforming Meshes," Journal of Aircraft, Vol. 35, No. 5, September – October 1998.
25. Bhagwat, M. J., Ormiston, R. A. ,Saberi, H. A. and Hong, X., "Application of CFD/CSD Coupling for Analysis of Rotorcraft Airloads and Blade Loads in Maneuvering Flight," AHS 63rd Annual Forum, Virginia Beach, VA, 2007.
26. Geissler, W., Raffel, M., Dietz, G. and Mai, M., "Helicopter Aerodynamics with Emphasis Placed on Dynamic Stall," Wind Energy, 2007, pages 199-204, DOI: 10.1007/978-3-540-33866-6_36.
27. Troolin, D. R., Longmire, E., and Lai, W. T., "Time Resolved PIV Analysis of a Gurney flap on a NACA 0015 Airfoil," 6th International Symposium on Particle Image Velocimetry, Pasadena, California, 21-23 September, 2005.
28. Yu, Y. H., Tung, C., van der Wall, B. G., Pausder, H., Burley, C., Brooks, T., Beaumier, P., Delrieux, Y., Mercker, E., and Pengel, K., "The HART-II Test: Rotor Wakes and Aeroacoustics with Higher-Harmonic Pitch Control (HHC) Inputs – The Joint German/French/Dutch/US Project," American Helicopter Society 58th Annual Forum, Montreal, Canada, June 11-13, 2002.
29. Kunz, D., "Comprehensive Rotorcraft Analysis: Past, Present, and Future" AIAA 2005-2244 46th AIAA/ASME/ASCE/AHS/ASC Structures, Structural Dynamics & Materials Conference, Austin, TX, April 2005.

30. Kufeld, R. M., Loschke, P.C., "UH-60A Airloads Program – Status and Plans," AIAA-1991-3142 Aircraft Design Systems and Operations Meeting, Baltimore, MD, September 1991.
31. Potsdam, M., Yeo, H., Johnson, W., "Rotor Aerodynamic Prediction using Loose Aerodynamic and Structural Coupling", American Helicopter Society 60th Annual Forum, Baltimore, MD, June 1994.
32. Makinen, S., Hill, M., Gandhi, F., Long, L., Vasilescu, R., Sankar, L., "A Study of the HART-I Rotor with Loose Computational Fluid/Structural Dynamic Coupling," American Helicopter Society 62th Annual Forum. Phoenix, AZ., 2006.
33. Bauchau, O. A., Bottasso, C. L., Nikishkov, Y. G., "Modeling Rotorcraft Dynamics with Finite Element Multibody Procedures," Mathematical and Computer Modeling, Vol. 33, 2001, pp 1113-1137. doi: 10.1.1016/S0895-7177(00)00303-4
34. Rajmohan, N., Sankar, L., Bauchau, O., Charles, B., Makinen, S., Egolf, T.A., "Application of Hybrid Methodology to Rotors in Steady and Maneuvering Flight," American Helicopter Society 64th Annual Forum, Montreal, Canada 2008.
35. Tung, C., Caradonna, F.X., Johnson, W.R., "The Prediction of Transonic Flows on an Advancing Rotor," American Helicopter Society 40th Annual Forum, Arlington, VA 1984.
36. Haykin, Simon, Neural Networks, 2nd edition, Prentice Hall, 1999
37. Bain, Jeremy J.; Sankar, L.N.; Prasad, J.V.R.; Bauchau, O.; Peters, D.A.; and He, Chengjian, "Computational Modeling of Variable-Droop Leading Edge in Forward Flight," Journal of Aircraft, Vol. 46, Issue, 2, April, 2009
38. FLIGHTLAB X-Analysis User Manual, Advanced Rotorcraft Technology, Inc., 2008
39. FLIGHTLAB Theory Manuals 1 & 2, Advanced Rotorcraft Technology, Inc., 2008
40. Tischler, M.B. and Remple, R.K.: Aircraft and Rotorcraft system Identification: Engineering Methods with Flight Test Examples, AIAA Publications, Virginia, USA, 2006
41. Johnson, W, "Helicopter Theory", Princeton University Press, 1980.